Understanding the Deposition and Molecular Interaction Mechanisms of Substrate-supported Functional Coatings

by

Jun Huang

A thesis submitted in partial fulfillment of the requirements for the degree of

Doctor of Philosophy

in

Materials Engineering

Department of Chemical and Materials Engineering

University of Alberta

Abstract

Functional coatings have been extensively exploited for creating surfaces with desired functionalities in numerous engineering applications, which have received increasing attention over the past few decades. The objectives of this thesis research were to develop stable, hydrophobicity-tunable functional coatings/films and further investigate the deposition and related surface interaction mechanisms using nano-mechanical techniques such as Atomic Force Microscope (AFM) and Surface Forces Apparatus (SFA). The research has focused on four types of surface coatings, including cross-linked hydrocarbon silane (octadecyltrichlorosilane, OTCS) coating, end-grafted hydrophobic polymer (poly(pentafluorophenyl acrylate)-*b*-polystyrene, PPFPA-*b*-PS) coating, layer-by-layer deposited polyethyleneimine (PEI) and PPFPA-*b*-PS multi-layer coating and mussel inspired polycatecholamine (polynorepinephrine, pNE) coating.

This research has revealed that the deposition process of OTCS on substrate surface with few active sites (*e.g.,* freshly cleaved mica) *via* a facile vapor deposition method mainly contains two stages: silane molecules first react with the limited silanol groups forming a smooth layer and then the initial layer can serve as nucleation sites for further deposition to form cross-linked hydrocarbon coatings. The interaction forces between the as-obtained silane-functionalized mica surfaces were quantitatively measured using an SFA. It was found that the approaching force-distance profiles of the OTCS surfaces obtained *via* a shorter deposition time (*e.g.*, 2 h, 8h) could be reasonably described by the classical Derjaguin-Landau-Verwey-Overbeek (DLVO) theory. However, for the OTCS surfaces obtained *via* longer deposition times (*e.g.*, 48 h), the hydrophobic interaction and steric interaction play an important role due to their enhanced surface hydrophobicity and surface roughness. The obtained results in this work provide useful insights into the deposition behaviors of alkylsilanes on substrates possessing low density of reactive sites *via* vapor deposition method as well as the fundamental interactions of the deposited alkylsilane surfaces in aqueous solutions.

A new type of homogeneous, hydrophobicity tunable PPFPA-*b*-PS polymer coating, covalently end-attached onto mica surface has been developed using a “graft to” methodology *via* amino group reacting with pentafluoro ester. The interactions between the grafted polymer surfaces in aqueous solutions were measured as a function of separation distance using the SFA technique. The effects of various factors, including surface hydrophobicity, salt concentration and degassing, on the surface interactions were examined. It was found that repulsion dominated the approaching process of PPFPA-*b*-PS surfaces with low hydrophobicity (water contact angle ~60^o), while long range attraction (> 50 nm) was detected for surfaces with higher hydrophobicity (water contact angle ~90^o). The range of measured attraction force decreases at high salt concentration or after degassing, which shows strong correlation between nano-bubbles or gas layers present on the hydrophobic PPFPA-*b*-PS surface (water contact angle ~ 90^o) and their long-range attraction. These experimental results help to better understand the interaction mechanisms between stable polymer surfaces in aqueous solutions, with implications for engineering processes such as mineral flotation and protein adsorption.

An efficiency way for preparing multi-functional polymeric films based on covalent bonding between active ester polymer, PPFPA-*b*-PS, and amine-rich polymer, PEI, using spin casting layer-by-layer deposition has been further developed. The film

shows switched hydrophobicity and controllable thickness during deposition. The interactions forces between the as-obtained multi-layer films in aqueous solutions were also measured by using the SFA technique under different experimental configurations. Strong adhesion was measured between PEI and PPFPA-*b*-PS, which shows significant stretching behavior before the two surfaces were separated. Importantly, a facile method has been developed for preparing robust freestanding polymeric films by peeling off the polymer films from silicon substrates, which show good transparency, excellent mechanic property and excellent stability in high salt and organic solvent. This study demonstrates a versatile route for preparing multi-functional polymeric surfaces based on active ester and amines.

Finally, a systematically study about the effect of amine groups on the polymerization and surface interaction of mussel-inspired polycatecholamine coatings (*e.g.*, pNE) in aqueous solutions has been conducted. Our surface-force results based on those smooth pNE surfaces indicate that the adhesive strength between pNE layers is thirty times higher than that of a poly(pyrocatechol) coating without any amine moiety at the same polymerization time. The significant improvement of adhesion after introducing primary amine has proved that primary amine group is a vital factor in the design and development of mussel-inspired catechol-coating materials.

Preface

This thesis is presented in manuscript based format. Chapters 1, 3, 4, 5 and 6 have been published, submitted, or under preparation for submission as described below.

Chapter 1, the section for reviewing hydrophobic interactions has been published in *Biointerphases*: H Zeng, C Shi, J Huang, L Li, G Liu, H Zhong *Recent Experimental Advances on Hydrophobic Interactions at Solid/water and Fluid/water Interfaces*, *Biointerphases* 2016, 11(1), 018903. I was responsible for reviewing the hydrophobic interaction from the aspect of solid/water interfaces as well as the manuscript composition. Chen was responsible for reviewing the part regarding fluid/water interfaces. L Li, G Liu, H Zhong contributed to the manuscript edits. Dr. H Zeng was the supervisory author and was involved in concept formation and manuscript composition.

Chapter 3 has been published in the *Journal of Physical Chemistry B*: J Huang, X Liu, X Qiu, L Xie, B Yan, X Wang, Q Huang, H Zeng *Octadecyltrichlorosilane Deposition on Mica Surfaces: The Insight Interface Interaction Mechanism.* DOI: 10.1021/acs.jpcb.7b00828. I was responsible for the data collection and analysis as well as the manuscript composition. X Liu, X Qiu, L Xie, B Yan, X Wang, Q Huang, contributed to the manuscript edits. Dr. H Zeng was the supervisory author and was involved in concept formation and manuscript composition.

Chapter 4 will be submitted for publication in *Journal of Physical Chemistry C*: J Huang, X Qiu, B Yan, L Xie, H Zeng *End-grafted Hydrophobic Poly(pentafluorophenyl acrylate)-b-Polystyrene Surfaces: Preparation, Characterization and Related Surface Interactions in Aqueous Solutions*. I was responsible for the data collection and analysis as well as the manuscript composition. X Qiu, B Yan and L Xie contributed to the manuscript edits. Dr. H Zeng was the supervisory author and was involved in concept formation and manuscript composition.

Chapter 5, a version of this chapter will be submitted for publication in *Advanced Functional Materials*: J Huang, X Qiu, B Yan, L Xie, H Zeng *Multifunctional Polymeric Films Prepared by A Fast and Covalent Bonded Layer-by-Layer Assembly Process*. I was responsible for the data collection and analysis as well as the manuscript composition. X Qiu, B Yan and L Xie contributed to the manuscript edits. Dr. H Zeng was the supervisory author and was involved in concept formation and manuscript composition.

Chapter 6, part of this chapter has been published in *Angewandte Chemie International Edition*: C Lim,* J Huang,* S Kim,* H Lee, H Zeng, DS Hwang *Nanomechanics of Poly (catecholamine) Coatings in Aqueous Solutions, Angew Chem Int Ed* , 2016, 55 (10), 3342. Some of the research conducted for this chapter forms part of an international research collaboration, led by Professor DS Hwang at Pohang University of Science and Technology, Professor H Lee at Korea Advanced Institute of Science and Technology and Professor H Zeng at the University of Alberta. I was responsible for SFA and AFM data collection and analysis as well as the manuscript composition. C Lim and S Kim were responsible for XPS and AFM data collection and analysis as well as the manuscript composition. Dr. H Lee, Dr. H Zeng and Dr. DS Hwang were the supervisory authors and were involved in concept formation and manuscript composition.

Acknowledgements

After more than four years of PhD study, I am proud to declare that I have achieved one of the greatest moments in my life: my student journey is going to be finished and I will move forward to the next step of my career. This thesis would not have been completed without the help and support from a lot of people, and I would like to express my sincere gratitude to all of them.

First of all, with immense respect and gratitude, I would like to thank my supervisor, Prof. Hongbo Zeng, for his thoughtful insights, immeasurable guidance and support for my PhD study. It was Dr Zeng who guided me through the door into the new area regarding surface forces and colloid interfaces. I will always memorize those visionary advices that he has given to me on scientific research and life path.

Secondly, I would like to thank my beloved wife, Dr. Xiaoyong Qiu. Many thanks to my father, Xinming Huang, my mother, Yiling Chen, my sister Juan Huang, my father in law, Deguo Qiu and my mother in law, Xiulian Fan. Thank you all for your continuous support and immeasurable love. Especially, I want to thank my little daughter, Xiyue Huang. You are a little angle who comes to my life during my PhD study, and it is you the one who makes me truly understand the great responsibility of being a father, and I will always stand besides you as your support in the future.

Thirdly, many thanks to all the group members in Dr Zeng's group, especially to Dr Bin Yan and Dr Xiaokong Liu, for their kind suggestions and discussions on my research and future career. Thanks to my Master supervisor, Prof. Liping Zhu, Prof. Xinsheng Peng and Prof. Jianguo Lv in Zhejiang University, for their assistance and support for kindly recommendation during my application for studying abroad.

Many thanks to my friends, Jinjun Nie, Jing Wang, Peng Huang and An Zhao,

Kaiwen Liu and Su Tian who have helped me through during my stay in Edmonton.

Also, the research project would not have been successfully finished without the financial support from Alberta Innovates. I want to thank Prof. Steve Kuziniki for his interesting lectures and the reference letter during my application.

Once again, thanks to all the people that I have met and become part of my life. Wish all of you the best, live long and prosper~

TABLE OF CONTENTS

List of Tables

List of Figures

List of Abbreviations

APTES	(3-Aminopropyl) triethoxysilane
AFM	Atomic Force Microscopy
AIBN	Azobisisobutyronitrile
ATR-FTIR	Attenuated Total Reflectance Fourier Transform Infrared Spectroscopy
CA	Contact Angle
DA	Dopamine
DDMAT	2-(dodecylthiocarbonothioylthio)-2-methylpropionic acid
DHBA	3,4-dihydroxybenzaldehyde
DHI	5,6-dihydroxyindole
DLVO	Derjaguin-Landau-Verwey-Overbeek
DMT	Derhaguin-Muller-Toporov
DOPA	*L*-3,4-dihydroxyphenylalanine
EDL	Electrostatic Double-Layer
FECO	Fringes of Equal Chromatic Order
JKR	Johnson-Kendal-Roberta
LB	Langmuir–Blodgett
LbL	Layer-by-Layer
MBI	Multiple Beam Interferometry
NE	Norepinephrine
OTCS	Octadecyltrichlorosilane
PAM	Polyacrylamide
PC	Pyrocatechol
pDA	Polydopamine
PEG	Polyethylene Glycol
PEI	Polyethylenimine
PEMs	Polyelectrolyte multi-layers

PEO	Polyethylene oxide
PFO	Perfluoro caprylic acid
pNE	Polynorepinephrine
pPC	Polypyrocatechol
PPFPA	Poly(pentafluoro-phenyl acrylate)
PPFPA-*b*-PS	Poly(pentafluorophenyl acrylate)-*b*-polystyrene
RAFT	Reversible Addition-Fragmentation Chain Transfer
RMS	Root-Mean-Square
SAM	Self-assembled Monolayer
SEM	Scanning Electron Microscope
SFA	Surface Forces Apparatus
SIMS	Secondary Ion Mass Spectrometry
vDW	van der Waals
XPS	X-ray Photoelectron Spectroscopy

CHAPTER 1

INTRODUCTION AND LITERATURE REVIEW

1.1 Hydrophobic and Hydrophilic Surfaces

“Hydrophobic” and “hydrophilic” are terms used to define the affinity of water on different surfaces. The word “hydro” origins from the ancient Greek words, meaning water, “phobos” meaning fear, and “philia” meaning love.[1] A hydrophobic surface tends to repel water, while a hydrophilic surface tends to adsorb water or be wetted by water. Water contact angle (CA) is a direct expression of the hydrophobicity (*i.e.*, wettability) of a surface. Surfaces with CA greater than 90° are generally designated as hydrophobic. Textured hydrophobic surfaces that exhibit apparent CA exceeding 150° are termed as superhydrophobicity. On the other hand, the surface is designated hydrophilic if the CA of water is less than 90°, and if water spreads over the surface with a CA less than 10°, the surface is designated as superhydrophilic.[2]

According to the composition and structure of hydrophobic species, hydrophobic surfaces can be mainly classified into two large categories including natural hydrophobic surfaces and artificial hydrophobic surfaces.

Natural hydrophobic surfaces

Nature is one of the greatest artists for creating hydrophobic surfaces with unique properties. Figure 1.1 shows several natural-hydrophobic surfaces with related scanning electron microscope (SEM) images showing the detailed hierarchical micro-structure. The lotus surface (Figure 1.1a) normally possesses the characteristic of superhydrophobicity and self-cleaning, and the SEM image shown in Figure 1.1b suggests that this kind of surface is composed of both micro- and nano-architecture structures and a layer of low surface energy epicuticular waxes.[3] The water strider's legs are covered by large numbers of oriented tiny hairs (micro-setae) with fine nano-grooves, inducing superhydrophobic water resistance ($CA>150^o$). And this superhydrophobicity results in a supporting force which is 15 times of the total body weight of the insect for a single leg, as shown in Figure 1.1c, d.[4] The butterfly surface (Figure 1.1e) shows unique pattern-structure which could induce an interesting directional adhesion of water, *i.e.*, the water droplet could easily roll off the surface of the wings along the radial outward direction, but is pinned tightly against the radial outward direction, and the detailed features are shown in Figure 1.1f.[5] The petal surfaces (Figure 1.1g) are in Cassie impregnating wetting state which inhibits the water droplet from sliding down the petal surface (Figure 1.1h).[6] The hydrophobic surfaces we mentioned above are just several typical examples. Inspired by those extraordinary and unique hydrophobic surfaces in nature, researchers have made impressive efforts to prepare artificial hydrophobic surfaces.[3, 7]

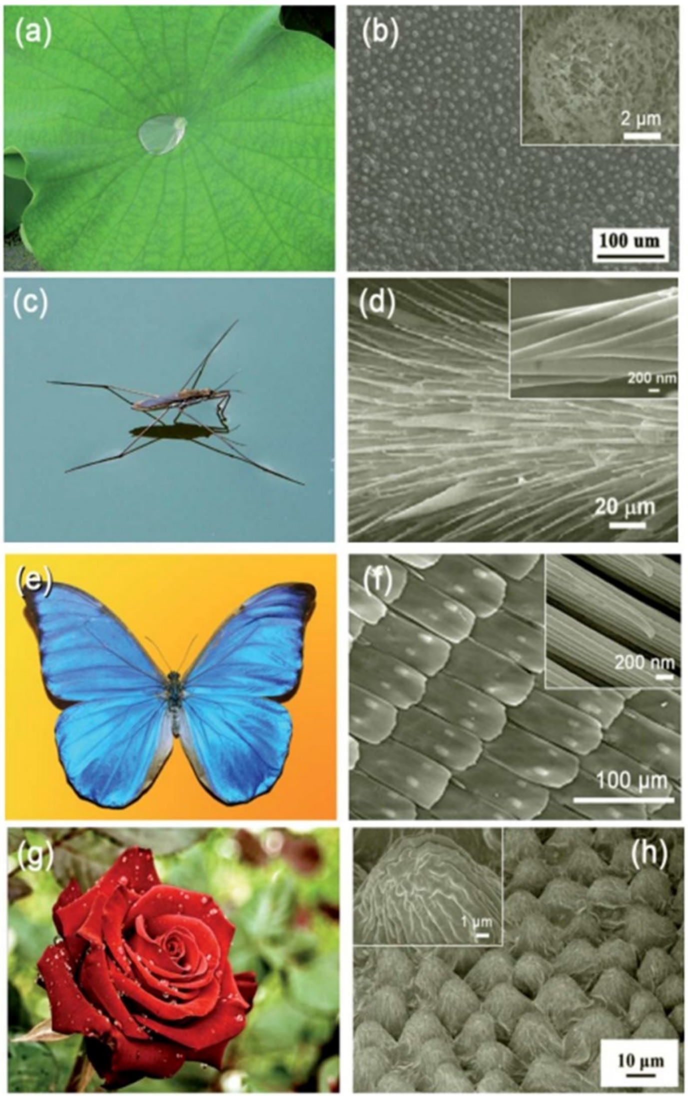

Figure 1.1 Photos of typical natural hydrophobic surfaces and related scanning electron microscope (SEM) images, which show the detailed microstructures.[7] The insets show the higher resolution SEM images of : (a, b) lotus surface [3] (c, d) the leg of water striders. [4] (e, f) butterfly surface [5] and (g, h) petal surface. [6]

Artificial hydrophobic surfaces

The second large category belongs to artificial hydrophobic surface, which is mainly prepared by self-assembling, polymerization or forming chemical bonding between molecules and surfaces. Those artificial hydrophobic surfaces are mainly classified into the following categories.

a) Solid surfaces coated with physically adsorbed surfactants or polymers (hydrocarbon or fluorocarbon groups). Different coating methods such as spin coating, dip coating are often employed to prepare this kind of surfaces. [8,9]

b) Amphiphilic molecules (such as fatty acids) assembled into mono or multi-layers on smooth substrates through Langmuir–Blodgett (LB) deposition. LB deposited surfactants on flat surfaces have been frequently used for studying hydrophobic effects in early years. [10, 11]

c) Surfaces functionalized with hydrophobization agents such as silane coupling reagents (octadecyltrichlorosilane, trimethoxysilane, triethoxysilane and *etc*). These surfaces are usually stable due to the chemical bonds formed at the interface. Unlike physical adsorbed polymer surfaces or surfactant surfaces, which may break due to the compress strain during contact, the hydrophobic surfaces created by chemical grafting or reaction could have good reproducibility and are robust for studying hydrophobic interactions.[12]

d) Inherent hydrophobic surfaces which are generally observed in daily life. Naturally hydrophobic minerals surfaces (*e.g.*, graphite, coal) and bulk polymers surfaces (*e.g.*, polystyrene, polytetrafluoroethylene) are typical examples for this category.

e) Superhydrophobic surface (CA>150^{o}) is another kind of hydrophobic surface that attracts great research interests for decades. This type of surface generally combines the features of using low surface energy materials/coatings and high surface roughness. Importantly, superhydrophobic surfaces which show interesting properties such as anti-ice, self-cleaning, mimicking natural hydrophobic surfaces are mentioned in Figure 1.1. [7]

f) During the past few years, the liquid infused porous surface, which is inspired by Nepenthes pitcher plants surface, becomes another interesting topic for surface preparation and functionalization. This kind of surface shows versatile properties for anti-fouling,[13, 14] anti-ice, [15] self-healing and is almost repellent to all kinds of liquids.[13] Nevertheless, this kind of surface are still facing problems such as evaporation and instability under flow conditions. There is still a long way to go before commercialization.

On the other hand, hydrophilic surfaces are those generally contains polarity groups, wherein surface molecules or their chemical groups have an electric dipole or multipole moment resulting in strong interaction with water molecules.[16] In fact, hydrophilic surfaces are more abundant than hydrophobic surfaces in nature.[16] According to the composition and structure of hydrophilic species, hydrophilic surfaces can be mainly classified into the category listed as follows.

a) Silicates and ceramics such as cleaved mica, quartz, lead zirconate titanate, yttrium barium copper oxide, *etc.* [17]

b) Metal oxides and hydroxylated oxides such as TiO_2, $Cu(OH)_2$, Al_2O_3, *etc.*

c) Biological membranes such as phospholipid bilayer.

d) Ionic crystals (*e.g.*, sodium chloride) which are often hygroscopic and pick up water from air.[1]

e) Metallic surfaces such as native gold and silver surface without contamination.[16]

f) Bulk polymers with polar groups such as polyethylene glycol (PEG), polyacrylamide (PAM), polyethylenimine (PEI) and *etc.*

g) Surfaces with hydrophilic chemical coatings such as grafted hydrophilic silane coatings,[2] mussel inspired polydopamine coatings,[18,19] polyphenol coatings[20, 21] and zwitterionic polymer brush coatings.[22, 23]

h) Hydrophobic surfaces that undergoes physical treatment such UV oxidation, plasma treatment could also increase the polarity of the surface and change them into hydrophilic surfaces.[24]

1.2 Surface Forces

Understanding the interaction mechanisms of different surfaces is essential in many engineering applications such as sedimentation, rheology, stabilization or destabilization of colloidal suspensions, thin film lubrication and adhesion.[25] Some of these important intermolecular and surface interactions mainly include DLVO (Derjaguin-Landau-Verwey-Overbeek) forces such as van der Waals force and electrostatic double-layer force, non-DLVO forces such as hydrophobic interactions, steric force, solvation force and hydrogen bonding. The van der Waals force, electrostatic double-layer force, hydrophobic interaction will be described in detail in the later sections.

Derjaguin-Landau-Verwey-Overbeek (DLVO) Forces

The DLVO forces can be well described by DLVO theory, named after Boris Derjaguin, Lev Davidovich Landau, Evert Johannes Willem Verwey and Theo Overbeek in the 1940s. This theory combines the effects of the van der Waals forces (vdW) and the electrostatic double-layer forces (EDL) due to the so called double layer of counter ions.

Van der Waals forces

Van der Waals forces are residual attractive or repulsive force between molecules that do not arise from a covalent bond or electrostatic interactions between opposite charged ions. It is a dispersion force which is omnipresent and play important roles in adhesion, surface tension, physical adsorption, wetting, physical properties of gases.[26] Van der Waals force mainly composes of three parts: a) Keesom force origin from permanent dipoles; b) Debye force from a permanent dipole and an induced dipole; c) London dispersion force between instantaneously induced dipoles.[1]

The vdW interaction potential and forces between two atoms or two macroscopic bodies of different geometries with surface distance D apart are shown in details in Table 1.1. It is found that the van der Waals pair potential $W(D)$ between two atoms or small molecules could be give by Equation 1.1, where C is the coefficient in the atom-atom pair potential, r is the distance between two atoms.

$$W(D) = -C/r^6 \tag{1.1}$$

At mean time, the van der Waals interaction potential W (D) and force $F(D)$ are related by Equation 1.2, where D is the separation distance.

$$F(D) = -dW(D)/dD \tag{1.2}$$

It is worth notice that the vdW force between atoms or molecules is a short range force and proportional to $-1/r^7$, while the vdW force between two macroscopic bodies is a relative long-range force and depends on the shapes of the bodies. Hamaker has proposed a simple pairwise additive model which ignores the influence of an intervening medium between the two bodies to calculate the van der Waals forces. A new constant named Hamaker constant (A) is defined, which is given by Equation 1.3, where C is the coefficient in the atom-atom pair potential, ρ_1 and ρ_2 are the numbers of atoms per unit volume in the two bodies, respectively.

$$A = \pi^2 C \rho_1 \rho_2 \tag{1.3}$$

Typical Hamaker constants values of condensed phases are about 10^{-19} J for interactions in vacuum.[1]

Table 1.1 Van der Waals interaction energy W and force F between two macroscopic bodies in terms of Hamaker Constant, A [1]

Geometry of bodies with surface distance D apart (D<<R)		**Energy, *W(D)***	**Force, *F(D)* =-*dW(D)/dD***
Two atoms or small molecules	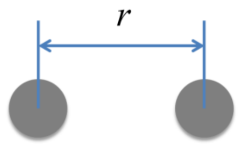	$-C/r^6$	$-6C/r^7$
Two flat surfaces (per unit area)	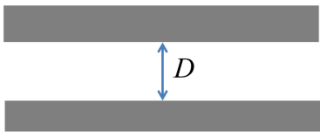	$-A/12\pi D^2$	$-A/6\pi D^2$
Two spheres with radii R_1 and R_2	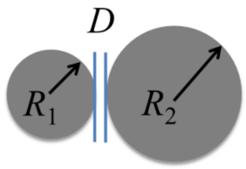	$\frac{-A}{6D}(\frac{R_1R_2}{R_1+R_2})$	$\frac{-A}{6D^2}(\frac{R_1R_2}{R_1+R_2})$
Sphere-Surface	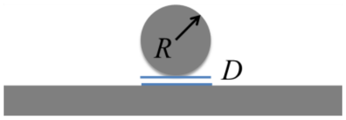	$-AR/6D$	$-AR/6D^2$
Two crossed cylinders or filaments of radii R_1 and R_2 at 90°	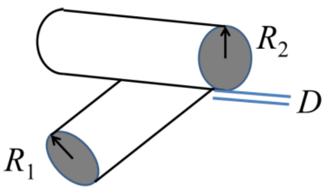	$\frac{-A\sqrt{R_1R_2}}{6D}$	$\frac{-A\sqrt{R_1R_2}}{6D^2}$

Gouy-Chapman Double Layer and electrostatic Double Layer (EDL) forces

It is generally considered that the boundary of two phases possesses properties that are quite different from material extended in the continuous phases, especially at the interfaces. Most surfaces in contact with water acquire surface charges.[27] Gouy and Chapman developed the diffuse double layer to describe the charge distribution and concentration of the counter ions near a charged surface with a surface potential Φ_m in aqueous solutions. Interfacial potentials of the charged solid surfaces could be attributed to the presence of layers of adsorbed ions. The first layer of surface charge comprises of counter ions adsorbed onto the surface are defined as Stern layer (Φ_1), which is shown in Figure 1.2. The thickness of Stern layer is on the order of the ionic radius due to the finite ion size. On the other hand, the second layer between Stern plane and slipping plane (Φ_2) is composed of ions attracted to the first layer *via* the Coulomb force. And generally this layer is made of free ions that could be influenced by electric interactions or thermal motions rather than being firmly anchored. And this layer is called the "diffuse layer". When two charged surfaces approaching each other under aqueous solutions, the electric field induces force on the diffuse layers, as well as on the surface charges. The thickness of the diffuse layer decreases with increasing valence and concentration of ions.

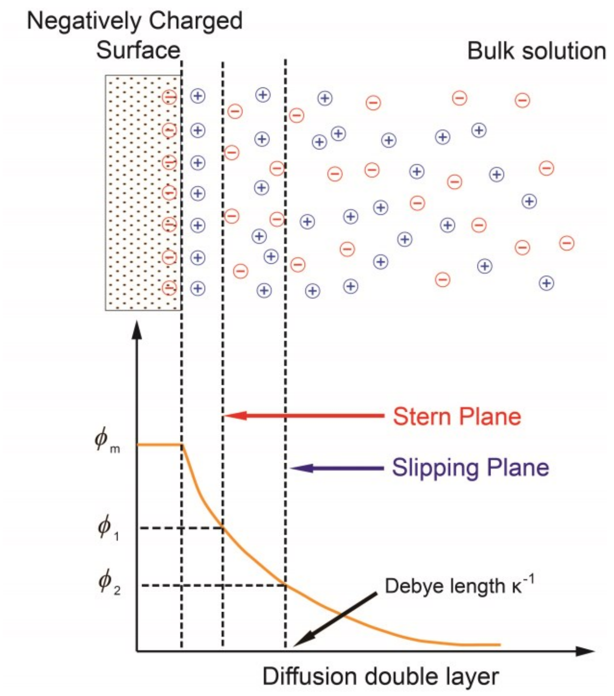

Figure 1.2 Schematic illustration of diffusion double layer model of a charged surface

The DLVO force has been widely used to explain the interactions between charged surfaces in an aqueous solution. It is a combination of vdW force and double layer force as follows:

$$F_{\mathrm{DLVO}}=F_{\mathrm{vdW}}+F_{\mathrm{DBL}} \tag{1.4}$$

where F_{DLVO} is the DLVO force, F_{vdW} is van der Waals force and F_{DBL} is electrostatic force. The DLVO theory predicts that the interaction energy per unit area between two flat surfaces can be given by Equation 1.5 and Equation 1.6.

$$W_{DLVO} = -A_{121}/12\pi D^2 + 64\pi\varepsilon_0\varepsilon\left(k_B T/ze_0\right)^2(\kappa/2\pi)\tanh^2\left(ze_0\psi_0/4k_B T\right)e^{-\kappa D} \tag{1.5}$$

$$1/\kappa = \left(\varepsilon_0\varepsilon k_B T\Big/\sum_i \rho_{\infty i}e_0^{\,2}z_i^2\right)^{1/2} \tag{1.6}$$

where A_{121} is the Hamaker constant of two surfaces 1 across liquid 2, D is the separation distance, ε_0 is the dielectric permittivity of free space, ε is the dielectric constant of confined liquid, k_B is Boltzmann constant, T is absolute temperature, z is the number of charge, e_0 is the elementary charge of a single electron, $1/\kappa$ is the so-called Debye length (*viz.* the characteristic decay length of the electrostatic double-layer interaction given in Equation 1.5), Ψ_0 is surface potential, $\rho_{\infty i}$ is the number density of *i*th ion in the bulk solution and z_i is the valency of the *i*th ion. It is noted that van der Waals force is almost insensitive to solution conditions while double-layer force can be significantly affected by ionic strength.[1] As a result of these differences, DLVO forces can be repulsive or attractive depending on separation distance, solution conditions and the intrinsic properties of those surfaces.[28] The *E*-ink technology (Figure 1.3) is one of the typical examples for employing the DLVO force to realize high brightness, ultra-low power requirement paper-like display. The display for this electronic book is reflective, not emissive. It contains small, electrically-charged particles suspended in oil whose position is controlled by electrophoretic motion. It is an "electrostatic" device - one "ruled" by electronic charge.[29]

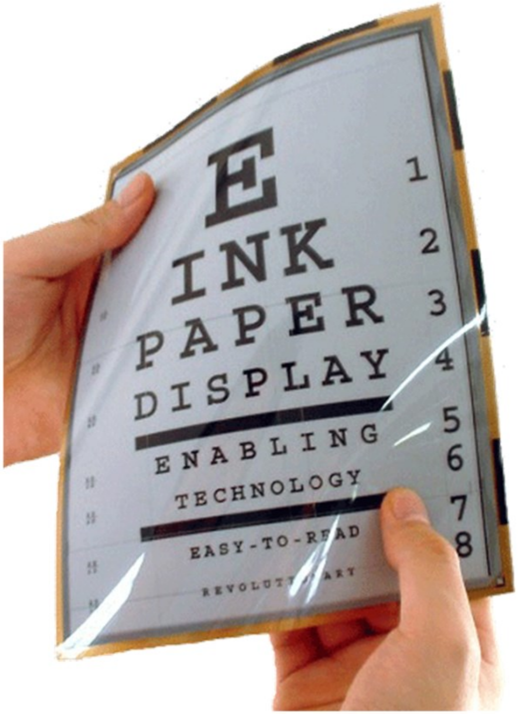

Figure 1.3 Electro-static interaction based E-ink paper displaying text with great flexibility. Image source: http://leeet.net/en_e_ink.php.

1.3 Surface Interaction between Hydrophobic Surfaces

In above paragraphs, we mainly talked about the DLVO forces, however, non-DLVO forces also play important roles between different surfaces in actual life. Hydrophobic interaction, also known as hydrophobic effect, can be qualitatively understood as an interaction that causes hydrophobic moieties to aggregate or cluster in water.[11] This effect plays a critical role for a wide range of phenomena such as the low solubility of hydrophobic solutes or non-polar groups in water, fast protein folding in biological systems, micelle and lipid bilayer formation, self-assembly in water solution, the long range attractive force between two hydrophobic surfaces, flotation for air-water interface, slip boundary condition for water flow through channels.[11] Once in a while, the hydrophobic interaction is so strong that makes people believe that there is “hydrophobic bond”.[1] However, the word “bond” is not suitable because this interaction is very hard to quantify, and no evidence of chemical or metallic bond like characteristic exists.

The first direct measurement of the long-range attractive interaction is performed by Dr. Israelachvili and Dr. Pashley in 1982 using the Surface Forces Apparatus (SFA) and the experiment results show a strong long-range attraction in water.[30] This long-range attraction exceeds the range of van der Waals interaction by at least 1-2 orders of magnitude. Since then, research on the origin for hydrophobic surfaces has been the focus for more than thirty years. Even until now, no single theory could encompass the large quantity of experiment results.

Origin of hydrophobic interactions

Great efforts have been dedicated to study the origin of hydrophobic force, however, the interpretation of the unusually long range attraction varies from report to report. Great debate still exists over the issue “what is a true hydrophobic force”. In this section, the theories regarding the origin of hydrophobic forces will be briefly introduced.

a) Bridging of bubbles & bubbles cavitation

The dissolution of gases will become inevitable in water when water solution is in contact with air. One of the most widely accepted theory for explaining the unusual long range hydrophobic force is the bridging of bubbles and cavitation. Early research showed that degassing had some important effects on interfacial properties. For example, after degassing, spontaneous emulsification of hydrocarbons will occur, [31] the range and magnitude of the interaction decreases though it does not disappear completely. [8, 32,.33]

The first evidence of the existence of bubbles during force measurement was reported by Parker *et al*, where the SFA technique has been used to measure the attractive force between two hydrophobic surfaces in water.[34] They found that the attractive forces exhibit discrete steps when bringing the two hydrophobic surfaces together, which is shown in Figure 1.4. Later, the existence of sub-micrometer or nanometer bubbles (the so-called surface nanobubbles) at solid−liquid interfaces are further confirmed by other groups.[34, 39, 41]

Generally, the pressure inside bubbles will increase due to surface tension. According to Young-Laplace equation shown in Equation 1.7, the pressure-increase inside the bubble can be calculated as

$$\Delta P = 2\gamma / r \tag{1.7}$$

where in this equation, ΔP is the pressure increase, γ is the surface tension of the liquid, r is the radius of the bubble.

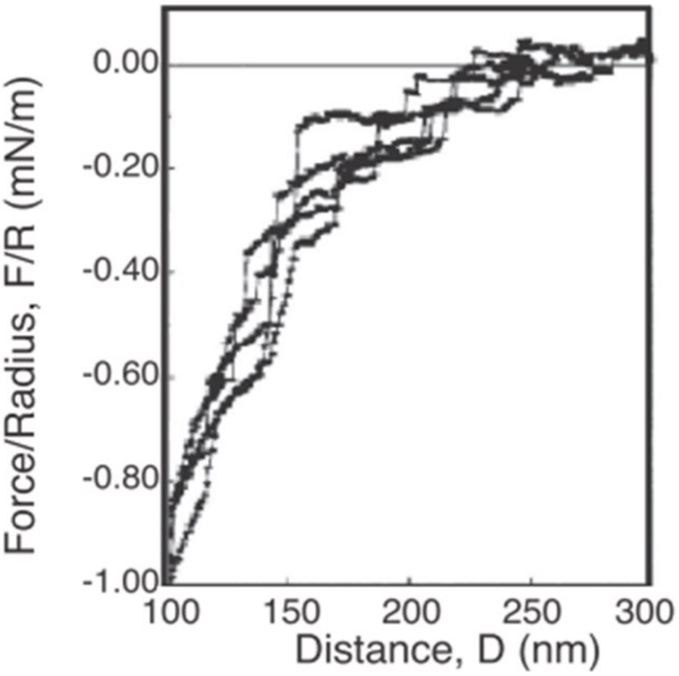

Figure 1.4 Discrete steps in force-distance curves reported by Parker *et al.*[34]

Based on the Young-Laplace equation, for a bubble with a radius of 100 nm in water, the pressure difference (ΔP) will be ~14 times of atmosphere pressure; and for the bubble with 10 nm radius, this value will increase to more than 140 atmosphere pressure. The large pressure elevation indicates that classic theories predict that nanobubbles are unstable and they should dissolve in the order of microseconds. However, recent report proves that nanobubbles can be observed on a lot of surfaces, even quite hydrophilic ones.[35] These nanobubbles are actually measured over a time scale of several hours or up to days. More importantly, those bubbles are stable not only under ambient conditions but also under enormous reduction of the water pressure.[35, 36]

The high pressure increase for nanobubbles mentioned above seems to be in contradiction with the classic theory. The stability of nanobubbles at the surface is still greeted with skepticism. This interesting phenomenon attracts lots of research on the stability of nano-bubbles. Brenner *et al.* suggest that nanobubbles are in a dynamic equilibrium, that the gas leaving the bubbles is compensated by gas re-entering at the three-phase contact line.[37] However, the energy source governing this recirculation remains elusive. Surface contamination,[38] three phase contact line pining,[39] supersaturated liquid[40] could all contribute to the formation and stability of nanobubbles on surfaces. A general and acceptable theory on the formation and stability of nanobubbles is still lacking.

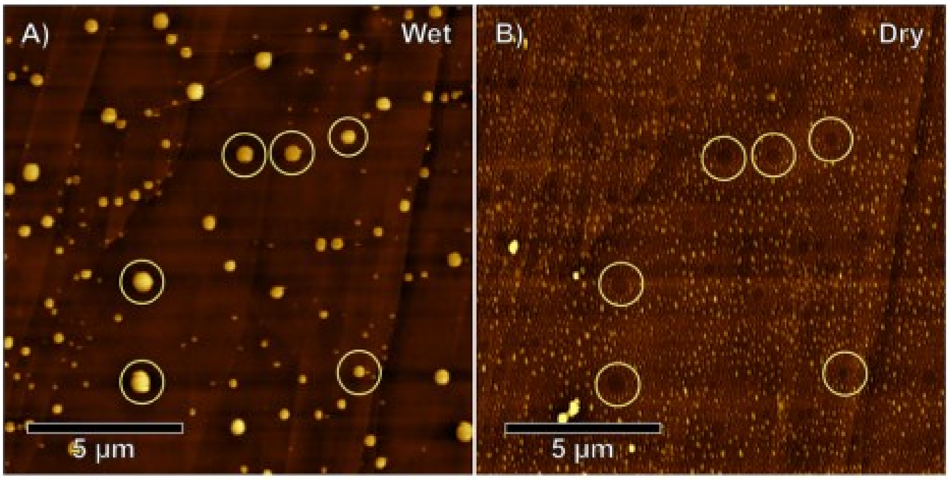

Figure 1.5 (A) Image of nanobubbles on HOPG in a 0.01 M NaCl solution, (B). image of bubble induced footprint pattern after drying. [41]

Besides the evidence provided by force measurement, there are also other indirect evidence which demonstrates that bubbles on hydrophobic surface could induce the change of surface morphology. For example, Wang *et al.* reported the formation of nanoindents caused by nanobubbles during the immersion of an ultrathin polystyrene film spin-coating on a silicon substrate in deionized water. With the elongation of immersing time, nanobubbles first shrank and rims appeared around them. Small nanobubbles with diameters less than 50 nm gradually disappeared, leaving nanoindents at their sites.[42] Additionally, pre-existing surface nanobubbles prevented the homogeneous coverage of the surface with the salt, keeping the footprint areas on the substrate pristine. As shown in Figure 1.5, the circles in both images (A, B) show a direct relation between nano-bubble and the NaCl-deprived footprint.[41]

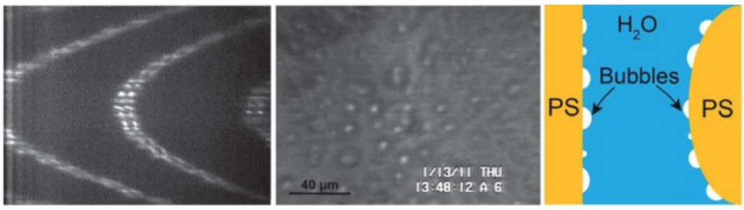

(a) Two PS surfaces were far from each other, and air bubbles were present on the PS surfaces.

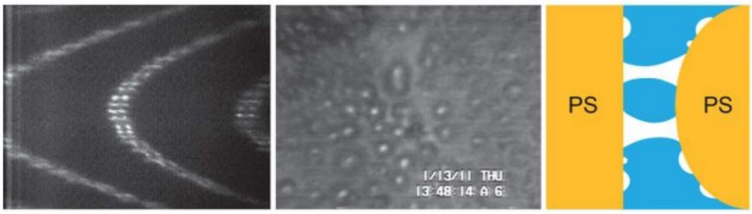

(b) Air bubbles started to coalesce which led the two PS surfaces to get closer.

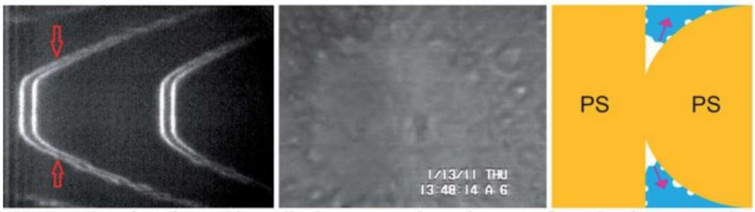

(c) Two PS surfaces jumped into adhesive contact, air meniscus was formed at the contact edge and propagated outward as fingering patterns (at air-water interface).

Figure 1.6 Evidence provided by top view camera indicates the existence of micro-bubbles on physically adsorbed polystyrene surfaces presented by Faghihnejad *et al.*[8]

A recent research done by our group also supports the existence of micro bubbles on physical adsorbed polystyrene surfaces. As shown in Figure 1.6, the discontinuity of the FECO fringe coupled with top view images provide strong evidence of the existence of micro size bubbles on hydrophobic polystyrene surfaces. Those bubbles coalesce and the front of the FECO fringe becomes flat when the two surfaces are getting into contact.[8] Ishida *et al.* also performed the solvent exchange method to prevent the formation of nanobubbles, and the long range attraction force is still observed without the influence of nanobubbles. Both the ionic strength and temperature has little effect on this force.[43] They consider that the force without the influence of bubbles is the genuine hydrophobic force.

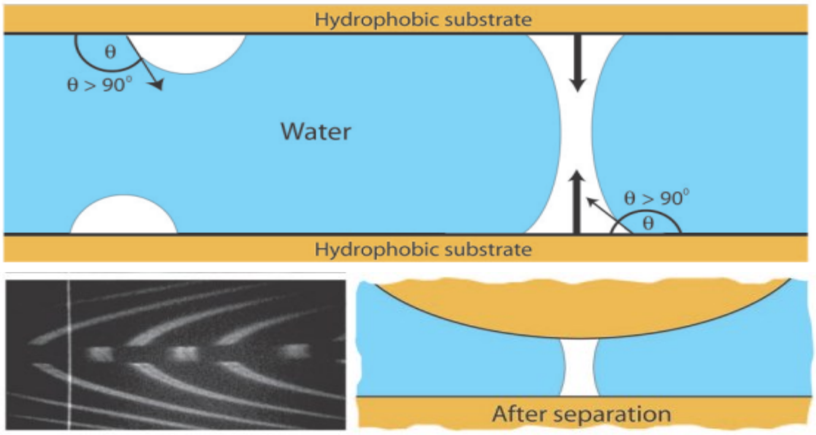

Figure 1.7 Cavitation observed during surface force measurement.[44]

In addition to the direct bridging effect of bubbles on surfaces, cavity due to meta-stability of the intervening fluid during approach or separation may also cause the unusual long range force.[44,45] It is observed that spontaneous cavitation occurred when the fluorocarbon surfaces were brought into contact, while it occurred only after separating two hydrocarbon surfaces from contact, as shown in Figure 1.7.[44] The spontaneous cavitation of vapor and dissolved gas was also observed in octadecyltriethoxysilane modified hydrophobic surfaces reported by Meyer *et al.*[11]

The effect of bubbles and cavity on immersed hydrophobic surface is of interest in many applications. Further study on the influence of size, position of the bubbles on hydrophobic forces can be conducted based on various hydrophobic surfaces. Namely, a lot of work can be done in the "bubble" field.

b) Electrostatic interaction and charge fluctuations

Early research done by Phil suggested that the long-range attraction could also be explained as part of the van der Waals forces. The long range force is attributed to an anomalous electrostatic response of the aqueous fluid which is perturbed by the adjacent hydrophobic surface. This short range perturbation in the fluid can induce a measurable force at large distance.[46] Podgornik *et al.* also reported the strong correlation between surface electrostatic potential induced electrostatic repulsion and the collapse of the surfactant film induced hydrophobic attractive forces.[47] A recent study on hydrophobic surfaces composed of double-chained cationic surfactants (dimethyl-dioctadecyl-ammonium bromide) indicated that surfactants in the self-assembled smooth monolayer in air could overturn and rearrange into charged bilayer patches in water at high electrolyte concentration or when changing temperature. Due to the electrostatic interaction between the negative charged mica and the positive charged surfactant head groups (Figure 1.8), a long-range attractive force was observed. However, this kind of long-range attractive force should not be considered as the genuine hydrophobic force. [48]

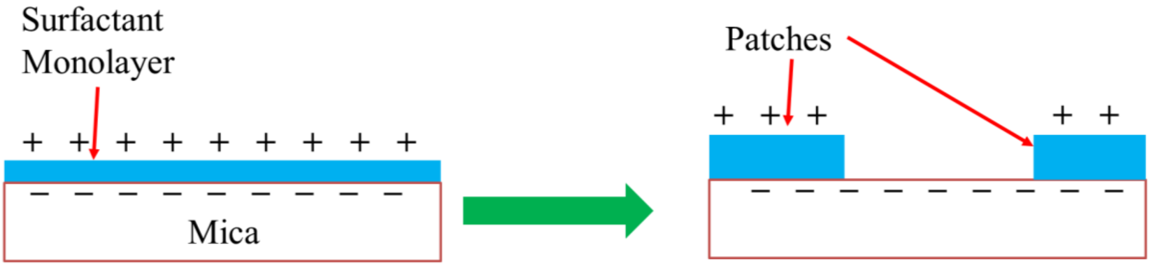

Figure 1.8 Sketch map of the collapse formation of patchy bilayers on mica surfaces.

c) Water structure and entropic effect

For short-range hydrophobic interaction, water structure becomes an important factor that needs to be considered. Water molecules will rearrange into a microscopic “iceberg” around a nonpolar molecule.[11, 49] As shown in Figure 1.9, entropic effect due to the rearrangement of H-bonding configuration around hydrophobic surface is the cause of this short range hydrophobic interaction.

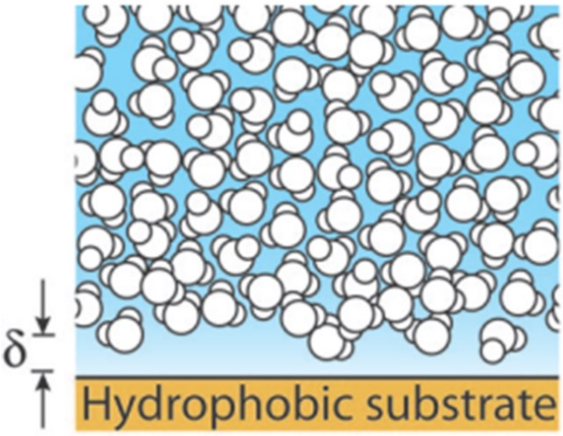

Figure 1.9 A depletion layer exists next to a hydrophobic surface, but the range of the effective distance is only several layers of water molecules.[11]

A recent report for studying the effect of degassing on surface morphology of flat hydrophobic polystyrene supported that there is a layer of polymer with enhanced mobility and reduced density when water is nearby. And the top layer of polymer could reconstruct even when the temperature is below the glass transition temperature (T_g).[33] Although atomistic simulations predict that non-polar surfaces can influence the structure and compressibility of water over a distance of 1 nm, [11,50, 51] the water structure theory still can't well explain the long range force which can extended to tens and several hundreds of nanometers.

d) The effect of ions on hydrophobic interactions

Early research also suggested that ion pairing in aqueous media, when approaching a hydrophobic surface, would be enhanced.[51] Recently, specific ion effect on hydrophobic surface has also attracted much interest. By studying the force interaction between an alkyl-functionalized tip with alkyl-functionalized gold surface using chemical force microscopy, Ma *et al.* found that proximal ions such as amine or guanidine groups can dramatically change the strength of hydrophobic force.[52] In a very recent work, Chen *et al.* reported that ionic interactions on a hydrophobic surface are modulated by their subnanoscale distance to the surface.[53] Those charged function groups near hydrophobic domains provide a strategy for tuning hydrophobic forces to optimize molecular recognition or self-assembly processes.[54]

e) Conclusion about hydrophobic forces

In spite of the tremendous progress that has been made to fully understand the origin of hydrophobic forces. The measured unusual long range attractive force can be considered to be the sum of several different forces. Generally, the hydrophobic interactions between polymer hydrophobic surfaces origin from three regimes: a very long-range interaction regime from 20 nm to several hundreds of nm, due to the bridging of microscopic and sub-microscopic bubbles or electrostatic interactions; (II) an intermediate interaction regime around 10 – 20 nm, due to the bridging of nano-bubbles or enhanced Hamaker constant associated with enhanced proton hopping in water; and (III) a short range interaction regime (from < 1 nm to several nanometers), mainly due to the water structure changes close to the hydrophobic surfaces.[8]

1.4 Other non-DLVO Force

In previous sections, we mainly introduce the DLVO theory and attractive hydrophobic force. However, non-DLVO forces such as polymer steric repulsion and bridging, hydration repulsion and depletion forces could also play significant roles in colloid and interface science. Typically, when the outer segments of two polymer-adsorbed or polymer-grafted surfaces begin to overlap during approaching, the polymer steric force, which is a repulsive osmotic force due to the unfavorable entropy associated with compressing the chains between the surfaces, could be measured.[1] The steric barrier between the two polymer coated surfaces is of great significance in stabilization of emulsion and colloid particles. For two hydrophilic surfaces, hydration repulsion between strongly hydrophilic groups with its strength mainly depending on the hydration structure of the surface groups could be measured.[1] The hydration repulsive force is akin to the polymeric steric force and mostly due to the entropic arising when the thermally excited chains and head-groups protruding are confined between two approaching surfaces in aqueous solutions. This kind of force is generally short ranged and follows exponentially decay law.[1] For non-ionic polymers that adsorbed at high concentration, a monotonically increasing steric repulsion is generally measured, however, for the case when low adsorbance ratio of the polymer on typical surface is achieved, there is a polymer-bridging force, which is long range attractive, reversible and time-independent during approaching.[55] The polymer bridging force is an important reason for the flocculation of colloids by adding non-ionic polymers. Depletion force, also regarded as a kind of entropic forces, is an attractive force that arises between large colloidal particles that are suspended in a dilute solution of smaller solutes that are preferentially excluded from the surroundings of the large particles. Thus, the depletion force could also facilitate the coagulation of colloidal particles. Those small solutes could be polymers, micelles, osmolytes, ink or even mud.[56, 57] Under other circumstances, when nano-particles are confined in between two randomly rough surfaces, whether elastic or elasto-plastic, upon compressing, exponential steric repulsion is measured using the SFA technique.[58, 59] In short, the surface interactions are quite complex because various factors such as surface roughness, chemical composition, bonding state, hydrophobicity and the medium environment should be taken into consideration, and sets of experiments need to be designed to identify the major driving force for most cases.

1.5 Mussel Inspired Hydrophilic Coatings

The above sections mainly describe the classification of hydrophobic, hydrophilic surfaces and typical surface interactions. And we also emphasize on the origin of hydrophobic force, which is still under debate. In this part, I will briefly review a versatile polymer coating method which is inspired by marine mussels. In this thesis research, this coating method has been used to prepare catecholamine coatings on mica surface, so as to study the role of amine groups for underwater adhesion employing the SFA technique.

Mussels are capable of attaching to all types of wet surfaces through mussel threads, which manifest strong underwater adhesion. *L*-3,4-dihydroxyphenylalanine (*L*-DOPA), a non-canonic amino acid produced by post-translational modification of tyrosine, is widely found in the protein of those mussel threads. And the catecholamine structure in DOPA has been proved to be critical for achieving strong underwater adhesion.[60, 61] Dopamine (DA) is a small molecule that contains catecholamine structure and mimics the adhesive component *L*-DOPA in marine mussels. DA has the capability to adhere and self-polymerize to form polydopamine (pDA) films on almost any kind of surfaces by simply soaking targeted substrates in a basic DA solution for certain time. More importantly, the formed pDA film can serve as a versatile platform for post-polymerization synthetic or modification because the pDA is a mixture of cross-linked products bearing mostly catecholamine and quinone groups.[18, 19] It has been reported that DOPA and dopamine could been combined with antifouling polymers such as polyethylene oxide (PEO) for achieving antifouling coatings and improve the fouling resistance of porous membrane.[62, 63, 64] Inspired by those pioneered work, mussel-inspired poly(catecholamine) coatings have rapidly become a hot topic that attracts lots of research interests for multifunctional coating and bio-adhesion application. However, the dopamine coating are still facing challenges such as high cost,[65] relatively low deposition rate[66] and difficult to control the surface morphology.[67] Especially uncontrolled polymerization of dopamine results in undefined nano-aggregates presented at interface when measuring surface interactions, which adds up to the difficulty for revealing the intrinsic mechanism of underwater adhesion. In order to generate smooth polymer film with high deposition efficiency, other chemicals that contains similar catecholamine group such as norepinephrine,[67, 68] or alternated deposition protocol have been developed. [66, 69]

Norepinephrine (NE) is one of the catecholamine neurohormone and neurotransmitters with a structure similar to dopamine, it could control responsiveness to stress and fear in human body. Importantly, NE is also capable of achieving substrate independent self-polymerization to form smooth surface coatings,[70] which provides a suitable platform that allows accurate surface interaction measurement to be feasible.

The adhesion mechanism of catechol has been relatively well studied utilizing Atomic Force Microscopy (AFM) and Surface Forces Apparatus (SFA) techniques.[71-76] The single-molecular force spectroscopy measurement based on AFM technique reveals that the high strength, reversible and non-covalent interaction is coordination mechanism instead of hydrogen bond.[71] And local chemical environment, surface roughness and the presence of other impurities could also significantly affect DOPA adhesion.[72] Besides AFM technique, the SFA technique using mussel foot protein coated mica surfaces either in symmetric or asymmetric configurations under various aqueous conditions proves that the adhesion could be influence by the type of protein tested, the surface chemistry, the contact time, the oxidation state of DOPA groups and the type of metal ions in the environment.[74-76] Recent SFA study also indicates that catechol and amine have a synergistic interplay in wet adhesion and substrate-independent coating ability. However, the detailed role of amine groups is still not clear. [68, 77]

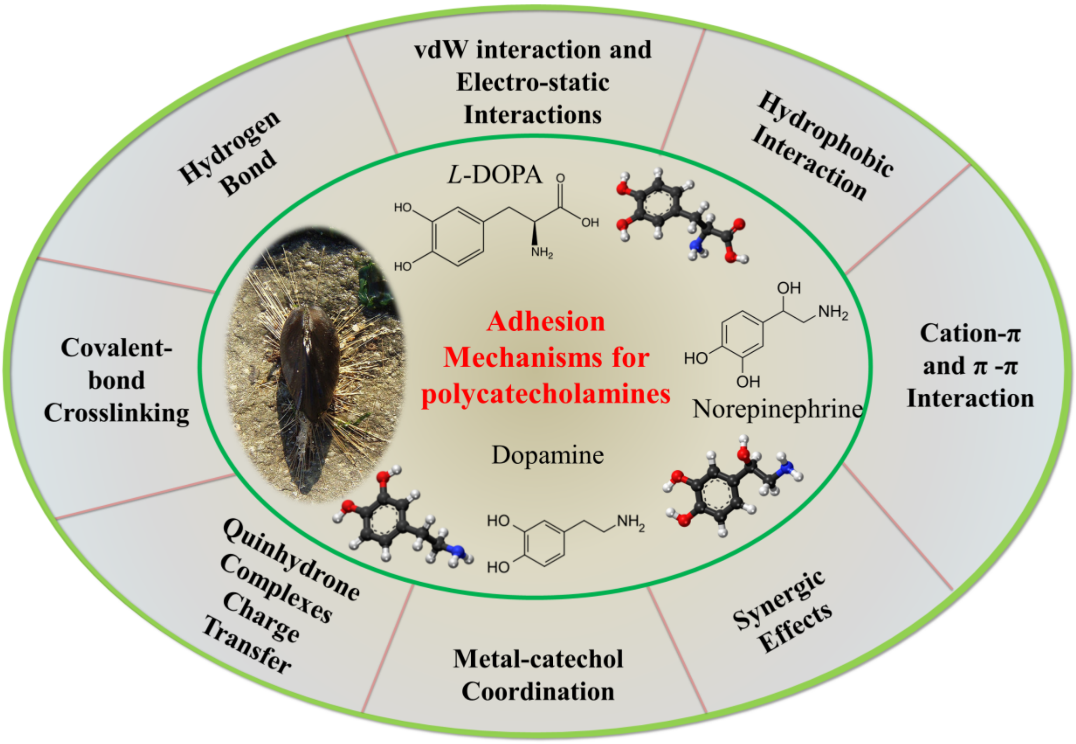

Figure 1.10 Major driving mechanisms for polycatecholamines coatings attached onto various kinds of substrates.

Extensive studies have been conducted on mussel-inspired underwater adhesion and lots of mechanisms have been proposed for explaining the substrate-independent coating ability of catecholamines. Herein we briefly summarized the mainly driving mechanisms for this specific coating method, which are shown schematically in Figure 1.10.

a) Hydrogen bond. This interaction is a non-covalent bond that plays an essential role in the initial stage of molecular assembly, and it enables the catecholamines compounds to compete with water molecules when adsorbing onto surface. A scanning tunneling microscopy study conducted by Diebold *et al.* suggests that catechol groups can form two types of hydrogen bond structures on TiO_2 (110) surface, either monodentate structure only or mixed monodentate–bidentate structures. The two structures can easily convert from one to the other through proton exchange.[78, 79] And the oxygen atoms of oxide materials such as mica and silica could also form hydrogen bonds with the phenolic -OH groups.[80]

b) Metal-catechol coordination and chelation effect. Waite *et al.* reported the coordination between Fe^{3+} and catechol could significantly contribute to the hardness and high extensibility of the cuticle of mussel byssal threads.[81] The chelation between catechol groups and trivalent Fe cations can even induce considerable adhesion of non-adhering mfps such as mfp-1.[74] Besides that, the chelation of Ti (IV) by catechol in aqueous solution has also been studied decades ago.[82]

c) π-π interaction. This interaction is a type of quadrupole–quadrupole interaction between aromatic rings of indolic and catechol-phenyl complexes/polymer layers, and this kind of interaction could facilitate the intra-layer cross-linking and polymerization of catecholamine compounds. The π-π-interaction has an important contribution to the stability of proteins in biological systems since this interaction provides a significant amount of binding enthalpy.[83] And it has also been reported that π-π interaction could be employed for preparing mesoporous pDA nanoparticles.[84]

d) Cation-π interaction between positively charged amine groups, the indolic crosslinks and other electron-rich π system. This kind of interaction is a monopole–quadrupole electrostatic forces that widely present between positively charged ions and an electron-rich π system.[85] The cation–π interactions are related to lots of important biological phenomena such as protein folding, potassium channel blockers, nicotinic acetylcholine receptors.[86] Mussel foot proteins are overall cationic in salted sea environment and recent SFA results proved that cation–π interaction is critical to achieve strong underwater adhesion and cross-linking.[87] And our recent study even proved that this short-range cation–π interaction is strong enough to induce a like-charged coacervation, viz. liquid-liquid phase separation, of two positively charged polyelectrolytes by overcoming the longer-range electrostatic repulsion in aqueous environment.[88]

e) Covalent-bond cross-linking. It has been reported that both Schiff base reaction and Michael addition reaction involving quinone groups of oxidized dopamine with nucleophilic groups like amine and thiol groups could proceed during the polymerization of catecholamine compounds.[18,63,78]

f) Quinhydrone complexes charge transfer. Spectroscopic and crystallographic study of polydopamine structure proved that this kind of interaction is a prominent feature of the non-covalent supramolecular structure and supramolecular interactions.[63,89,90]

g) Synergic effects. A recent study suggested that the catechol and amine groups could synergistically enhance interfacial adhesion. The lysine groups appear to displace hydrated potassium ions on mica surface, thus facilitate further chelation and attaching of catechol groups onto mineral surfaces.[77]

h) Other interactions such as vDW interaction, surface charge related electrostatic interactions, hydrophobic interaction between hydrophobic surface and hydrocarbon chains, which have been described in previous sections, could all contribute to the underwater adhesion of catecholamines.

Although we mentioned the above mechanisms separately, some of those mechanisms could happen simultaneously for each coating step. For a typical polycatecholamine deposition process on a smooth surface, those non-covalent interactions such as vDW force, hydrogen bonding, coordination and chelation effect, hydrophobic interactions and electrostatic interaction could play dominant role for the initial coating step especially for metal and metal oxide surfaces. Later on, other interactions like intra-layer π-π-interactions, cation–π interactions, covalent-bonding formation and cross-linking could take over along with other interactions at the same time. The above paragraphs briefly summarize the adhesion/cohesion mechanisms for catecholamine coatings. A number of review papers have also been published regarding polydopamine or polycatecholamine inspired coatings, which include their chemical property structure and applications.[18,63,90-92] For more detailed information on DOPA chemistry and polycatecholamine coatings, we can proceed to those excellent review papers.

1.6 Objectives and Outline of Thesis

Great efforts have been dedicated to preparing functional coatings on various kinds of surfaces with controlled hydrophobicity over the past few decades. However, the fundamental understanding of the deposition mechanisms of these coatings and related surface interactions remains incomplete. Therefore, the major objective of this proposed research is to develop stable, hydrophobicity-tunable, multi-functional coatings, study the deposition mechanisms of those coatings materials and understand related surface interactions using nano-mechanical techniques such as SFA and AFM. Four types of coatings have been chosen for studying in this thesis, including cross-linked hydrocarbon silane (*e.g.*, octadecyltrichlorosilane, OTCS) coating, end-grafted (poly(pentafluorophenyl acrylate)-*b*-polystyrene, PPFPA-*b*-PS) polymer coating, layer-by-layer deposited polyethyleneimine (PEI) and PPFPA-*b*-PS multi-layer coating and mussel-inspired polycatecholamine (*e.g.*, polynorepinephrine, pNE) coating. The detailed objectives are listed as follows.

(1) Systematically investigate the deposition behavior of alkylsilanes (*e.g.*, OTCS) on substrates with low density of reactive sites (i.e. freshly cleaved mica) *via* the vapor deposition method. Probe the surface interactions on silane vapor functionalized mica surfaces using SFA-force measurement.

(2) Systematically elucidate the preparation of hydrophobicity tunable, stable end-grafted hydrophobic block *co*-polymer (i.e. PPFPA-*b*-PS) surface on atomic smooth mica surface and study the effect of various factors such as hydrophobicity, salt concentration and degassing on the surface interactions between end-grafted polymer surfaces.

(3) Prepare stable polymeric films based on covalent bonding between active ester polymer, PPFPA-*b*-PS, and amine-rich polymer, PEI, using spin casting

layer-by-layer deposition and then combine with other post-treatment methods (*e.g.*, fluorination, grafting dyes) to achieve multi-functional properties. The surface interactions between obtained multi-layer polymeric films under aqueous solutions will also be investigated by using the SFA technique.

(4) Systematically study the effect of amine groups on the polymerization and surface interaction of mussel-inspired polycatecholamine coatings (*e.g.*, pNE) in aqueous solutions.

It is expected the successful outcomes of the proposed research will not only enhance the fundamental understanding for the deposition mechanism of those coating materials, surface interactions of coating surface, but also provide new insights into the development of advanced polymeric materials and nano-materials.

The outline of the thesis is provided as follows:

1) In chapter 1, I briefly reviewed the definition and classification of hydrophobic and hydrophilic surfaces. Then we spent some efforts on explaining the DLVO forces that including vdW force and electric double layer force, and several typical non-DLVO forces such as polymer steric repulsion, attractive bridging, depletion force and hydration repulsion. Later on, I generally reviewed the discovery and possible origin of hydrophobic interaction between hydrophobic surfaces. In the last part, I briefly reviewed the preparation and adhesion mechanisms of hydrophilic mussel-inspired polycatecholamine coatings on solid substrates.

2) In Chapter 2, I briefly introduced the techniques that were employed for my

research, especially focusing on the SFA technique. The contact mechanism and adhesion of elastic surface including JKR theory and contact mechanics test have also been described. Besides that, we also briefly reviewed three kinds of topography imaging modes for AFM technique, X-ray photoelectron spectroscopy, ellipsometry, spin coating, secondary ion mass spectrometry and scanning electron microscope.

3) In Chapter 3, I have systematically investigated the deposition behaviors of the hydrocarbon silane, octadecyltrichlorosilane (OTCS), on model mineral substrates (fresh mica) with few active sites *via* a vapor deposition method. Further investigation on the interaction forces between the as-obtained silane-functionalized mica under various conditions using SFA technique is illustrated and explained.

4) In Chapter 4, I reported the preparation of homogeneous, hydrophobicity tunable, stable poly(pentafluorophenyl acrylate)-*b*-polystyrene (PPFPA-*b*-PS) layers covalently end-attached onto mica surface using a “graft to” methodology. The interactions between the grafted-polymer surfaces in aqueous solutions were studied using the SFA technique. Various factors, including hydrophobicity, salt effect, degassing were examined and the origin of the long range forces have been discussed.

5) In Chapter 5, I reported an efficient way of preparing multi-functional polymer films based on covalent bonding between active ester, (polypentafluorophenylacrylate-*b*-polystyrene, PPFPA-*b*-PS) and amine-rich polymer (polyethyleneimine, PEI) using spin casting layer-by-layer (LbL) deposition. Other post-treatments have also been conducted on the polymeric films to achieve

multi-functional properties. SFA technique was employed to investigate the surface interactions between spin deposited PEI and PPFPA-*b*-PS multi-layer surfaces under aqueous solutions. A freestanding film with excellent stability, transparency has been obtained based on the multi-layer polymeric film.

6) In Chapter 6, I described the research on the deposition and polymerization of poly-dopamine, poly-norepinephrine and poly-pyrocatecol on fresh cleaved mica surface under base conditions, respectively. And the systematically study about the effect of amine groups on the polymerization and surface interactions of catecholamine reagents has been conducted by using nano-mechanic techniques such as SFA.

7) In Chapter 7, a brief summary regarding previous research results has been provided. Future directions that can be done are also mentioned.

CHAPTER 2

EXPERIMENT TECHNIQUES

In this chapter, the experiment techniques that have been used for my research will be presented briefly, which include surface forces apparatus, multiple-beam interference technique, atomic force microscope, ellipsometry, X-ray photoelectron spectrum, spin coating, scanning electronic microscope, contact angle and secondary ion mass spectrometry.

2.1 The Surface Forces Apparatus

Surface Forces Apparatus (SFA) has been widely used for direct measuring intermolecular and surface forces for numerous biological and non-biological systems in vapors and liquids for decades. This technique allows accurate and direct determination of forces between two surfaces as a function of separation distance with force sensitivity down to 1 nN and the distance resolution down to 0.1 nm.[93] The prototype of SFA was first described by Tabor and Winterton at 1969, and the separation distance of the two surfaces could reach as low as 5-30 nm with a resolution of ca. 0.3 nm.[94] Later, Israelachvili *et al.* further improved the SFA technique not only to measure the forces in a longer range in air (>100 nm), but also make it possible to measure surface forces in liquid medium.[94-96] Overall, the SFA technique has provided significant mechanistic insights into interaction mechanisms of various kinds of surfaces. Direct measurement of various kinds of surface forces have been reported, such as van der Waals forces, [94] electrostatic forces,[97] adhesion forces,[24] hydrophobic interactions,[30] steric interactions,[98] specific biological interactions,[99] friction and lubrication forces,[100] with angstrom resolution for separation distance and nano-newton force precision in both vapors and liquids.

2.1.1 Structure of Different SFA Models

Early version of SFA has been developed and is only applicable for measuring the normal forces. The Surface Forces Apparatus developed by Israelachvili in 1970s is called the SFA MK I.[96] Later improved model type MK II, MK III have also been developed, and in those modified models, the single cantilever spring disk holder was replaced with a double cantilever spring to prevent the surfaces from rotation or tilting during forces measurement; moreover, the upper surface could move in the lateral direction using a motor-driven micrometer which allowed the lateral force measurement to be feasible. A schematic diagram of the SFA MK III is shown in Figure 2.1. Three different levels of control could be achieved using this system: a) micrometer to millimeter distance control by using a micrometer; b) nanometer distance control driving through electric motor, c) angstrom (Å) precision control using piezoelectric ceramics. The MK III system has a small chamber that could be easily sealed, which facilitates the experiments where surfaces are needed to be completely immersed in liquid media. Moreover, the MK III is more stable to thermal drifts and the chamber design makes it very stable and linear during measurement.

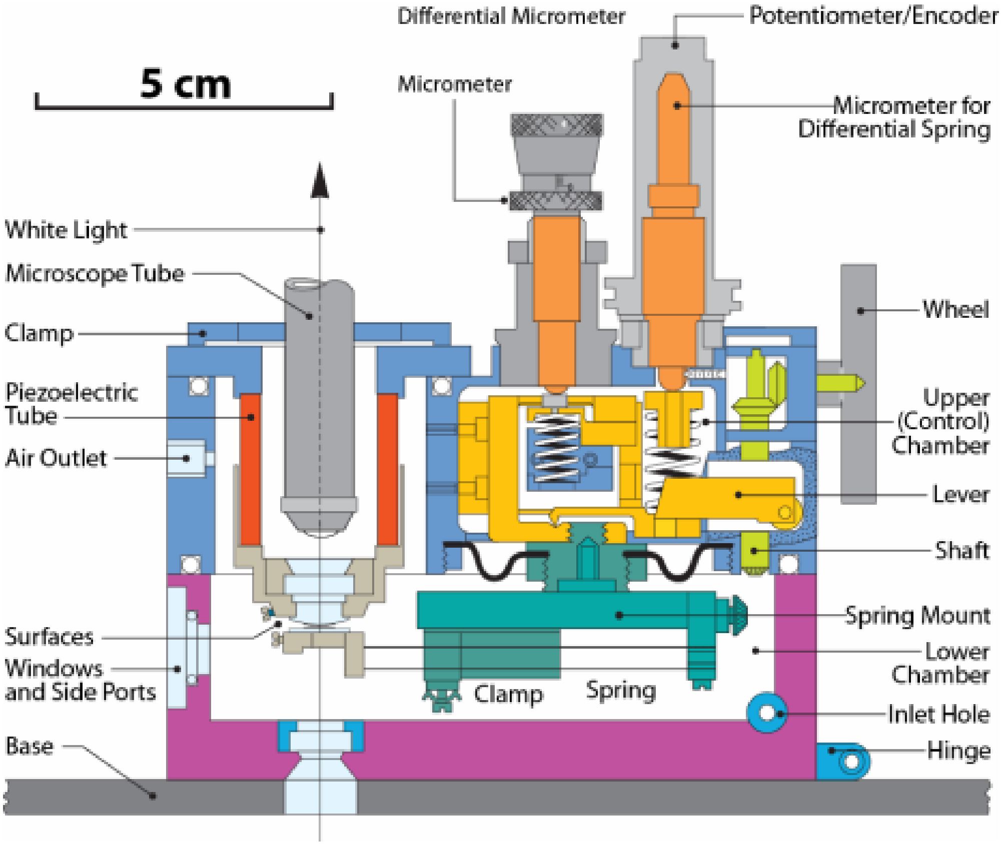

Figure 2.1 Schematic section view of the SFA MK III.[101]

The MK III system has the merits of extensible, good vertical and linear motion of the lower surface and reduced thermal drifts, however, the main translation stage is very difficult to machine and the lower chamber is too small to add new attachments. Those drawbacks have lead to the design of a new version of SFA, the so called SFA 2000, which is able to measure both normal force and lateral forces in a wide range of applications.

The SFA 2000 is easier to fabricate, assemble, operate and has fewer parts as compared to MK III. More importantly, the much larger chamber of SFA 2000 is able to accept numerous attachments such as bimorph slider, bimorph vibrator, 3D translation stage, rotating high-speed disk, which further extend the functionality of SFA.[93]

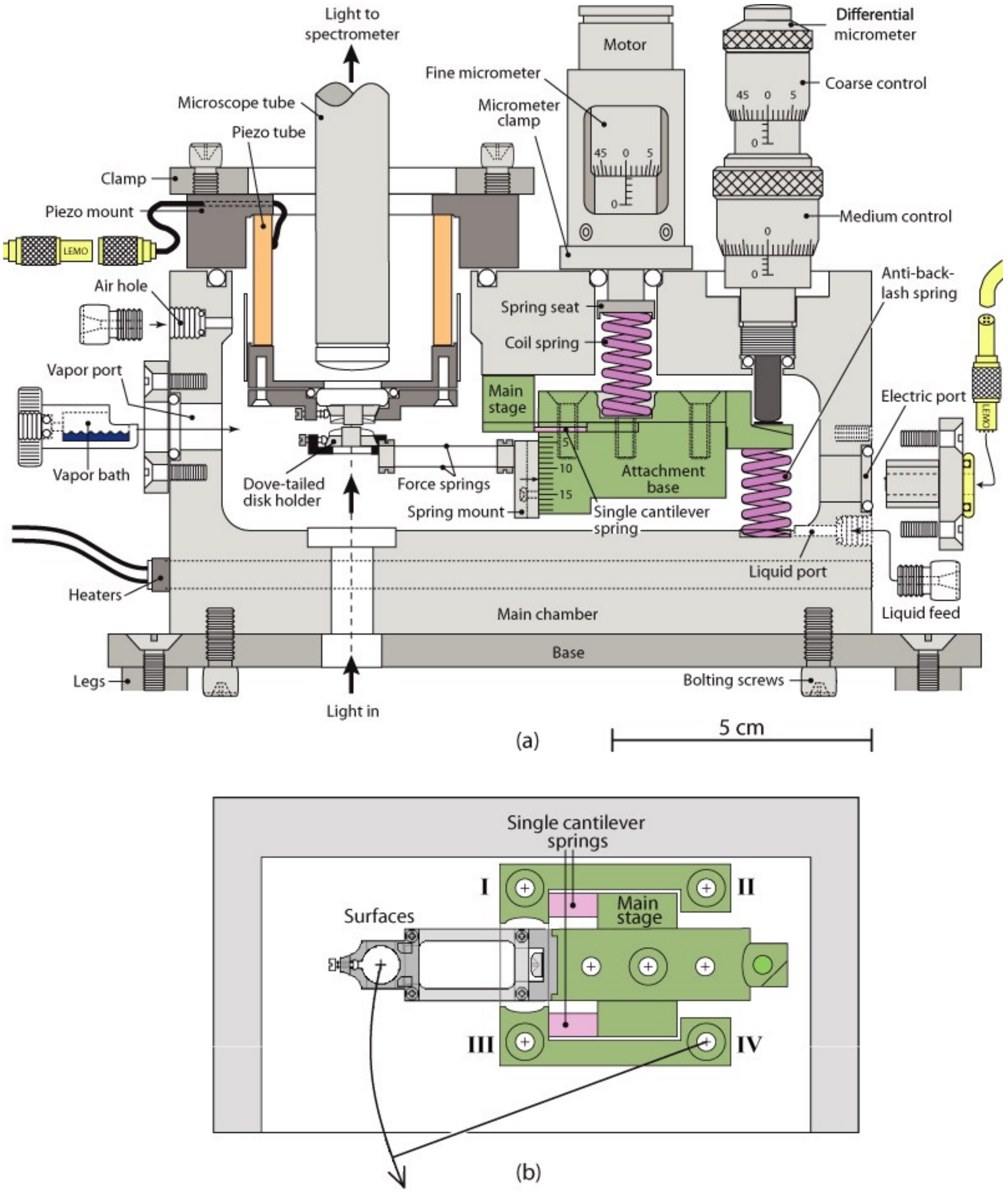

Figure 2.2 (a) Section view of the SFA 2000 main body through the center of the apparatus, (b) top view of the main stage and lower disk holder.[93]

Figure 2.2 shows the section profile of a typical SFA 2000 main body and a top view image of the newly designed sample holder. The main body of SFA 2000 system includes micrometers, the main stage containing the central single-cantilever spring, lower double-cantilever spring disk holder, upper disk holder with a piezoelectric tube for fine control, and a fully sealable chamber.[93] Similar to MK III system, the separation distance between two interacting surfaces can be controlled at three levels: by differential micrometers over a range of ~2 mm with ~50 nm precision (the coarse and medium control), by a motor-driven fine micrometer over a range of >10 μm with a position accuracy of 0.2 nm (the fine control), or by a piezoelectric tube over a range of 1 μm with <0.1 nm precision (the extra-fine control).

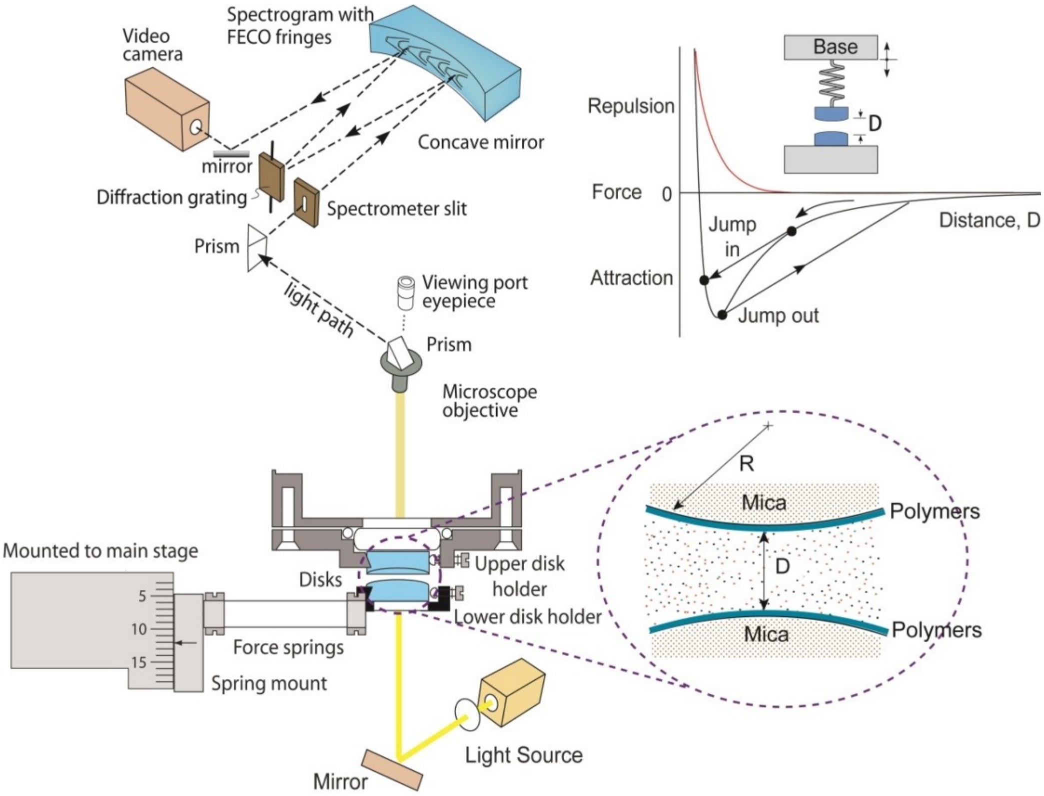

Figure 2.3 Schematic of SFA setup showing the light path in a typical SFA 2000 experiment. The right top figure shows the schematic force-distance curve which contains both jump in and jump out.[93]

Mica is a commonly used supporting substrate in SFA experiments due to its molecularly smooth feature at large scale (centimeters). The surface chemistry of mica can be readily modified by various physical or chemical methods, such as spin coating polymer layers, self-assembly of surfactant or polymers through Langmuir–Blodgett deposition, surface initiated polymerization and so on. Figure 2.3 shows the schematic view of SFA setup in a typical SFA normal force experiment. Generally, two back silvered mica sheets with coated polymer layers were glued onto two cylindrical silica discs of radius R and were mounted into the main chamber in a crossed-cylinder configuration. For typical surface force measurement carried out under aqueous conditions, the desired solutions will be injected into the gap of two disks. When the separation distance of two curved surface was much smaller than the radius of the curvature, it is equal to a sphere with the radius of R approaching a flat surface.[1] According to Derjaguin approximation,[1] the measured force, F, can be converted into energy per unit area (W(D)):

$$F(\mathrm{D})=2\pi R W(\mathrm{D}) \tag{2.1}$$

When white light is reflected by a flat mirror and directed normal to the silvered mica surfaces, the light will be reflected back and forth between the silver layers. Therefore, Newton's rings will be created by the transmitted light near the closest contact point between the surfaces as can be seen through a microscope objective. The transmitted light corresponds to a particular set of discrete wavelengths that is made visible by a spectrometer and are the so-called fringes of equal chromatic order

(FECO). [93,102] The FECO images can be applied for calculating the actual separation distance of two surfaces and the refractive index of the medium confined in between, which will be mentioned in the following section of this chapter.

Figure 2.3 also shows the schematic force-distance curves obtained by the SFA technique. During the measurements, the lower surface supported by a 'force spring' with a spring constant of k is moved by a distance $\Delta D_{\text{applied}}$ towards the fixed top surface driving electric motor, and the actual surface separation distance ΔD, during experiment is monitored and measured by calculating the shift of FECO fringes.[102] Therefore, the normal forces between the surfaces in various vapors or liquid media can be obtained using Hooke's law,

$$F(\mathrm{D})=k\,\Delta \mathrm{x}=k\,(\Delta \mathrm{D}_{\text{applied}}-\Delta \mathrm{D}) \tag{2.2}$$

It is worth mention that due to the lower effective spring constant k as compared to the maximum slope of the force-distance curve, the jump instabilities occurs at the positions that are shown as an inward jump in on approach curve and an outward jump out on separation curve. It will result in inaccessible regions due to the instability of force spring. Thus, a more stiff spring can be replaced in the SFA 2000 system so as to build the full force profile. And if the spring stiffness reached infinite, viz., $k=\infty$, although there will be no more instabilities on approach or separation, no equilibrium could be reached at separation distance between the jump in and jump out points either. [1,93]

2.1.2 Fringe of Equal Chromatic Order (FECO)

In order to measure the separation distance of two surfaces with high accuracy (~1 nm), the optical multiple-beam interferometry (MBI) technique also known as Fringes of Equal Chromatic Order (FECO) is applied in a SFA technique. Initially, the MBI technique was developed for characterization the topography of single surface, and later it was extended to the areas including SFA technique for accurate distance measurement.[102, 103, 104, 105]

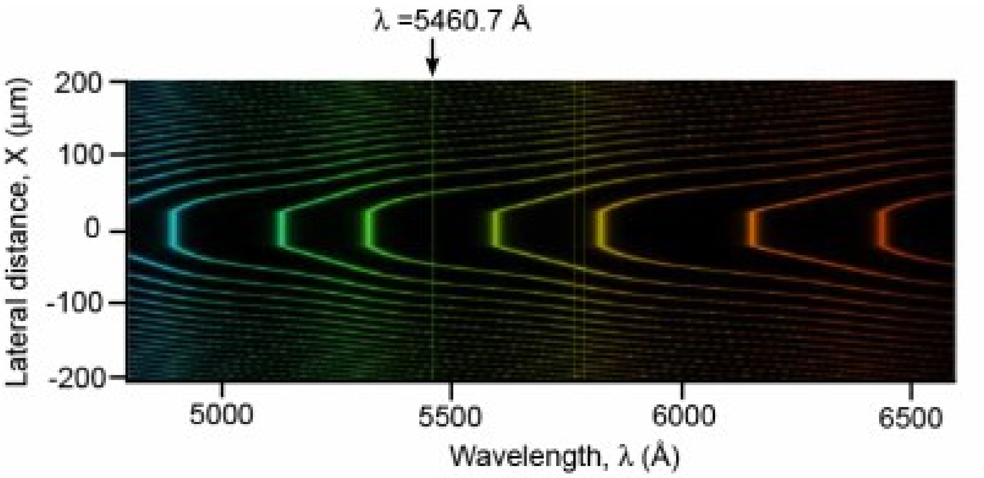

Figure 2.4 Typical FECO fringe image recorded using a color camera, the indicated λ at 5460.7 Å is the reference green line produced by a mercury lamp.[101]

Figure 2.4 shows the colored fringes produced by the MBI technique in a typical SFA experiment. In order to acquire clear and high quality FECO patterns, the top of transparent surfaces (*e.g.*, fresh cleaved mica) are coated with a reflective layer such as silver with the thickness to be around 50 nm, which acts as a mirror and also allows light passes through. When intense white light is passing normally through two silver surfaces and reflecting back and forth by silver layers before it leaves the interferometer. Only certain wavelengths could pass through during the reflective process, so the exit beam consists of a series of discrete wavelengths. By using a grating spectrometer, these wavelengths could be split up and captured using a camera, which is shown in detail in Figure 2.4.

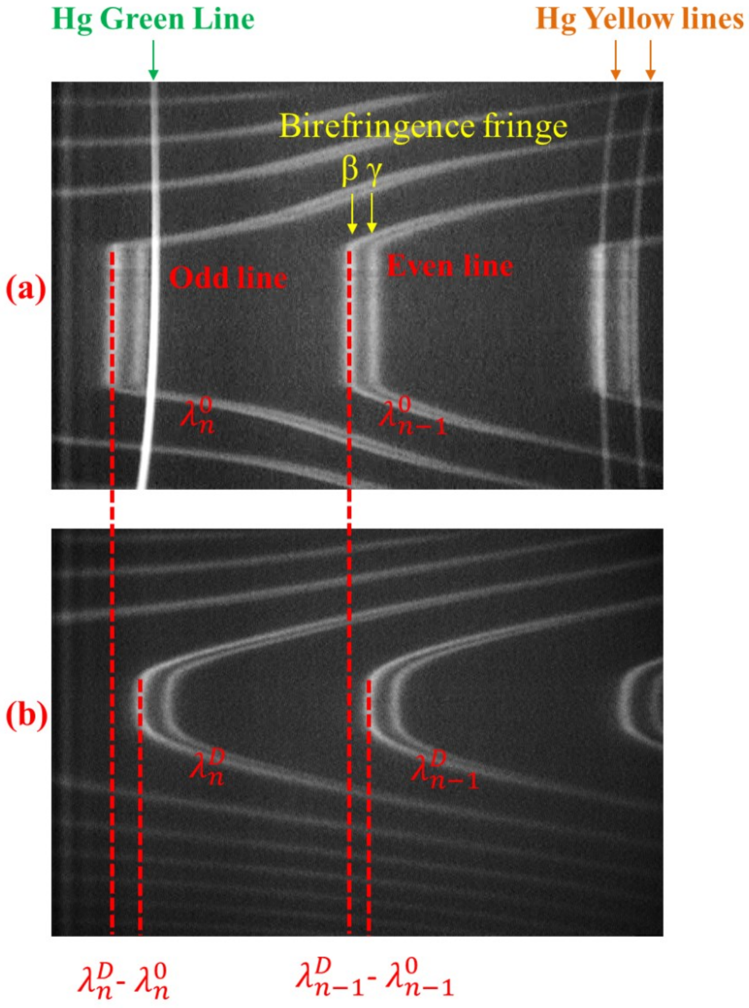

Figure 2.5 FECO pattern of mica-mica surface under adhesive contact (separation distance D = 0) in air (a) and (b) separated by a layer of lubricant film (D ~ 20.2 nm) under finite compress load during friction force measurement. The dark and grey color is due to the black and white camera used for capturing FECO fringe.

In my experiments, the mica-medium-mica is the common configuration being used, thus, we will only discuss the calculation method based on this three layer model. Figure 2.5 shows a typical FECO pattern between two mica surfaces in adhesive contact in ambient condition (Figure 2.5(a)) and separated by a layer of lubricant with the thickness D to be ~20 nm (Figure 2.5(b)).

Here we will briefly introduce how to calculate actual separation distance D using FECO fringes. Firstly, we can determine the Fringe order *n* using Equation 2.3,

$$n= \lambda_{n-1}^{0} / (\lambda_{n-1}^{0} - \lambda_{n}^{0}) \tag{2.3}$$

where λ_{n-1}^{0}, λ_{n}^{0} is the wavelength of (n-1) and *n*th order of FECO fringe, respectively. The birefringence of mica results in a doublet appearance (β- and γ -component) of the FECO fringe. The Hg green line at 546.74 nm and yellow lines at 576.96 nm and 579.66 nm are generally used for calibration during measurement. The flat front of the FECO fringe reflects the shape and size of contact area.

For mica-mica contact, if the two mica surfaces have the same thickness *T*, then *T* can be calculated by using the wavelength of the *n*th order fringe λ_{n}^{0} using Equation 2.4, and μ_{mica} is the reflective index of mica.[102]

$$T= n\lambda_{n}^{0} / 4\mu_{\text{mica}} \tag{2.4}$$

When the two mica surfaces are separated by a distance *D*, the *n*th fringe wavelength changes from λ_{n}^{0} to λ_{n}^{D}, which is shown in Figure 2.5(b), the separation distance *D* can be determined by Equation 2.5,

$$\tan\left(\frac{2\pi\mu D}{\lambda_n^D}\right) = \frac{2\bar{\mu}\sin\left(\mathrm{n}\mathrm{F}_n\pi\Delta\lambda_n/\lambda_n^D\right)}{(1+\bar{\mu}^2)\cos(\mathrm{n}\mathrm{F}_n\pi\Delta\lambda_n/\lambda_n^D)\pm(\bar{\mu}^2-1)} \quad (2.5)$$

where in this equation, $\bar{\mu} = \mu_{\mathrm{mica}} / \mu$, μ and μ_{mica} are the refractive index of medium and mica, respectively, λ_n^D are the wavelength of the *n*th FECO fringe with a separation distance *D*, $\Delta\lambda_n$ is the wavelength change as compared to adhesive contact of mica, $\Delta\lambda_n = \lambda_n^D - \lambda_n^0$, $n\mathrm{F}_n = \lambda_{n-1}^0 / (\lambda_{n-1}^0 - \lambda_n^0)$, λ_n^0 and λ_{n-1}^0 are the wavelength of *n*th and *(n*-1*)*th FECO fringe, *n* is the fringe order and F_n can be considered as a correction factor due to the phase changes at the mica-silver interface and the dispersion effects.[93, 101] The "+" sign is taken for odd and "–" is taken for even for Equation 2.5.

By using the optical multiple-beam interferometry, the SFA technique can provide information on the confined film thickness between the two surfaces (also called "hard-wall" distance) which does not appear to significantly change with increasing the normal load or pressure as well as force-distance profiles. The confined polymer film thickness mostly depends on the properties of molecules and substrates (*e.g.* molecular weight, rigidity of chains and surface roughness) and adsorption states (*e.g.* grafting density, conformation) which can be affected by the solution environment.

2.1.3 Contact Mechanics of Surfaces

The adhesion forces between different surfaces are important for understanding various rheological and interfacial phenomena (especially for highly deformable materials) such as surface adhesion, wear, agglomeration of colloidal particles.[28] The research on contact mechanics and adhesion mechanics has steadily progressed for over one century, beginning with the pioneering work done by Hertz in 1882,[1] followed by the Johnson-Kendal-Roberta (JKR) theory,[106] Derhaguin-Muller-Toporov (DMT) theory[107] and Maugis model.[108] These classic models well describe the adhesion and deformation of two curved purely elastic surfaces. [109, 110] The JKR theory and DMT theory predict the adhesion force F_{ad} between two curved surfaces of radii R_1 and R_2 as given in Equation 2.6 and Equation 2.7, respectively.

$$\text{JKR model: } F_{\mathrm{ad}}=(3/2)\pi R W_{ad}=3\pi R\gamma_{\mathrm{eff}} \tag{2.6}$$

$$\text{DMT model: } F_{\mathrm{ad}}=2\pi R W_{ad} \quad =4\pi R\gamma_{\mathrm{eff}} \tag{2.7}$$

$$R=R_1R_2 \;/\; (R_1+R_2) \tag{2.8}$$

where R is the equivalent radius and W_{ad} is the work of adhesion per unit area, γ_{eff} is the effective surface adhesion energy. The JKR theory is usually applicable to soft materials with large surface energies and radii, and the DMT theory applies to small, rigid spheres (or asperities) with low surface energies.[25] For deformable soft materials, the adhesion energy per unit area (W_{ad}) can be correlated to the adhesion force F_{ad} by $W_{ad} = F_{ad} / 1.5\pi\mathrm{R}$.[106]

For a typical contact mechanics test using the SFA technique, the two surfaces were firstly brought into adhesive contact in air by electric-motor, and then finite compressive load was applied using a differential micrometer. The contact diameter was monitored through FECO fringes change in real time.

According to the classic JKR theory, the contact diameter change of a purely elastic sphere of radius R, when pressed by a load L against a flat surface can be well fitted by

$$r^3 = \frac{R}{K}(F_{\perp} + 3\pi RW + \sqrt{6\pi RF_{\perp}W + (3\pi RW)^2}) \tag{2.9}$$

$$K = \frac{3(1-\nu^2)}{4E} \tag{2.10}$$

where r is the contact radius measured by monitoring FECO (Fringe of Equal Chromatic Order) change in real time, $F_{\perp}$ is the normal load applied during contact mechanics measurement, v is Poisson's ratio, E is the Young's modulus of the surface material, K is the equivalent modulus calculated by Equation 2.10. For typical adhesive systems during JKR tests, the loading-unloading force curves generally do not overlap and results in an adhesion hysteresis as

$$\Delta\gamma=\gamma_R-\gamma_A \tag{2.11}$$

where γ_A is the surface energy measured during loading process, γ_R is the surface energy measured during unloading process.

2.2 The Atomic Force Microscope (AFM) Technique

AFM is a very sensitive technique for acquiring information about the surface morphology and force interactions with high spatial resolution.[111] As shown schematically in Figure 2.6a, the AFM setup typically includes five parts: a cantilever with tip (force transducer), piezoelectric tube (PZT) scanner, laser diode, photodiode detector, and feedback control circuit. The AFM technique has been widely applied for imaging surface topography as well as molecular force measurements with typical force sensitivity of 10-100 pN, which makes single molecular force measurement feasible.[25, 111] Unlike electron-microscopy samples, the samples for AFM study normally do not require any special pretreatment (i.e., gold or carbon coating). Importantly, the AFM technique could also work under aqueous environment, which greatly enlarges its scope for scientific research.

Typically there will be three different modes for AFM imaging: the contact mode, non-contact mode and tapping mode. For contact mode, the AFM tip is in close contact with the sample surface. Pushing the tip against the sample surface will lead to a repulsive force which results in the deflection of the cantilever. Silicon nitride tips are commonly chose for this mode. An electric feedback loop is generally employed to restore the desired value of deflection. The disadvantage of contact mode is that AFM tip may damage the sample surface especially when surface is soft and fragile, and the AFM tip could also get contaminated or easily become blunt after scanning.[111] For non-contact mode, AFM tips are generally hovers above the sample for certain distance (5-10 nm). The topographic images are constructed by employing van der Waals force acting between the tip and the sample surface. The non-contact mode does not have the issue of damage sample surface, however, the liquid meniscus layer developed under ambient conditions will greatly affect the resolution in this mode.[112,113] Thus, the third mode, tapping mode (also called dynamic contact mode, intermittent contact or AC mode) has been developed to overcome the above issues. In tapping mode, the cantilever is driven by a piezo to oscillate at or near its resonance frequency with a free amplitude from several nm to hundreds nm. The interaction forces such as vdW force, acting on the cantilever usually result in the decrease of amplitude of the cantilever. The feedback loop will adjust the height of tip to maintain constant oscillation amplitude (set point) as the cantilever is scanned across the sample surface.[114, 115] In tapping mode, the tip will slightly touch the surface, however, unlike contact mode, the oscillation amplitude is large enough to overcome the adhesion force between tip and sample. Additionally, the applied force is generally vertical and the effect of shear force could be minimized. The wide operation range of tapping mode would benefit the feedback system, leading to a more stable and reproducible imaging result.

In addition to topographic imaging, the AFM technique has the capability to measure force interactions. And various surface forces have been reported. For example, the AFM technique has been applied for measuring hydrophobic interactions,[116] colloid forces,[117] single molecule forces[118-120] and *etc*. The sketch map of the force curve (force-distance curve) is shown in Figure 2.6b with similar jump instabilities due to the finite spring constant of cantilever.

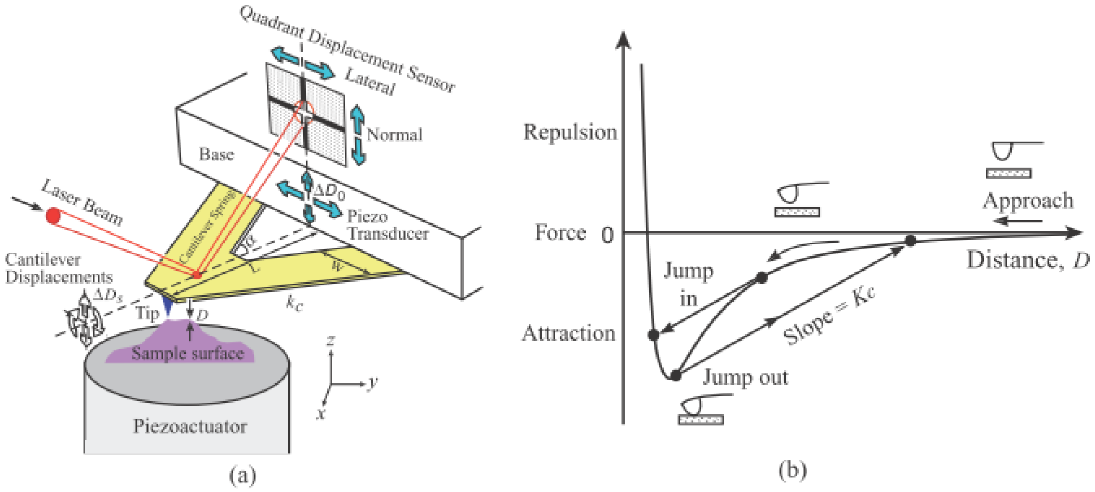

Figure 2.6 (a) Schematic of the working principle of an AFM and (b) typical normal force versus distance curve obtained using an AFM. [25]

In this thesis research, the tapping mode AFM will be frequently used to characterize the morphology of substrate surfaces before or after functionalized with chemicals so as to better understanding the deposition mechanisms. Herein a comparison between the SFA and AFM technique is given in Table 2.1. It is noted that the AFM technique has both the ability to conduct imaging and force measurement, while the SFA technique is only able to conduct force measurement between different surfaces, and the SFA technique is more suitable for soft materials such as proteins, because it is usually difficult for AFM to obtain the absolute separation distance, contact area and surface deformation during force measurements.

Table 2.1 A detailed comparison between SFA and AFM techniques

	SFA	**AFM**
Basic Principle for force measurement	**Hooke's Law: <u>F = *k*·ΔX</u>**	
Contact type	Local surface contact (tens of micro-meters)	Single asperity contact (tens of nano-meters)
Diameter of Contact Area	10 - 100 μm	10 - 1000 nm
Load range	< 500 mN	< 1 mN
Sample requirement	Smooth surfaces at nanometer scale	Relatively smooth surfaces at micrometer scale
Combined with other techniques	X-ray, Optical interference, *etc*.	Conductive measurement, interference microscopy, *etc.*
Slide velocity	0.001–100 μm/s	0.02–200 μm/s
Other Comments	Accurate distance by analyzing multiple-beam interferometry with an accuracy of ~ 0.1nm, low lateral resolution ~1μm	Real distance between tip and surface unknown, especially for soft materials
Applications	Surface forces (both normal and lateral) Nano-rheology	Different imaging modes, Force measurement, Conductivity , Nanotechnology

2.3 Other Techniques

Beside the SFA and AFM technique, other techniques such as X-ray photoelectron spectroscopy (XPS), ellipsometry, contact angle, spin coating, scanning electron microscopy, secondary ion mass spectrometry have also been used for my research, and I will introduce those techniques briefly in this section.

X-ray Photoelectron Spectroscopy (XPS) is a highly sensitive and quantitative spectroscopic technique for analyzing surface elemental composition, chemical state and electronic state of specific elements. [121] Typically, the samples are irradiated by a beam of X-rays, and the number and kinetic energy of escaped electrons with a depth of 0-10 nm are analyzed. Thus a typical XPS spectrum is a plot of the number of electrons detected versus the binding energy of the escaped electrons detected. XPS measurement usually requires high vacuum or ultra-high vacuum conditions and the detection limits for most of the elements are in the parts per thousand range.[122] For my experiments, the XPS measurements were conducted using Kratos Axis Ultra Spectrometer employing a monochromated Al Ka X-ray source ($h\nu = 1486.71$ eV). The pressure of analysis chamber during experiments was controlled below 5×10^{-10} Torr.

Ellipsometry is a commonly used optical technique for measuring the dielectric properties and thin film thickness. Basically, it measures the change of polarization for light upon reflection or transmission and compares it to a model to get fitted dielectric property and thickness.[123] This technique could measure samples with a thickness ranges from less than 1 nm to several micrometer with very good accuracy. And for my research, the ellipsometry technique was combined with the SFA technique to check the film thickness prepared by spin coating method. A VASE Ellipsometer (J.A. Woollam Co.) is used in a reflection mode for measuring thin film spin coated on silicon wafer with the scan wavelength changing from 200 nm to 1200 nm.

Contact angle measurement is a useful method to quantify the wettability of a solid surface by a liquid. The equilibrium contact angle mainly depends the interaction between the liquid, solid and vapor molecules.[124] Typically we use water contact angle on a surface to define the hydrophobicity of functionalized surface. In my research, a contact angle goniometer (Ramehart, USA) is used to measure the contact angle of water on functionalized mica or silica surface.

Spin coating is a widely applied method to prepare thin polymer films on flat substrates. For liquid with high viscosity such as photoresist, a static disperse method that added the liquid drop before spinning is generally applied. However, for liquid with low viscosity and poor wettability on substrate, the dynamic dispense method that added the solution during spinning would be more suitable. For a typical spin coating process, the thickness of prepared film mainly depends on the intrinsic property of the liquid such as viscosity, surface tension of the liquid, as well as the spin coating conditions such as spinning speed and duration time. Generally, the higher the rotation speeds is, the thinner the film will be. [101, 125] In my research, a KW-4A spin coating machine has been employed to prepared spin-assistant lay-by-layer assembling thin film. Due to the poor wettability and low viscosity of acetone and toluene on silicon, the dynamic disperse method is applied for my experiments.

The scanning electron microscope is capable of achieving high-resolution for conductive samples. Typically, the SEM images are generated by detecting the secondary electrons emitted from sample surface due to excitation by focused high energy electron beam.[126] Here for my research, a TESCAN tungsten SEM is employed to measure the surface morphology or spin-assistant layer by layer deposited polymer films.

Secondary ion mass spectrometry (SIMS) is a useful surface analyzing technique that is able to collect information about the composition of solid surfaces and thin films by sputtering the surface of the specimen with a focused primary ion beam, collecting and analyzing ejected secondary ions.[127] For my research, the SIMS technique has been used to detect the composition of polypyrocatechol coatings on substrates.

CHAPTER 3

OCTADECYLTRICHLOROSILANE DEPOSITION ON MICA SURFACES: THE INSIGHT INTERFACE INTERACTION MECHANISM

3.1 Introduction

Surface modification/functionalization by alkylsilanes can adjust the wettability and interactions of material surfaces. Alkylsilane coatings have been extensively exploited for many engineering applications, such as fabrication of superhydrophobic surfaces.[128-131] enhancement of the mechanic properties of nanocomposite materials and interfaces,[132-134] and fabrication of micro-/nanoelectromechanical systems. [135, 136] Alkoxysilanes and chlorosilanes are two groups of alkylsilanes with different reactive bonds of Si-OR and Si-Cl, respectively. Compared to alkoxysilanes, chlorosilanes are more susceptible to moisture and thus exhibit higher reactivity.[137, 138] “Solution deposition”[139] and “vapor deposition”[128, 140] are two commonly used methods to deposit alkylsilanes onto substrates. Compared to the “solution deposition”, the “vapor deposition” holds better flexibility and convenience in terms of its applicability to a broader range of substrates (*e.g.*, those sensitive to organic solvents in solution deposition), with potential engineering applications such as electronic devices and sensors. Previous reports have revealed that both deposition methods can make the alkylsilanes form an ordered and densely packed self-assembled monolayer (SAM) on substrates with high density of reactive sites (*e.g.*, hydroxyl groups), such as the Piranha-solution-oxidized silica/silicon.[134, 138, 139] However, in many practical cases, the active sites on the substrate surfaces are not sufficient to allow the formation of a perfect alkylsilane SAM. To the best of our knowledge, there is few report on systematical characterizations of the physicochemical deposition behaviors of alkylsilanes on substrates with low density of reactive sites.

Mica, comprising sheets of octahedral hydroxyl-aluminum sandwiched between two silicon tetrahedral layers, exhibits surface smoothness at the atomic level, which makes it especially suitable for the study of the small molecules deposition.[141, 142] Mica has been the most reliable and commonly used substrate for the measurement of surface interactions using surface forces apparatus (SFA) because of its translucency and surface smoothness at the atomic level. [93, 102, 143] In contrast to the oxidized silicon/silica, the freshly cleaved mica possesses much fewer reactive sites (*i.e.*, silanol groups) for the alkylsilane deposition, because one in four silicon atoms in the silicon layer of mica is replaced by an aluminum atom. It has been proved that the freshly cleaved mica only carries 11% silanol groups,[141] and high quality, monolayer coatings of triethoxysilane (i.e., 3-aminopropyltriethoxysilane) has been achieved *via* vapor deposition to pattern mica surfaces.[144] In this work, freshly cleaved mica is employed as a model substrate with low density of reactive sites to systematically characterize the deposition behavior of the highly reactive octadecyltrichlorosilane (OTCS) by using the vapor deposition approach. Subsequently, the surface interactions of the OTCS-modified mica surfaces were investigated by SFA in both air and aqueous media. The surface force measurements of the OTCS-modified mica not only help verify the deposition behavior of the alkylsilane on mica surfaces, but also provide pivotal understanding on the interactions between the as-prepared OTCS-modified surfaces with nanoscale roughness. Previous force measurements in this aspect mainly focused on the smooth and ordered SAM alkylsilane surfaces.[43],[145] The force measurements in this work based on the as-prepared (relatively rough) OTCS surfaces will provide useful insights into the interaction mechanisms of rough alkylsilane-modified hydrophobic surfaces that are normally obtained in practice, with implications on the surface bonding/adhesion and surface interactions when alkylsilane-modified hydrophobic surfaces are involved.

3.2 Materials and Methods

Materials

Octadecytrichlorosilane (95%), sodium chloride (anhydrous, 99.999%), glacial acetic acid (HAc, 99%) and hydrochloric acid (35%) were purchase from Sigma-Aldrich and used as received. Ruby mica sheets were purchased from S & J Trading Inc. (Glen Oaks, NY). Deionized water with a resistance of 18.2 $M\Omega \cdot cm^{-1}$ was used in all experiments.

Deposition of OTCS on Mica *via* the Vapor Deposition Method

Freshly cleaved mica sheets were placed into a vacuum desiccator (diameter of 230 mm, Bel-Art Scienceware) and 0.5 ml of OTCS was added into a PTFE container that was also placed in the desiccator. The desiccator was vacuumed for 30 min (~80 mm Hg), and then sealed and kept for varied times from half an hour to several days. Finally, after the desired deposition time was reached, the resulting mica sheets were taken out and washed with deionized water, dried with nitrogen flow and kept in vacuum desiccator before further measurements.

To prepare the samples used for the SFA measurements, two pieces of back-silvered thin mica sheets with thickness of around 1-5 μm were respectively glued onto two cylindrical silica disks with radius $R \sim 2$ cm. The mica surfaces supported by the silica discs were then coated with OTCS *via* the same method described above.

Surface Characterizations

The morphology of the OTCS modified mica surfaces was characterized with an Atomic Force Microscope (MFP-3D, Asylum Research, Santa Barbara, USA) under the Acoustic tapping mode. Silicon cantilevers (Bruker Nano) with a nominal resonance frequency of 300−400 kHz and spring constant of ~40 N/m were used for imaging. For the measurements in the aqueous solutions, thermal method was used to determine the resonance frequency peak of the silicon cantilevers.[146]

An SFA (SurForce LLC, Santa Barbara, CA, USA) was used to measure the contact mechanics of the vapor-deposited OTCS thin films in air and the interaction forces between OTCS-modified mica surfaces in aqueous solutions. The SFA technique provides an accurate and direct means to determine the interaction forces as a function of absolute separation distance between two surfaces with force sensitivity and distance resolution down to <10 nN and 0.1 nm, respectively.[1, 93, 147] The detailed experimental setup using the SFA system and its working principles can be found elsewhere.[93] To conduct the force measurements, the two silica discs with the OTCS-modified mica surfaces were mounted into the SFA chamber in a cross-cylinder configuration, of which the surface interaction is equivalent to a sphere with the same radius of R approaching a flat surface when the separation distance (D) is much smaller than the radii of curvature R.[1] For measurements in aqueous solutions, the desired solution was injected between the two surfaces. The film thickness and the absolute separation distance between the two surfaces can be *in situ* determined using an optical technique named Multiple Beam Interferometry (MBI) by employing fringes of equal chromatic order (FECO).[102] The measured force, F, between two curved surfaces (with a radius of curvature R) can be correlated to the energy per unit area (W(D)) between two flat surfaces based on the Derjaguin approximation (Equation 3.1).[1]

$$F(\mathrm{D})=2\pi RW(\mathrm{D}) \tag{3.1}$$

In this study, the contact mechanics tests were carried out under room temperature with a small container filled with P_2O_5 in the sealed SFA chamber to ensure the dry atmosphere condition. SFA was also applied to measure the interaction forces of OTCS modified mica surfaces obtained *via* different deposition times in 1 mM NaCl aqueous solutions of different pH values. The solution pH was adjusted by using HCl and NaOH solutions.

3.3 Results and Discussion

3.3.1 Surface Morphology of The OTCS-modified Mica

To study the deposition behavior of OTCS on mica surfaces, freshly cleaved mica sheets were exposed to the OTCS vapor for different times varied from 2 h, 8 h to 48 h. The as-obtained OTCS-modified mica surfaces are denoted as OTCS-2h, OTCS-8h and OTCS-48h henceforth, respectively. Figure 3.1 shows the morphology of the bare mica surface and the as-obtained OTCS-modified mica surfaces *via* different deposition times imaged by AFM. As shown in Figure 3.1a (5×5 μm^2) and Figure 3.1e (0.5×0.5 μm^2), the freshly cleaved mica surface is extremely flat and featureless with root-mean-square (rms) roughness less than 0.1 nm. After 2 h of OTCS vapor deposition, scattered tiny particles with height of ca. 0.2-1.0 nm and lateral dimension of ca. 10 nm were observed on the OTCS-2h surface (Figure 3.1b, 3.1f and 3.1i). With the prolonged vapor deposition time, the particles on the mica surfaces grew bigger and the surface coverage was increased. The height of the particles on the OTCS-8h was ca. 1-4 nm, and their lateral dimension ranged from several to tens of nanometers (Figure 3.1c, 3.1g and 3.1j). The OTCS-48h surface was covered by particle aggregates with height of ca. 5-8 nm and their lateral dimension could reach hundreds of nanometers (Figure 3.1d, 3.1h and 3.1k). The surface roughness of the as-obtained OTCS-modified mica surfaces also increased with increasing the deposition time. Specifically, the rms roughness of the OTCS-2h, OTCS-8h and OTCS-48h surfaces was respectively ca. 0.1 nm, 0.5 nm and 2 nm. Previous research indicated that the thickness of a closely packed SAM film of OTCS is around 2.6 nm.[138] In our case, the OTCS particles formed on the OTCS-modified mica obtained with shorter vapor deposition time (*e.g.*, 2h and 8 h) are not composed of closely packed and well aligned OTCS molecules, instead the OTCS molecules appear to be more randomly oriented. This can be evidenced by the fact that the height of the majority particles on the OTCS-2h and OTCS-8h surface is much smaller than 2.6 nm. Accordingly, the OTCS aggregates on the OTCS-48h surface comprises of several layers of aggregated OTCS molecules. Therefore, it can be concluded that the vapor deposition of OTCS on mica surfaces involves two stages: (i) OTCS molecules react with the reactive sites on the mica surfaces to form patchy structures; (ii) the initially deposited OTCS molecules continue to serve as nucleation/reactive sites for the upcoming OTCS molecules to deposit and graft to the nucleation sites and thus OTCS aggregates formed (see Figure 3.1h).

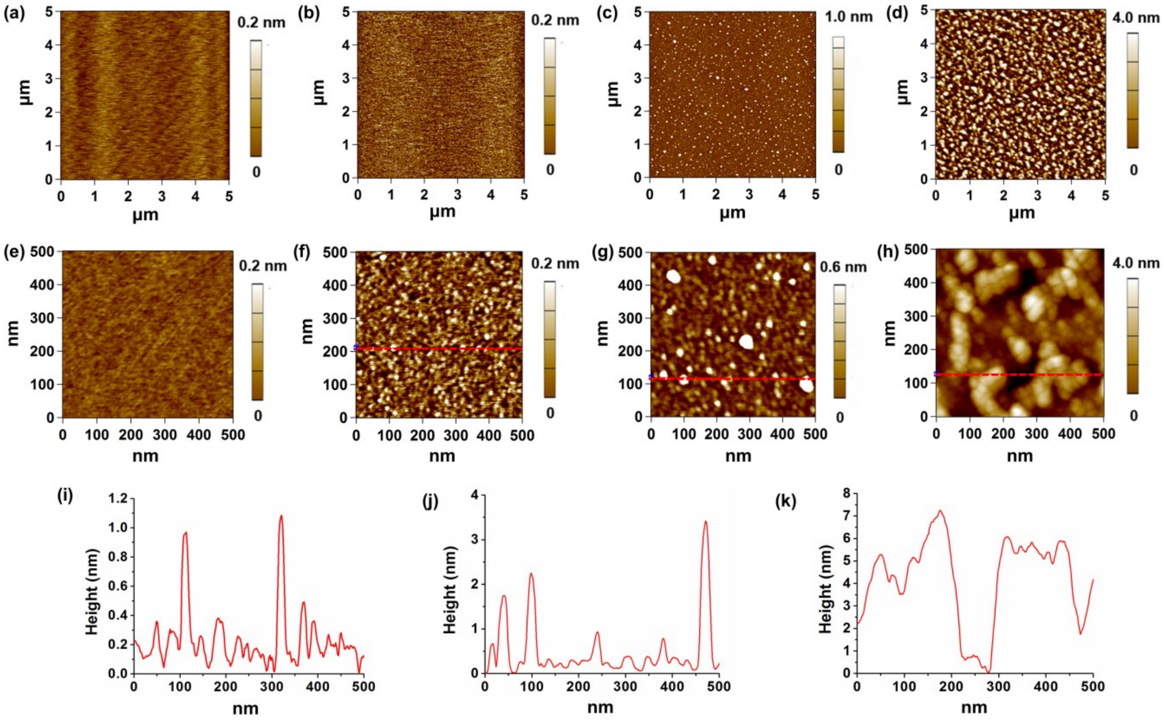

Figure 3.1 (a-h) Topographic AFM images of (a, e) freshly cleaved mica, (b, f) OTCS-2h, (c,g) OTCS-8h and (d, h) OTCS-48h surfaces. (i-k) Typical cross section line-scan profiles of (i) OTCS-2h, (j) OTCS-8h and (k) OTCS-48h surfaces, derived from the corresponding topographic AFM images (f, g and h).

3.3.2 Surface Hydrophobicity of the OTCS-modified Mica Surfaces

To further evaluate the deposition process of OTCS on the mica surfaces, the surface hydrophobicity of the as-obtained OTCS-modified mica was assessed by water contact angle (CA) measurements. Figure 3.2 shows the water CA of the OTCS-modified mica as a function of the OTCS deposition time (black line). Accordingly, three regions can be roughly identified from the CA evolution curve: (i) the rapidly increasing region, the water CA increases almost linearly from 0° to ca. 40° with the OTCS deposition time increasing from 0 h to 5 h, (ii) the slowly increasing region ranging from ca. 40° to ca. 85° with the OTCS deposition time increasing from 5 h to 35 h, (iii) the plateau region around 85°-90° when the deposition time is longer than 35 h. As indicated by the AFM images, the OTCS-modified mica exhibits a patchy surface composition that comprises of the bare mica and OTCS aggregates. Therefore, the water CA (θ_{eff}) of the OTCS-modified mica surfaces can be theoretically defined by the modified Cassie-Baxter equation:

$$\cos\theta_{\mathrm{eff}} = (1 - x_{OTCS})\cos\theta_{\mathrm{mica}} + R_f x_{OTCS}\cos\theta_{\mathrm{OTCS}} \tag{3.2}$$

where x_{OTCS} is the surface coverage ratio of the OTCS molecules on the mica surface, θ_{mica} and θ_{OTCS} respectively represent the water CA on a bare mica surface and a surface with ideally full coverage of OTCS, and R_f is the roughness factor. It has been reported that a bare mica surface exhibits superhydrophilicity with water CA of ca. 0° and the water CA on a self-assembled OTCS monolayer surface is ca. 112°. [135,138] Accordingly, by defining θ_{mica} and θ_{OTCS} to be 0° and 112° in Equation 3.2, respectively, the surface coverage ratio of the OTCS on the OTCS-modified mica surfaces at different deposition stages was estimated and depicted in Figure 3.2 (blue line, assuming the roughness factor R_f to be 1). Specifically, the as-calculated surface coverage ratio of the OTCS molecules on the OTCS-2h, OTCS-8h or OTCS-48h surface is estimated to be 3%, 28% and 66%, respectively. It is worth pointing out that there can be a slight disparity between the estimated and actual surface coverage of the OTCS molecules, especially for the long deposition time case (CA > 85°) when the effect of surface roughness become non-negligible. It should be also noted that the orientation of OTCS molecules on the as-obtained surfaces might not the same as that of the closely packed self-assembled OTCS monolayer reported previously. [135, 138]

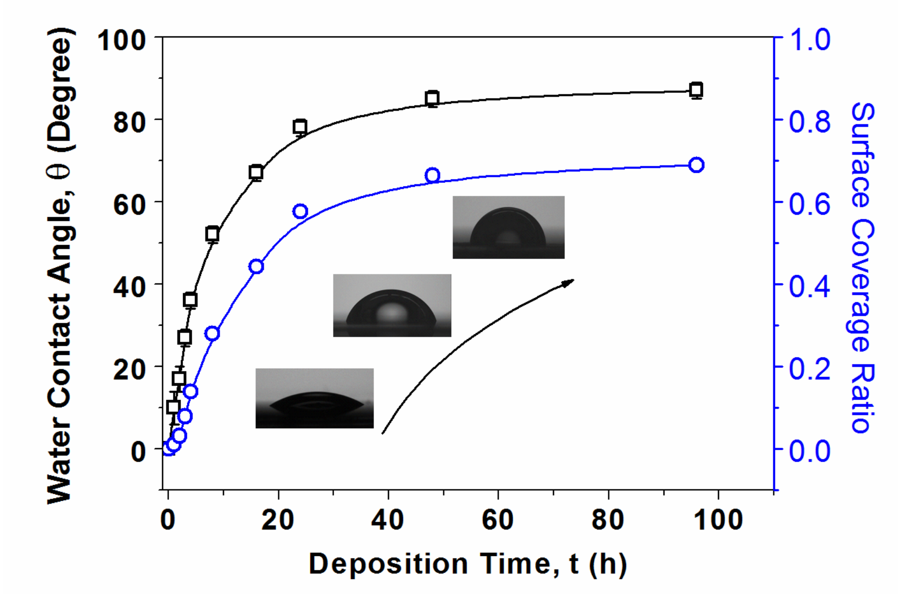

Figure 3.2 Water CA (black squares) on the OTCS-modified mica surfaces and the calculated surface coverage ratio (blue circle) of the OTCS molecules on the mica surface as a function of the OTCS deposition time used to prepare the surfaces. The solid lines are added as the guidance. Insets: water droplet profiles measured on the OTCS-2h, OTCS-8h and OTCS-48h surfaces.

3.3.3 Hydrolysis of The OTCS Aggregates at Acidic Conditions

Previous study suggested that the siloxane bond could undergo hydrolysis under acidic conditions.[29] Herein, the effect of acid on the stability of the as-obtained OTCS aggregates on mica surfaces has been investigated by AFM imaging in aqueous solutions. Figure 3.3 shows the surface morphology and the aggregates height distribution of the OTCS-48h sample measured in 1 mM NaCl aqueous solutions with different concentrations (*i.e.*, 0.001 M, 0.01 M and 0.1 M) of HAc dissolved, the pH of which were 3.8, 3.4 and 2.8, respectively. It can be found that, with decreasing the pH of the incubation solution, the ratio of the aggregates with higher height increased, the lateral size of aggregates also increased from tens of nanometer to hundreds of nanometer. The AFM imaging results in Figure 3.3 indicate that the OTCS aggregates undergo swelling under acidic conditions.

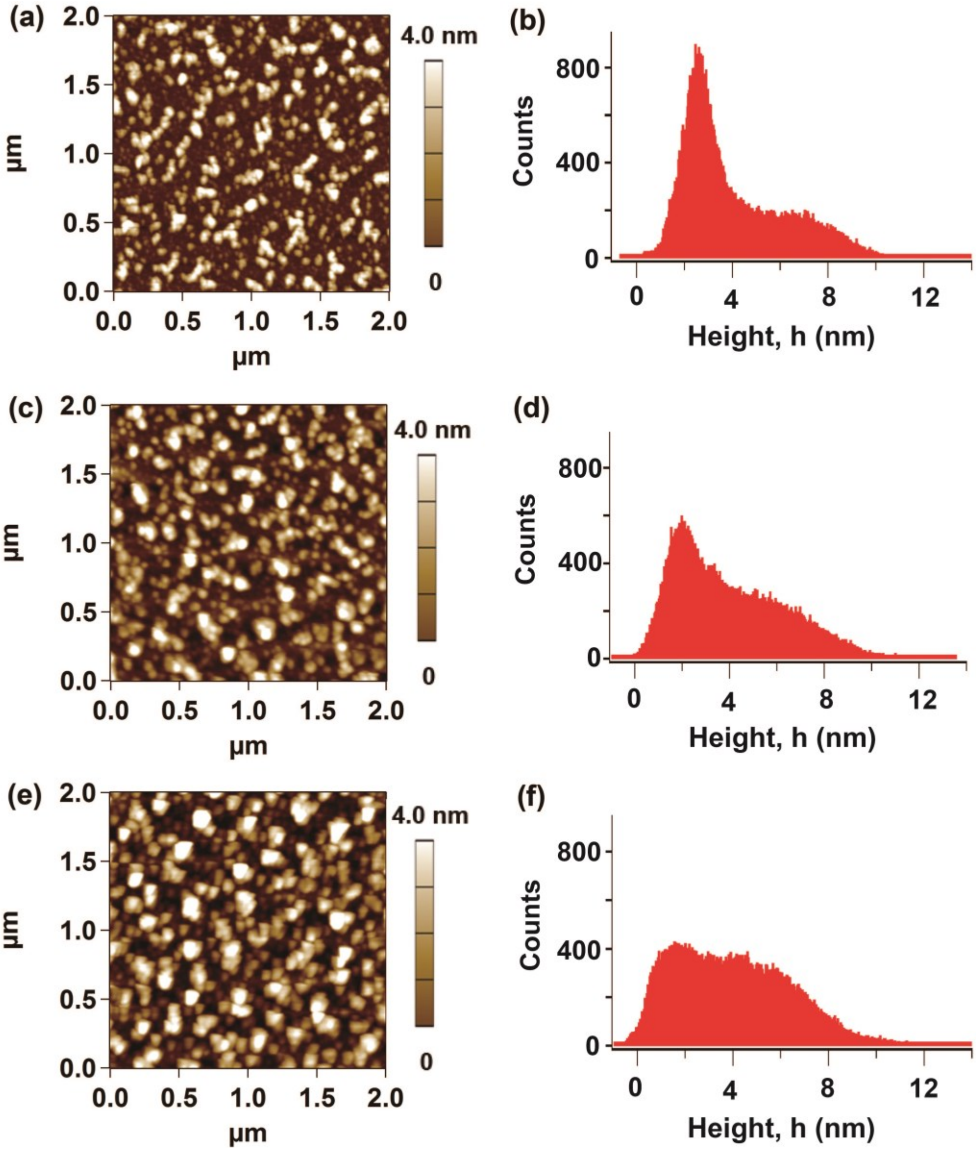

Figure 3.3 (a, c, e) AFM images (left column) of the OTCS-48h sample, measured in 1.0 mM NaCl aqueous solutions with (a) 0.001 M, (c) 0.01 M and (e) 0.1 M HAc, the pH of which were 3.8, 3.4 and 2.8, respectively. The surfaces were imaged ~10 min after immersed in the aqueous solutions. (b, d, f) The corresponding height distributions of the landscape shown in a, c, e.

The stability of the mica-supported OTCS coating was further tested under strong acid (*i.e.*, 0.1 M HCl) with pH of 1.0. After putting ~0.15 ml of 0.1 M HCl solution onto the OTCS-48h surface for two minutes and then rinsing the surface with Milli-Q water, the morphology of the interfacial area (i.e. boundary) between the intact OTCS surface region and the treated region that had been exposed to 0.1 M HCl was imaged by AFM in air. As shown in Figure 3.4a, the OTCS aggregates deposited on the mica surface can be etched away by the acid, leaving a quite flat surface. The cross-section line scan profile that goes across the boundary between the acid treated and untreated regions (Figure 3.4b) further indicates the thickness of the OTCS film of the OTCS-48h sample was ca. 8-10 nm, which is in good agreement with the results shown in Figure 3.1h. Figure 3.4c shows an AFM image of higher resolution for the acid-treated region in Figure 3.4a. It is found that the morphology of this acid-treated region is almost identical to that of the OTCS-2h sample with tiny particles (i.e. tiny OTCS aggregates) deposited on the mica substrate. The instability of the OTCS coatings under strong acid treatment provides a useful way to modify the coating morphology or fabricate patterned OTCS surfaces.

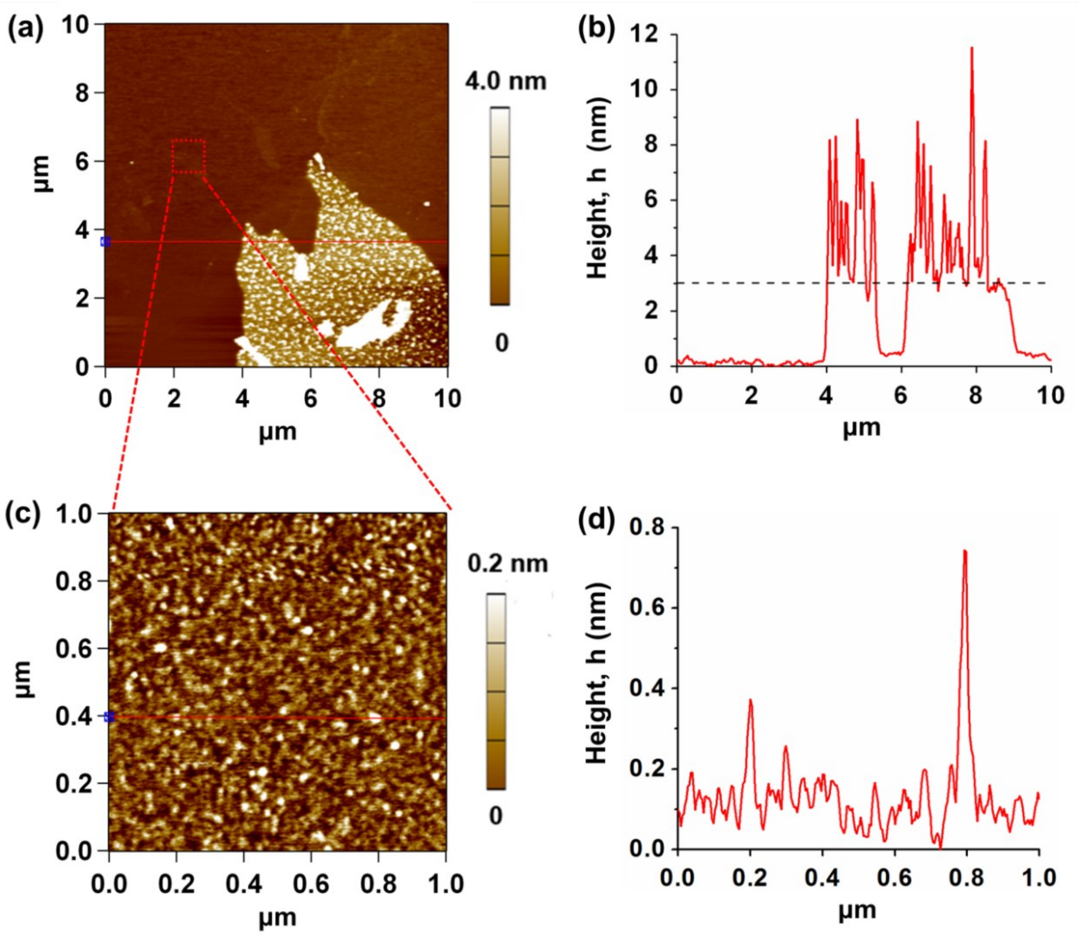

Figure 3.4 (a) The topographic AFM image of the interfacial boundary area between the acid-treated and untreated regions on the OTCS-48 surface. (c) AFM image of higher resolution on the acid treated region in (a). (b) and (d) Cross section line-scan profiles that correspond to the lines shown in (a) and (c), respectively.

The stability of the deposited OTCS coatings was also tested by immersing the OTCS-48h samples in organic solvents (*e.g.*, toluene, heptane) for 48 h, and the AFM images shown in Figure 3.5 did not change much after treating with different organic solvent, indicating that the OTCS coatings obtained by vapor deposition were quite stable in these organic solvents.

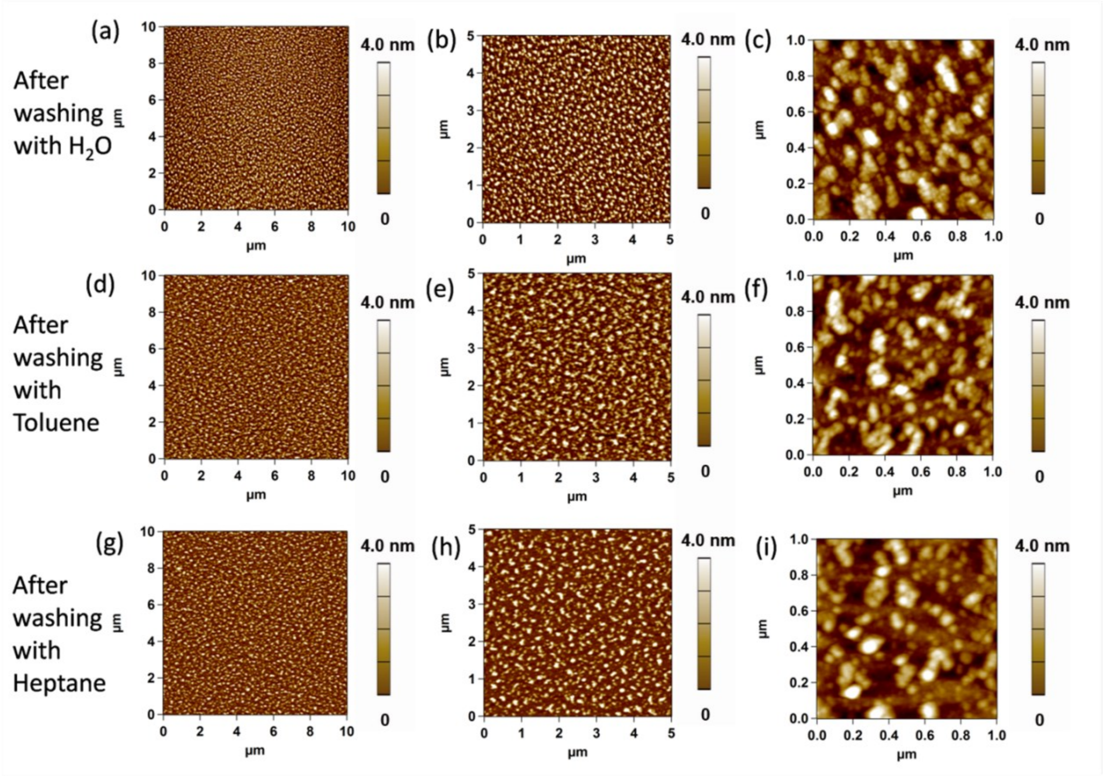

Figure 3.5 AFM images of OTCS-48h surface after immersing and washing with different solvent: H_2O(a-c), toluene(d-f), heptane(g-i).

Based on the results above, the vapor deposition of OTCS molecules on mica could follow a two-stage process illustrated in Figure 3.6. At the initial vapor deposition stage (*e.g.*, < 2 h deposition), the OTCS molecules deposited are firmly attached to the mica substrates *via* strong covalent bond. The silanol groups on the mica surface serve as reactive sites to anchor the deposited OTCS molecules (Stage 1). Meanwhile, the upcoming OTCS molecules at the later vapor deposition stage (*e.g.*, > 8 h deposition) mainly polymerized/nucleated onto the previously deposited OTCS molecules,[148] but relatively loosely attached onto the mica substrates, probably with less or even no covalent bonds (Stage 2). The multilayers could be silanes interconnected through Si-O-Si bond or hydrogen bonding, forming a 3-D alkysiloxane polymerized network. It is noted that the reactions between OTCS molecules on the substrate could occur simultaneously with the deposition process.

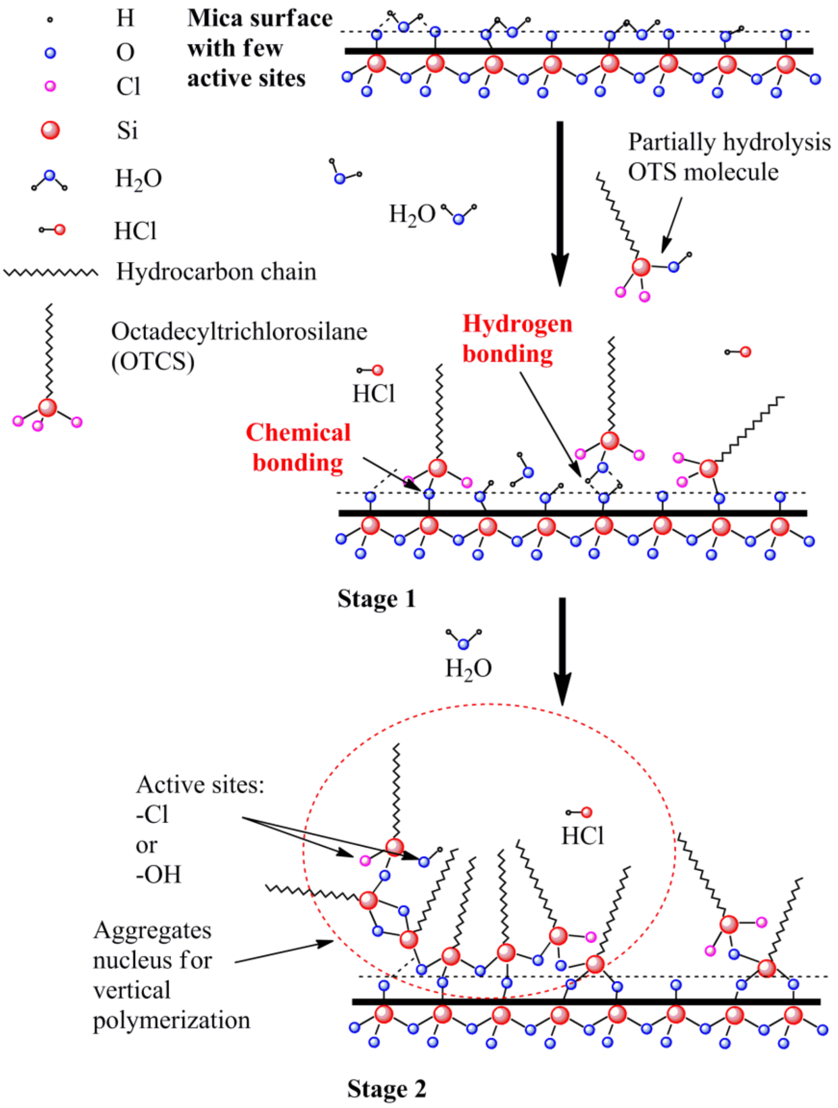

Figure 3.6 Schematic illustration of the deposition process of OTCS molecules onto the freshly cleaved mica surface *via* the vapor deposition method.

3.3.4 Contact Mechanics Study

The study of contact mechanics between solid surfaces can provide useful information on the load-dependent deformation and surface adhesion which are important in many engineering applications.[59] The contact mechanics between the as-prepared OTCS-modified mica surfaces were studied by SFA in air. The two sample surfaces were first brought into contact at zero-load, compressive load was then applied onto the surfaces and was gradually increased till a maximum load $F_\perp$ = 44 mN was reached (i.e., loading process), followed by reducing the load and separation of the two contacted surfaces (i.e., unloading process), both the loading and unloading rate of $dF_\perp/\mathrm{d}t$ was kept at ~0.4 mN/s. The surface deformation was monitored in situ and in real time using the Multiple Beam Interferometry technique. Figure 3.7 shows the plots of the diameter of the contact area between the OTCS-modified mica surfaces as a function of the applied load for a typical loading-unloading cycle. According to the Johnson−Kendall−Roberts (JKR) theory, [106,149, 150] the contact radius between two elastically curved surfaces with increasing the normal load $F_\perp$ can be described by Equation 3.3:

$$r^3 = \frac{R}{K}\left(F_\perp + 3\pi RW + \sqrt{6\pi RF_\perp W + (3\pi RW)^2}\right) \tag{3.3}$$

$$\frac{1}{K} = \frac{3(1-\nu^2)}{2E} \tag{3.4}$$

$$W = 2\gamma \tag{3.5}$$

where r is the contact radius, R is the radius of the surface curvature, K is the equivalent modulus which is related to Young's Modulus E of the surface material by Equation 3.4 (ν is Poisson's ratio), $F_\perp$ is the normal load applied, and W is the adhesion energy between the two contacted surfaces (W=2γ for two surfaces of the same material, Equation 3.5). Accordingly, it is found that the loading curves of the OTCS-2h and OTCS-8h samples can be well fitted by Equation 3.3 with the fitted W

to be 91 mJ/m^2 and 42 mJ/m^2 for the OTCS-2h and OTCS-8h samples, respectively (inset of Figure 3.7). However, the loading curve for the OTCS-48h samples cannot be well fitted by the JKR theory, which could result from the large surface roughness of the samples.

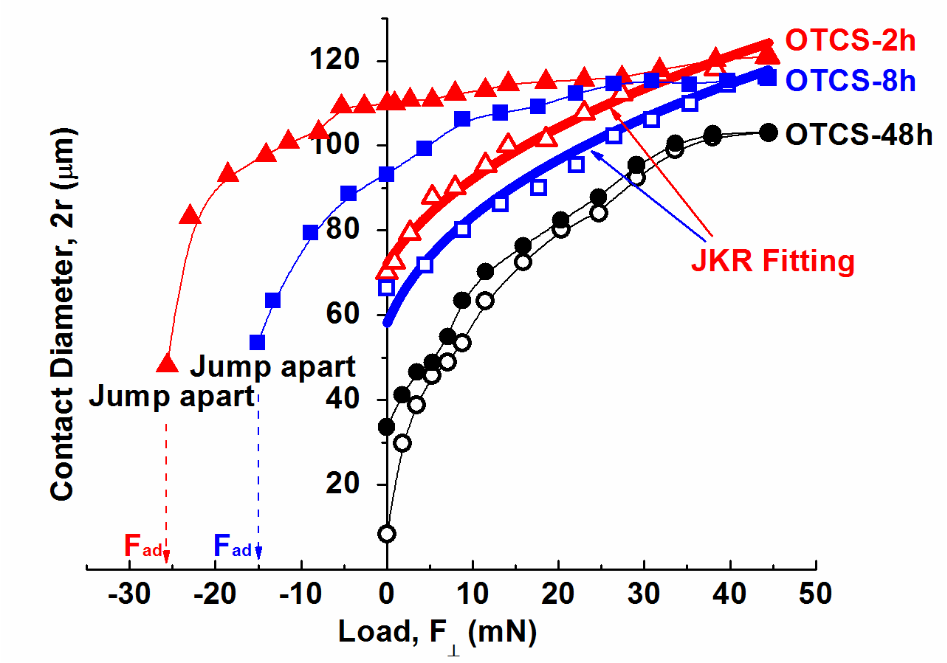

Figure 3.7 The contact diameter *vs.* the applied load in the loading (open symbol) and unloading (filled symbol) processes for typical contact mechanics test between, OTCS-2h (red), OTCS-8h (blue) and OTCS-48 (black) surfaces. The thin solid curves are added for guidance, and the bold red and blue curves are the JKR fitting curves for the OTCS-2h and OTCS-8h cases, respectively.

Figure 3.7 also shows that strong adhesive forces were measured for the OTCS-2h and OTCS-8h surfaces during the unloading process, which decrease from ~25 mN for the OTCS-2h to ~15 mN for OTCS-8h surfaces. In contrast, the adhesive force between the OTCS-48h surfaces becomes almost negligible. Theoretically, the adhesive force F_{ad} between two elastic bodies of the same material (i.e., sphere on a flat surface which is equivalent to the two crossed-cylinder configuration used in SFA), is given Equation 3.6.[151,152]

$$F_{\mathrm{ad}} = 3\pi R\gamma_{\mathrm{R}} \tag{3.6}$$

Accordingly, the effective surface energy γ_{R} can be calculated as

$$\gamma_{\mathrm{R}} = F_{\mathrm{ad}}/3\pi R \tag{3.7}$$

where R is the radius of curvature of the interacting surfaces. The calculated effective surface energies γ_{R} for OTCS-2h, OTCS-8h samples are ~132 mJ/m^2, ~79 mJ/m^2, respectively. The deposition of OTCS-molecules lowers the surface energy of substrate, which is consistent with previous report regarding the effects of organics adsorbed on the adhesion strength of mica surface in air.[153] According to the AFM measurements, the adhesion measured here mainly results from the interactions between the contacted OTCS aggregates and between mica (uncoated region) and the opposing OTCS aggregates. The increase of surface roughness could decrease the effective contact area between the surfaces and thus dramatically decreases the adhesion, which is consistent with previous reports on adhesion between rough surfaces.[59,154]

The loading and unloading curves of all the measured samples in Figure 3.7 do not overlap, showing adhesion hysteresis. The adhesion hysteresis generally describes the phenomenon that taking apart two surfaces in contact dissipates more energy than bringing the surfaces together.[24,143,155,156] Plastic deformations,[157] interdigitation/interpenetration of the surface functional groups or polymer chain ends,[24,158] polar interaction,[153] dynamic rearrangement and disentanglement of the polymer segments at contact interfaces[156] are thought to be the possible causes of adhesion hysteresis. Adhesion hysteresis is generally described by

$$\Delta\gamma = \gamma_R - \gamma_A \tag{3.8}$$

where γ_A is the advancing surface energy measured on loading process (that is generally close to the equilibrium thermodynamic surface energy of the material) as described using Equation 3.3, and γ_R is the effective (receding) surface energy measured during the unloading process (Equation 3.7).[152, 155] Accordingly, the calculated energy hysteresis $\Delta\gamma$ for the OTCS-2h and OTCS-8h samples are ~87 mJ/m^2 and ~58 mJ/m^2, respectively. Therefore, the OTCS-8h surface shows lower adhesion hysteresis during a loading-unloading process as compared to the OTCS-2h surface, with higher amount of OTCS deposited. It is noted that for OTCS-48h surfaces with longer vapor-deposition time (48h), the loading process could not be well described by the JKR theory due to the relatively high surface roughness[59,154] and the presence of large OTCS aggregates deposited (as shown in Figure 3.1d and 3.1h). Overall, the contact mechanics test on the OTCS-modified mica surfaces using SFA is in good agreement with the AFM imaging measurements, showing that OTCS coatings deposited on mica could significantly reduce the surface adhesion and adhesion hysteresis.

3.3.5 Interactions between OTCS-modified Mica Surfaces in NaCl Solutions

The interactions between two OTCS-modified mica surfaces in aqueous NaCl solutions were also measured using SFA. Figure 3.8a and Figure 3.8b show the force-distance profiles on approach and separation, respectively, for two OTCS-modified mica surfaces, obtained *via* different vapor deposition times (*i.e.*, 2 h, 8 h, and 48 h), in 1 mM NaCl solution at pH 6.0. The OTCS layer thickness deposited on mica could be determined as half of the confined separation distance (or so-called hard-wall distance) when the two surfaces were brought into contact under relatively high load. Note that the zero separation distance (D=0) here was defined as the mica-mica contact in air. The OTCS layer thicknesses of the OTCS-2h, OTCS-8h and OTCS-48h samples could be determined to be ~1.1 nm, ~2.8 nm and ~9.8 nm, respectively, in good agreement with the height of the OTCS nano-aggregates as imaged by AFM.

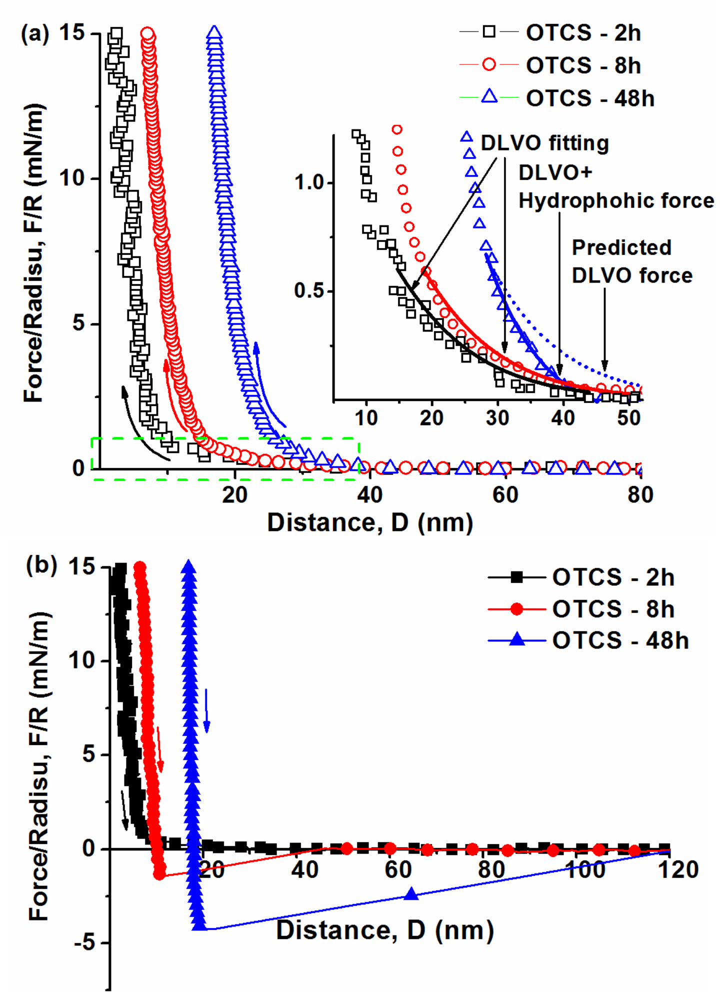

Figure 3.8 (a, b) Interaction force curves measured during approaching (a) and separating (b) for two OTCS-2h (black square), OTCS-8h (red circle) and OTCS-48h (blue triangle) surfaces in 1 mM NaCl solution at pH 6.0. Inset of (a): DLVO fitting curves for the OTCS-2h (black solid curve) and OTCS-8h (red solid curve) samples, and modified DLVO fitting curve by considering the hydrophobic interaction (blue solid curve) (as compared to the prediction by DLVO model, blue dash curve) for the OTCS-48h sample. Note that in the theoretical calculations, the planes of origin for all DLVO contributions (and hydrophobic interactions) have been shifted to the hard-wall contact by subtracting the thickness of respective coating layers: (D-2T) was used in Equations 3.10 and 3.11.

The interactions measured between two OTCS-modified mica surfaces during approaching could be attributed to the sum of several kind of interactions (Equation 3.9), namely the DLVO interaction (F_{DLVO}) which includes attractive van der Waals forces and repulsive electrical double layer forces due to the charged OTCS or mica surfaces, the attractive hydrophobic interaction ($F_{\mathrm{Hydrophobic}}$) due to the presence of hydrophobic domains, and the repulsive steric interaction (F_{Asperity}) due to the presence of contacted surface asperities.

$$\frac{F(D)}{R}=\frac{F_{DLVO}}{R}+\frac{F_{Hydrophobic}}{R}+\frac{F_{Asperities}}{R} \tag{3.9}$$

No attraction was measured during the approaching of two OTCS-modified mica surfaces (Figure 3.8a), which indicates that the repulsive interactions between the OTCS-modified mica surfaces dominate the surface interactions. For OTCS-2h and OTCS-8h samples, the modified mica surfaces had relatively low coverage of OTCS molecules (<30 %), and the surface roughness was also relatively small (< 1 nm, Figure 3.1b, 3.1f), suggesting the hydrophobic interaction and steric interaction in Equation 3.9 might not play important roles in their surface interaction, especially at relatively large separation distances or low load regime. The overall DLVO force $F_{DLVO}(D)$ between two OTCS-2h, OTCS-8h surfaces is described by Equation 3.10, where R is the surface curvature, A_{mwm} is the Hamaker constant for mica-water-mica with a value of 2×10^{-20} J,[1] D is the distance between the two mica surfaces, T is the OTCS film thickness (*e.g.*, 1.1 nm for the OTCS-2h sample measured using SFA), ε is relative permittivity of aqueous medium, ε_0 is vacuum permittivity, κ is the reciprocal of Debye length with a value of 1.03×10^{8} m^{-1} for 1 mM NaCl solution, ψ is the surface potential. For OTCS-2h and OTCS-8h samples, ψ is fitted to be -35 mV and -20 mV respectively. The surface potential of mica was reported to be about -60 mV under similar solution conditions,[159] and the surface potential of a fully covered alkysilane coating was reported to be -15 mV to -30 mV.[160, 161] The fitted surface potential values for OTCS-2h and OTCS-8h fall into the surface potential range of bare mica and fully covered alkysilane surfaces, which is mainly due to the scattered alkysilane coating on mica here.

$$\frac{F_{DLVO}(D)}{R}=-\frac{1}{6}\frac{A_{mwm}}{(D-2T)^2}+4\pi\varepsilon\varepsilon_0\kappa\times\psi^2\left[\frac{e^{-\kappa(D-T)}-e^{-2\kappa(D-T)}}{1-e^{-2\kappa(D-T)}}\right] \quad (3.10)$$

In contrast, the classical DLVO model was not able to well fit the force-distance profile of the OTCS-48h at low load using Equation 3.9 with ψ ~ -20 mV. As compared to the predicted DLVO forces (blue dash line in the inset of Figure 3.8a), the lower measured forces (at relatively low load or large separation regime) could be most likely due to the hydrophobic attraction between the hydrophobic OTCS-48h surfaces. The hydrophobic interaction ($F_{\mathrm{Hydrophobic}}$) has been reported to follow an exponential equation as shown in Equation 3.10, C is a pre-exponential parameter and D_0 is the characteristic decay length of hydrophobic interaction. When incorporating the effect of hydrophobic interaction into the modified DLVO fitting (Equation 3.11, where A_{owo} is the Hamaker constant for OTCS-water-OTCS with a value of 8×10^{-21}J), reasonable fitting could be achieved (blue solid curve in the inset of Figure 3.8a). It should be noted that the fitted characteristic decay length of hydrophobic interaction

D_0 is ~13 nm here, which is close to the reported value (~10 nm) previously measured between two OTCS-modified glass surfaces (with a water contact angle of 92°), but is higher than the values (< 5 nm) reported between two polydimethylsiloxane grafted mica surfaces or between bubble and smooth OTCS-modified mica surfaces. Strictly speaking, the classical DLVO model or the modified DLVO model (by including the hydrophobic interaction) should be only applicable to smooth surfaces.However, the OTCS-48h surfaces prepared in this work were considerably rough with surface heterogeneity containing both hydrophobic and hydrophilic domains (Figure 3.1 and Figure 3.2), therefore, contributing to the above difference in the decay length of hydrophobic interactions. At relatively high load (or short separation) regime, the increased repulsion could be mainly due to the steric interaction between the contacted asperities of the two OTCS-48h surfaces. Nevertheless, the above analysis indicates hydrophobic and steric interactions play an important role in the surface interactions of OTCS-48h surface in aqueous solution.

$$\frac{F_{Hydrophobic}}{R} = -Ce^{-(D-2T)/D_0} \tag{3.11}$$

$$\begin{aligned}\frac{F(D)}{R} &= \frac{F_{DLVO}}{R} + \frac{F_{Hydrophobic}}{R} \\ &= -\frac{1}{6}\frac{A_{owo}}{(D-2T)^2} + 4\pi\varepsilon\varepsilon_0\kappa\times\psi^2\left[\frac{e^{-\kappa(D-2T)} - e^{-2\kappa(D-2T)}}{1-e^{-2\kappa(D-2T)}}\right] - Ce^{-(D-2T)/D_0}\end{aligned} \tag{3.12}$$

When the two OTCS-modified surfaces were separated, adhesion and jump-out behavior were observed for the OTCS-8h and OTCS-48h surfaces, while only pure repulsion was observed for the OTCS-2h sample (Figure 3.8b). The adhesion measured was mainly due to the vdW interactions between the two contacted surfaces and interpenetration of the OTCS molecules at the contact interface. Higher adhesion was measured between OTCS-48 surfaces than that of OTCS-8h surfaces, which could be attributed to (1) higher OTCS surface coverage (with high probability for interpenetration of OTCS molecules at the contact interface surface) and (2) higher surface hydrophobicity allowing a more intimate contact of the contacted hydrophobic OTCS asperities in aqueous medium. [24, 145] It is noted that the adhesion measured between the as-obtained OTCS-mica surfaces (e.g. OTCS-48h) in this work is much smaller than those measured between flat hydrophobic surfaces (e.g. >200 mN/m between two flat polystyrene surfaces) reported previously,[8] which could be due to the fact that the effective contact area between the rough surfaces was much smaller than that between flat surfaces.

Effect of preload on the adhesion

The above AFM imaging and force analysis indicate that the surface asperities could play an important role in the interactions between OTCS-mica surfaces in aqueous solution, particularly for the cases with relatively high surface roughness (e.g., OTCS-48h). Therefore the effect of the maximum preload applied during force measurements on the adhesion of the OTCS-48h surfaces was investigated. As shown in Figure 3.9, as the maximum preload applied changed from 15, 42 to 105 mN/m, the adhesion increased from 3.9, 6.2 to 8.6 mN/m. The results in Figure 3.9 are consistent with previous reports that the measured adhesion could increase with applied preload for rough surfaces as their real contact area would increase with increasing with applied load. [24,59] When the two rough OTCS surfaces come into contact, the peaks of the asperities first got into contact, and these contacted asperities could undergo deformation readily while the uncoated asperities did not deform.[162] With increasing the applied load, the real contact area of two rough surfaces would increase due to the enhanced deformation of the previously contacted asperities as well as the increased number of asperities getting into contact.[163] The increased real contact area and increased load could strengthen the interpenetration of the OTCS chains at the contact interface. Therefore, the adhesion was strengthened with increasing the load applied for rough OTCS surfaces.

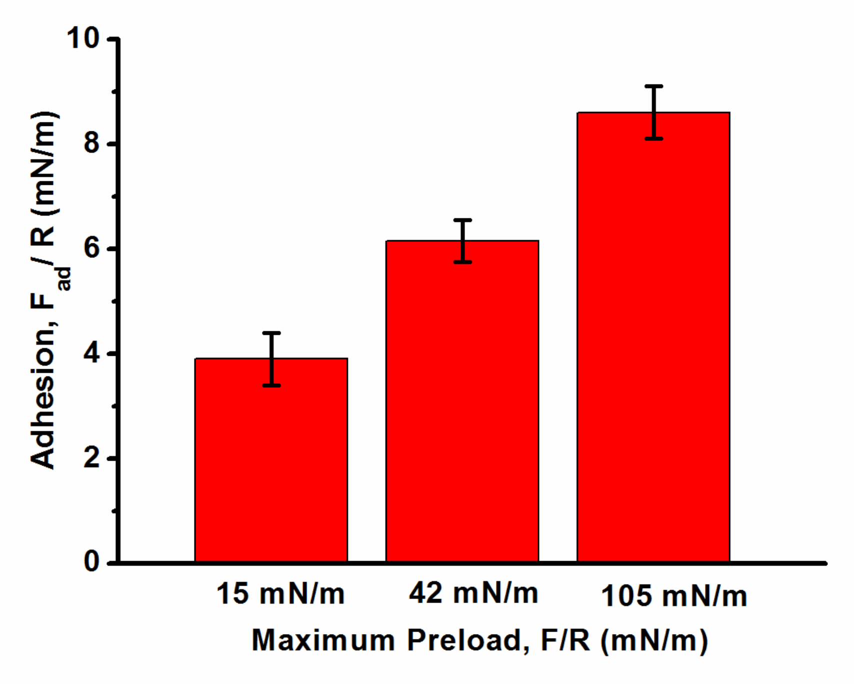

Figure 3.9 Adhesion measured during separating two OTCS-48h surfaces with different preload (i.e., 15, 42 and 105 mN/m).

Effect of solution pH on the adhesion

The AFM imaging results on the OTCS-modified mica surfaces indicated that the OTCS aggregates on the OTCS-48h surface could be hydrolyzed at low pH. Herein the effect of pH on the interactions between two OTCS-48h surfaces in 1 mM NaCl solutions of different pH conditions was investigated. As shown in Figure 3.10, OTCS-48h surfaces exhibit similar force profiles when measured in solutions of pH 10 and pH 6. The confined film thickness did not change at pH 10 as compared to that at pH 6 (even after immersing for 60 min). In contrast, when the interactions were measured in aqueous solution of pH 2, the confined film thickness decreased to ~4 nm (under the same immersing time), indicating that the OTCS films was partially dissolved under the low pH conditions. Only pure repulsion was measured during approaching for all the three pH conditions, which was mainly attributed to the electrical double layer repulsion and steric repulsion, overcoming the hydrophobic attraction and vdW interaction between the two surfaces under the solution conditions investigated. [145,164,165] For pH 2, the deposited OTCS aggregates was mostly dissolved, the confined film thickness decreased from ~20 nm to ~4 nm. The reduced repulsion and absence of adhesion during separation at pH 2 could be mainly due to the dissolving of OTCS layer and the decreasing of surface hydrophobicity (note the water contact angle of the surfaces decreased to ~ 28^{o} after being immersed in the solution of pH 2 for 60 mins).

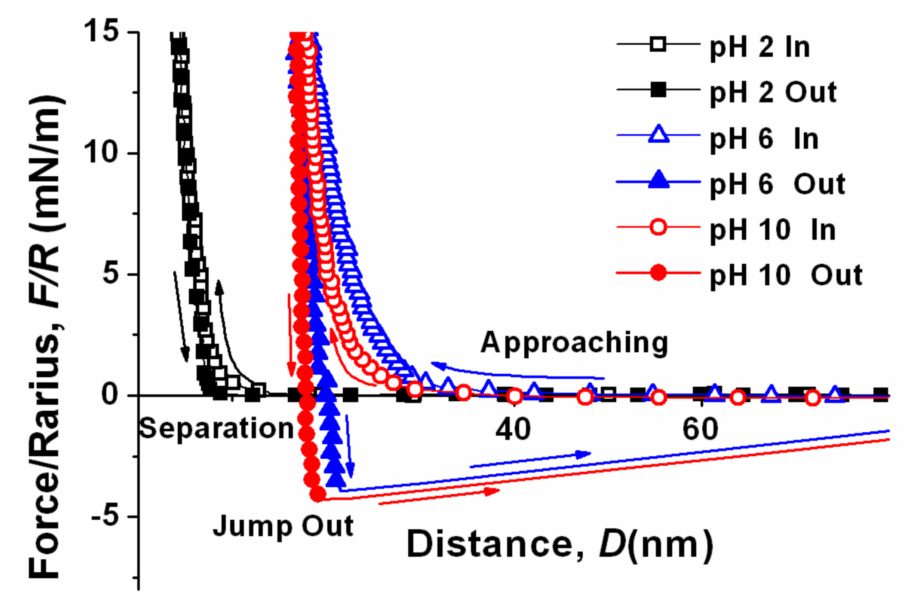

Figure 3.10 Interaction force profiles measured during approaching (open symbols) and separating (filled symbols) of two OTCS-48h surfaces in 1 mM NaCl aqueous solutions with pH of 2 (black), 6 (blue) and 10 (red).

3.4 Conclusions

This work has systematically investigated the deposition behaviors of a model alkylsilane (i.e., OTCS) on freshly cleaved mica with low density of reactive sites *via* a facile vapor deposition method. Coatings with multilayered OTCS nanoaggregates were obtained, which were different from the ordered SAM OTCS films deposited on substrates with relatively high coverage of reactive sites reported previously.[137-139] The AFM imaging results indicate that the vapor deposition mainly follows a two-stage process: (1) OTCS molecules first firmly attach to the mica substrates and form scattered nanoaggregates, which serve as nucleation sites for the further deposition of OTCS molecules; (2) the OTCS nanoaggregates continue to grow with time and form multilayered OTCS aggregates, relatively loosely attached on the mica substrates. The as-obtained OTCS films can undergo hydrolysis in strongly acidic conditions (pH $\leqslant$ 2), providing a useful approach for fabricating controlled OTCS nanostructures. The OTCS films show excellent stability in common organic solvents (e.g., toluene, heptane).

The interactions between the as-obtained OTCS surfaces were quantitatively measured in air and aqueous solutions using an SFA. The contact mechanics tests in air demonstrate that the OTCS coatings can significantly reduce the surface adhesion and adhesion hysteresis. The surface forces of the OTCS samples obtained at relatively short deposition time (e.g., OTCS-2h and OTCS-8h) in aqueous solutions can be reasonably described by the classical DLVO theory. However, for the samples obtained with longer deposition times (i.e., OTCS-48h), additional hydrophobic interaction and steric interaction play an important role due to their enhanced surface hydrophobicity and surface roughness. Our results provide useful insights into the physicochemical characteristics of alkylsilane deposition on substrates via vapor deposition method and the fundamental interaction mechanisms of the alkylsilane surfaces, with implications in many related engineering applications.

CHAPTER 4

END-GRAFTED HYDROPHOBIC POLY(PENTAFLUOROPHENYLACRYLATE)-*b*-POLYSTYRENE SURFACES: PREPARATION, CHARACTERIZATION AND RELATED SURFACE INTERACTIONS IN AQUEOUS SOLUTIONS

4.1. Introduction

Physical adsorption and chemical bonding are two typical methods for preparing polymer coatings which have been extensively exploited for creating multi-functional surfaces..[166] Compared with physically adsorbed polymer surface, the chemical bonded surface has more practical value in terms of its applicability to sustain strong mechanic shearing or pressing under harsh environment. Two methods are commonly used to prepare chemical bonded polymer coatings, one is the "graft from" method, which involves polymerization initiated at the substrate surface through attached initiating groups.[167] Polymer films with the thickness of hundreds of nanometers can be achieved by using "graft from" method.[168,169] However, due to the low amount of grafted polymer on surfaces, it is quite challenging to characterize the authentic properties such as polydispersity and molecular weight of the grafted polymer films. The other method termed as "graft to" involves reaction of end-functionalized polymer molecules with complementary functional groups forming tethered chains on the surfaces.[167] Therefore, the “graft to” method tends to be technically less challenging in terms of both polymer design and synthesis. In addition, the polymers can be thoroughly characterized via various chemical and physical methods because the polymer synthesis step and function process are proceeded separately.[170] The major limitation of the ‘‘grafting to’’ method is that it typically yields polymer films with a thickness ranging from five to tens of nanometers with relatively low graft density.[167]

Silane-incorporated polymer reagents that can react with hydroxyl rich inorganic substrates forming covalent silicon-oxygen bond, provide basis for preparing truly covalently bonded polymer layers using “graft to” method.[2] However, there are some drawbacks of using silane-polymer reagents, such as aggregation, contamination due to environmental conditions, solvent impurity or strict anhydrous conditions being used during the grafting process. Poly(pentafluorophenyl acrylate) (PPFPA) is an active polymeric esters that reacts with aliphatic amines and aromatic amines under mild conditions with short reaction time generating polymerical materials that were soluble in most organic solvents.[171] This reagent provides an alternative way for preparing grafted polymeric materials onto amine functionalized surfaces. Compared with silane-polymer reagents, the PPFPA active-esters are more stable when stored in ambient conditions and the reaction between active ester and amine takes place in a more mild way, which can reduce the chance of aggregation during grafting and obtain relatively smooth polymer coatings. More importantly, the interfacial layers that contain un-reacted pentafluorophenyl groups can facilitate further post-polymerization modification, thus extends the application of multi-functional polymer surfaces.[170]

Polymer grafted surfaces with controlled hydrophobicity have a wide range of engineering and biomedical applications because surface hydrophobicity can significantly affect water structure, [11,172,] the behavior of ions,[52, 53] the formation and stability of bubbles on or near polymer surfaces.[11, 35,173] Previous studies revealed that micro- and nano-bubbles could exist on physically adsorbed hydrophobic polystyrene surface, and significantly influence the surface interactions between polymer coated mica surfaces.[8, 174, 175] However, physically adsorbed polymer films would suffer from fracture or dewetting in aqueous solutions during force measurement. Moreover, surface bubbles together with ions have been reported to significantly alter the surface topography when immersed in aqueous solutions.[33, 42] All those factors add up the difficulty of fully understanding the force interactions between two polymer surfaces, thus it is necessary to develop stable, chemically grafted surfaces with varied hydrophobicty for systematically studying the surface interactions. To the best of our knowledge, there is few report in the aspect to systematically elucidate the preparation of hydrophobic adjustable, end-grafted block *co*-polymer surfaces on atomic smooth mica surface and systematically study the surface interactions in air and in aqueous solutions.

In this work, smooth poly(pentafluorophenyl acrylate)-*block*-polystyrene (PPFPA-*b*-PS) films covalently end-attached onto amino groups functionalized mica surface were obtained using a “graft to” technique for the first time. The grafting of the PPFPA-*b*-PS polymer was achieved *via* forming amido bonds between amino groups and pentafluorophenyl groups. The hydrophobicity of grafted mica surface could be modulated by adjusting the deposition time of the precursor layer (3-Aminopropyl) triethoxysilane (APTES). The interactions between end-grafted polymer surfaces were quantitatively measured using a surface forces apparatus (SFA) in air and in aqueous solutions. Various factors, including hydrophobicity, salt concentration and degassing have been investigated. It is observed that the end-grafted polymer surface shows better stability than physically adsorbed polymer surface during force measurement. Surface hydrophobicity and salt could greatly influence the interaction between two surface: for low hydrophobicity surface (water contact angle CA ~ 60^{o}), classic DLVO force dominate the approaching process, however for high hydrophobicity surface (CA ~ 90^{o}), long range attraction (~20-100 nm) is observed. Importantly, it is observed that degassing of solution will also lead to shortened range of attraction for higher hydrophobicity surface during approaching, which confirms the important role of dissolved gas on two end-grafted hydrophobic polymers in aqueous media. Our research provides new insights into the basic interaction mechanism between chemical grafted hydrophobic surfaces, with implications for many biological and non-biological phenomena such as mineral flotation, protein adsorption and self-assembly.

4.2 Experiment Section

4.2.1 Materials and Surface Preparation

(3-Aminopropyl) triethoxysilane (APTES, 98%) was purchased from Alfa-Aesar, Azobisisobutyronitrile (AIBN), pentafluorophenyl (PFP), acryloyl chloride, styrene, anisole, dioxane were purchased from Sigma-Aldrich. Ruby mica sheets were purchased from S & J Trading Inc. (GlenOaks, NY). Milli-Q water with a resistance of ≥18.2 MΩ·cm was used for preparing aqueous solutions. AIBN was purified by recrystallized twice from ethanol. Styrene was passed through a short column of basic aluminum oxide to remove inhibitor. PFPA and Reversible Addition-Fragmentation Chain Transfer (RAFT) agent, 2-(dodecylthiocarbonothioylthio)-2-methylpropionic acid (DDMAT), were synthesis according to the procedures reported in references.[171,176]

Figure 4.1 shows the schematic synthesis route of poly(pentafluorophenyl acrylate)-*block*-polystyrene (PPFPA-*b*-PS) polymer and the reaction between amines and pentafluorophenyl esters. The functional block copolymer, PPFPA-*b*-PS, was prepared by RAFT polymerization using a PFPA based macro-RAFT agent. Here is the typical reaction for preparing this macro-RAFT agent: a 50 mL one-port round-bottom flask was charged with PFPA (2.38 g, 0.01 mol), AIBN (0.0081 g, 0.5 mmol), DDMAT (0.09125 g, 2.5 mmol) and dioxane (5 mL). The whole mixture was purged with argon for 30 min to remove oxygen and sealed under argon atmosphere. Then it was put in a preheated oil bath at 80 ^{o}C and allowed to process the polymerization for 2 hr. The polymerization was quenched by cooling the flask in liquid nitrogen. The mixture was diluted with dichloromethane and the polymer was precipitated into methanol. The above purification was repeated three times and the product was collected and dried in vacuum to constant weight, yielding 2.10 g (conversion: 88%) of solid product as PPFPA$_{-30}$. $M_{n,NMR}$ = 7140 kg/mol;. $M_{n,GPC}$ = 8,000 kg/mol, M_w/M_n = 1.10.

The block copolymer, PPFPA-*b*-PS, was obtained by using the above macro-RAFT agent as the starting block. The typical example is shown as follows: PPFPA$_{30}$ (0.325 g, 0.05 mmol), styrene (5.2 g, 0.05 mol), AIBN (1.6 mg, 0.01 mmol) were added into a round-bottom flask. The whole mixture was applied with three freeze-pump-thaw cycles and then kept the flask to let it react at 75 ^{o}C for 24 h. The resulting solution was diluted with chloroform and precipitated into methanol three times. The product was collected and dried at 40 ^{o}C under vacuum for 24 h, yielding 4.5 g of white solid product. $M_{n,NMR}$ = 97140 kg/mol;. $M_{n,GPC}$ = 100,000 kg/mol, M_w/M_n = 1.10. Then the synthesized PPFPA-*b*-PS block polymer is dissolved in toluene with a concentration of ~0.5 wt % for surface coating.

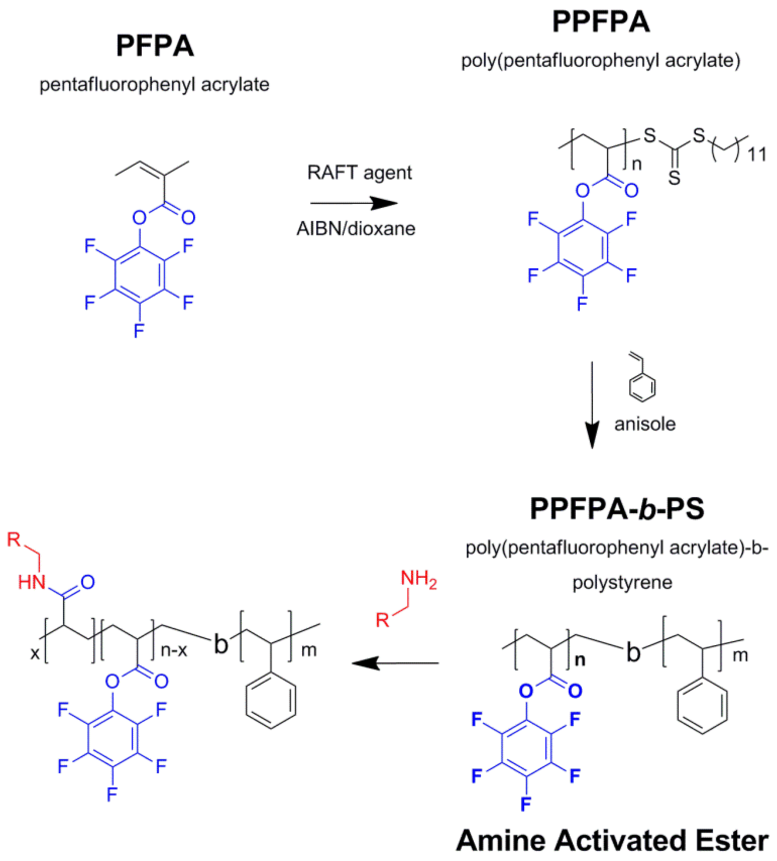

Figure 4.1 Schematic illustration of synthesizing poly(pentafluorophenyl acrylate)-*block*-polystyrene (PPFPA-*b*-PS) polymer and the chemical reaction between active ester and amino derivatives.

Figure 4.2 shows the schematic process for grafting PPFPA-*b*-PS polymer onto APTES treated mica surface. Firstly, fresh cleaved mica surface were placed inside a plasma chamber (40W, Harrick Plasma,) for 10 min under continued N_2 and water vapor flow to generate enough active sites (*i.e.*, hydroxyl groups) on mica surfaces. Then the treated mica surfaces were placed in a plastic petri-dish (9 cm diameter, Fisher Scientific) inside a plastic vacuum desiccator (230 mm Diameter, Bel-Art Scienceware). Then 100 µl of 98% APTES liquid were added into the desiccator using a small PTFE cap as reservoir, and the system was kept under vacuum (ca. 1300 Pa) for different deposition time as reported previously.[177, 178] Then the APTES source was removed, and those APTES treated mica surfaces were kept under vacuum for another 24 h and vacuum annealed at 80 °C for another 2 h.. Later the APTES pre-treateded mica surfaces were spin coated with 5 drops of PPFPA-*b*-PS toluene solution (0.5%) and annealed in vacuum at 80 °C for another 24 h. Finally the surfaces are washed with toluene to remove un-reacted polymer species and kept under vacuum for at least 24 h to remove possible solvent residual in the polymer network. Degassing of the aqueous solutions was carried out following the same method reported by Faghihnejad and Meyer *et al.*[8, 11] by using an oil-free vacuum pump connected to either a filtering flask or SFA chamber directly under a pressure of 1300 Pa for 20 min.

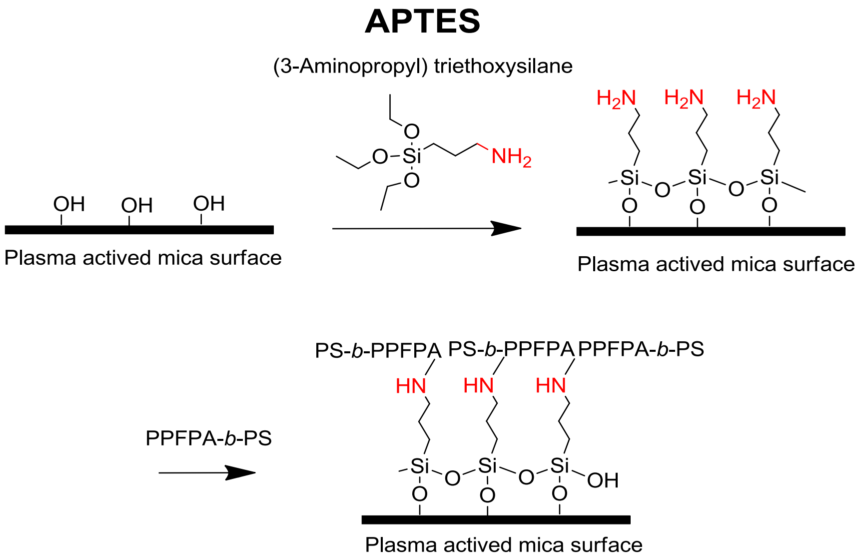

Figure 4.2 Schematic illustration of the grafting process of PPFPA-*b*-PS onto water-plasma treated mica surfaces.

4.2.2 Surface Characterizations

The morphology of the APTES and PPFPA-*b*-PS grafted mica surfaces was characterized with an Atomic Force Microscope (MFP-3D, Asylum Research, Santa Barbara, USA) under the Acoustic tapping mode. Silicon cantilevers (Bruker Nano), with a nominal resonance frequency of 300−400 kHz and spring constant of ~ 40 N/m were used for imaging. Surface hydrophobicity of the obtained polymer grafted surface was assessed by water contact angle (CA, Rame–Hart drop shape analysis system, USA) measurements in the laboratory atmosphere. The chemical composition of APTES treated mica and end grafted polymer-mica surface (2 cm × 2 cm) was determined by using X-ray photoelectron spectroscopy (XPS, Kratos Axis Ultra Spectrometer, USA) employing a monochromator Al Ka X-ray source, hv = 1486.71 eV, under high vacuum (~5 $\times 10^{-10}$ Torr). Charge effects were corrected by using C 1s peak at 284.8 eV as a reference. Nonlinear optimization was used to determine the peak model parameters such as peak positions, widths, and peak intensities by using the Marquardt algorithm (Casa XPS). A Shirley background was applied to subtract the inelastic background of core-level peaks.

An SFA 2000 (SurForce LLC, Santa Barbara, CA, USA) was used to measure the contact mechanics and interaction forces between end-grafted PPFPA-*b*-PS films. The SFA technique has been extensively used to study the interactions in biological and un-biological systems for decades. It allows accurate and direct determination of forces between two surfaces as a function of separation distance with force sensitivity down to 10 nN and the distance resolution down to 0.1 nm. Detailed setup of the SFA system and working principles can be found elsewhere.[93,102] Briefly, two back silvered mica surface with the thickness of 1-5 μm were glued onto cylindrical silica disks with the curvature radius of 2 cm. Then the glued mica surface were treated with APTES first and then grafted with PPFPA-*b*-PS, as described in previous sections. After that, the two disks were mounted into the SFA chamber in a cross-cylinder configuration. The film thickness and absolute separation distance could be obtained in situ by employing an optical technique named Multiple Beam Interference (MBI) with fringe of equal chromatic order (FECO).[93] For contact mechanics test in air, the two surfaces were first brought into adhesive contact by electric-motor, and then a finite compressive load was applied using a differential micrometer with the loading and unloading rate being kept at ~0.4 mN/s. The contact diameter was monitored through FECO fringes change in real time. For surface force measurements, ~100 uL of desired aqueous solution was injected between the two disks. According to Derjaguin approximation,[1] when the separation distance is much smaller than the radius of the curvature, it is equal to a sphere with the radius of R approaching a flat surface, the measured force, F, can be converted into energy per unit area (W(D)) follow Equation 4.1.

$$F(\mathrm{D})=2\pi R W(\mathrm{D}) \tag{4.1}$$

In this study, the contact mechanics tests were carried out under room temperature with a small container filled with P_2O_5 in the sealed SFA chamber to ensure the dry atmosphere condition. SFA was also applied to measure the interaction forces of end grafted polymer surface in NaCl aqueous solutions of different concentrations (1 mM and 100 mM). The effect of degassing was also conducted by using an oil free mechanic pump.

4.3. Results and Discussion

4.3.1 Surface Hydrophobicity of APTES and PPFPA-*b*-PS Grafted Mica Surfaces

To verify the successfully grafting of APTES and PPFPA-*b*-PS on mica surface, the hydrophobicity of (3-Aminopropyl) triethoxysilane (APTES) treated mica and PPFPA-*b*-PS grafted polymer surface were accessed by water contact angle (CA) measurement. Figure 4.3 shows the CA of APTES modified mica (red line) and PPFPA-*b*-PS modified APTES-mica surface (black line) as a function of APTES deposition time. Accordingly, the water CA of bare APTES surface on mica gradually increases from 0^o to ca 40^o when APTES deposition time varies from 0 h to 14 h. However, the water CA of end grafted PPFPA-*b*-PS surface quickly reaches ca. 90^o when the deposition time of APTES is longer than 8 h. Three regions can be roughly identified from the CA evolution curve of grafted PPFPA-*b*-PS: (i) the rapidly increasing region from 0^o to 60^o with the APTES deposition time increasing from 0 h to 2 h, (ii) the slowly increasing region ranging from 60^o to 90^o with the APTES deposition time increasing from 2 h to 8 h, (iii) the plateau region around 90^o when the APTES deposition time is longer than 8 h. The low hydrophobicity of APTES surface (< 40^o) could due to the polar amino groups of APTES molecules. It is reported that a bare mica surface exhibits superhydrophilicity with water contact angle (CA) of ca. 0^o, [141] while a polystyrene surface generally shows hydrophobic property with a higher CA of ca. 91°.[42,179] The gradually change of water CA after grafting polymer provides indirect evidence of successfully grafting PPFPA-*b*-PS polymer onto APTES treated mica surface.

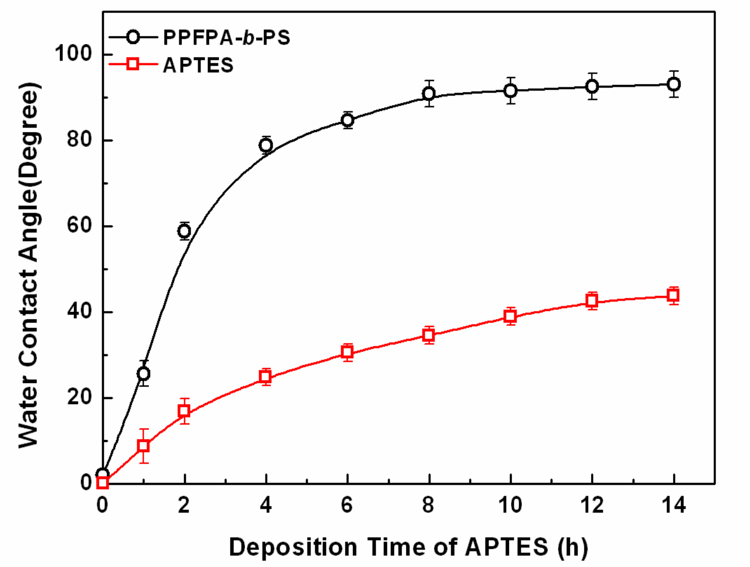

Figure 4.3 Water CA of APTES on mica (red-open square) and PPFPA-*b*-PS (black-open circle) on APTES treated mica as a function of APTES deposition time. The solid lines are added as the guidance.

4.3.2 Surface Morphology of PPFPA-*b*-PS grafted Mica Surface

In order to study the grafting behavior of polymers onto mica surface, surface morphology and roughness of PPFPA-*b*-PS grafted mica surfaces were characterized using AFM in tapping mode. Figure 4.4 shows the morphology and section-profiles of APTES treated mica surface and the as-obtained PPFPA-*b*-PS grafted mica surfaces *via* different deposition times (1 h and 10 h). As shown in Figure 4.4a (5 × 5 μm^2), APTES treated mica surface is flat and featureless with root-mean-square (RMS) roughness of 0.2 nm and the peak-valley value is less than 0.4 nm (Figure 4.4b). After grafting polymer, a smooth layer of particles is observed comparing with APTES deposited mica surface, and the measured RMS increases to 0.3 nm (Figure 4.4c, APTES deposition time ~2 h, water CA ~60^o). The measured peak-valley value reaches 0.8 nm (Figure 4.4d). When the deposition time of APTES reaches 10 h, the RMS value of grafted polymer surface goes up to 0.5 nm (Figure 4.4e), and water CA also increases to ~90^o. More importantly, the peak-valley value also increases from less than 0.4 nm for bare APTES surface to ca. 1.2 nm for end-grafted PPFPA-*b*-PS surface (Figure 4.4f). Comparing with the lower hydrophobicity surface (Figure 4b, water CA ~60^o), the polymer coating becomes denser and more particles with lateral size of several hundred of nm are observed for higher hydrophobicity surface (water CA ~ 91^o), suggesting the precursor amino-silane layer could influence the amount of grafted PPFPA-*b*-PS polymer, thus change the surface hydrophobicity.

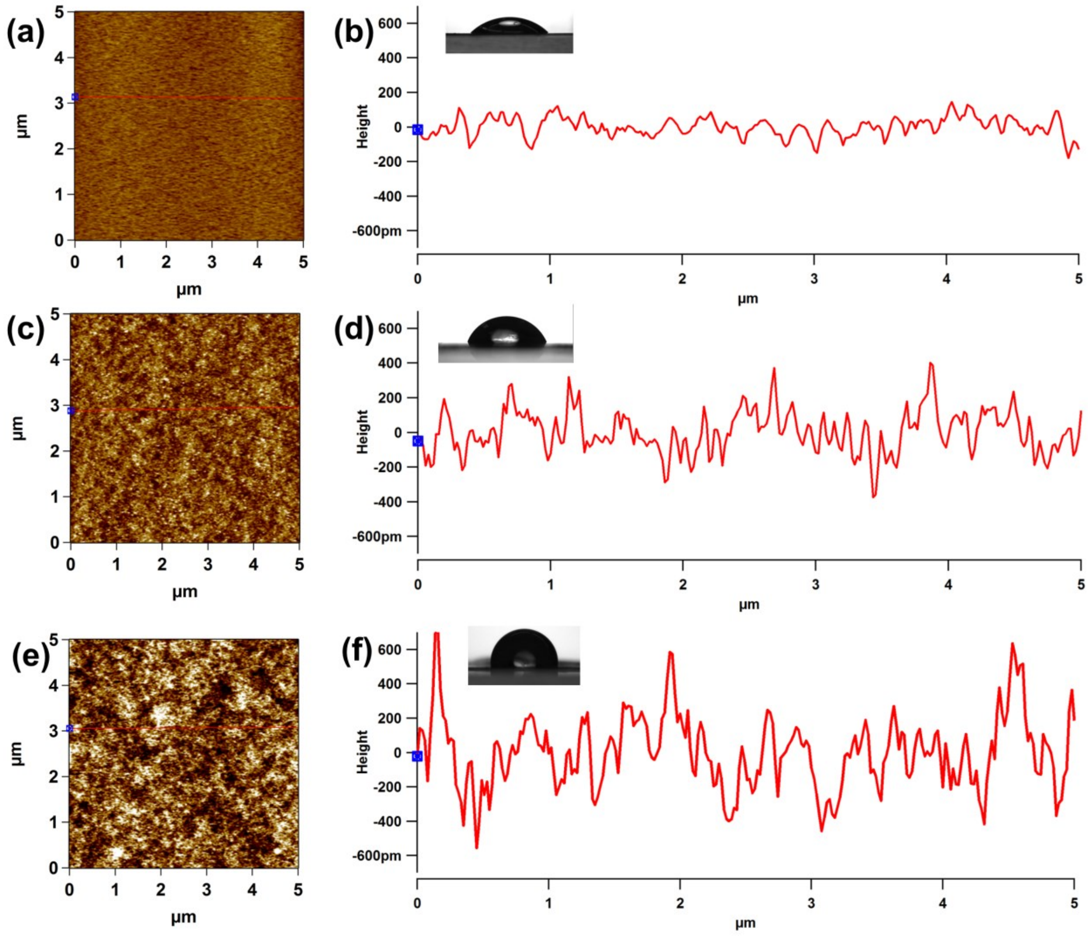

Figure 4.4 Topographic AFM images of (a) APTES deposited mica; (c) end grafted PPFPA-*b*-PS surface with low hydrophobicity (CA ~60°); (e) end grafted PPFPA-*b*-PS surface with high hydrophobicity (CA ~90°); (b, d, f) cross section line-scan profiles derived from the corresponding topographic AFM images (a, c and e).

4.3.3 XPS Measurement of APTES and PPFPA-*b*-PS Surfaces

The surface chemistry of APTES and end grafted PPFPA-*b*-PS films was further characterized by XPS (Figure 4.5). The XPS survey spectrum (Figure 4.5a) of APTES-treated mica shows the presence of Al, Si, K, C, O and N; while end-grafted PPFPA-*b*-PS surface only shows the characteristic peak of C, O and F. The element signals of Al, Si, K are due to mica substrate, which is widely known as a typical aluminosilicate that composed of $AlO(OH_2)_{2m}$ layers sandwiched between $(Si_2O_5)n$ layers with K^+ to be the positive ions for charge balance.[141] The strong signal of mica proves that the deposited APTES layer is quite thin (< 10 nm). Importantly, the N 1s peak shown in Figure 4.5b demonstrates the successful functionalization of APTES on water plasma activated mica surface. On the other hand, for PPFPA-*b*-PS surface, the signal intensity of N 1s peak clearly decreases compared with APTES treated mica, which could be mainly due to the coverage of PPFPA-*b*-PS polymer layer. Moreover, a sharp fluorine peak is also observed for PPFPA-*b*-PS sample (Figure 4.5 a,c), proving the existence of pentafluorophenyl-groups. The significant increase of C, F peak and absence of substrate signal provide direct evidence of successfully grafting polymer layers onto mica surface with good coverage. The XPS results here agree well with the AFM images shown in Figure 4.4, that a layer of PPFPA-*b*-PS polymer coating has been grafted onto mica surface.

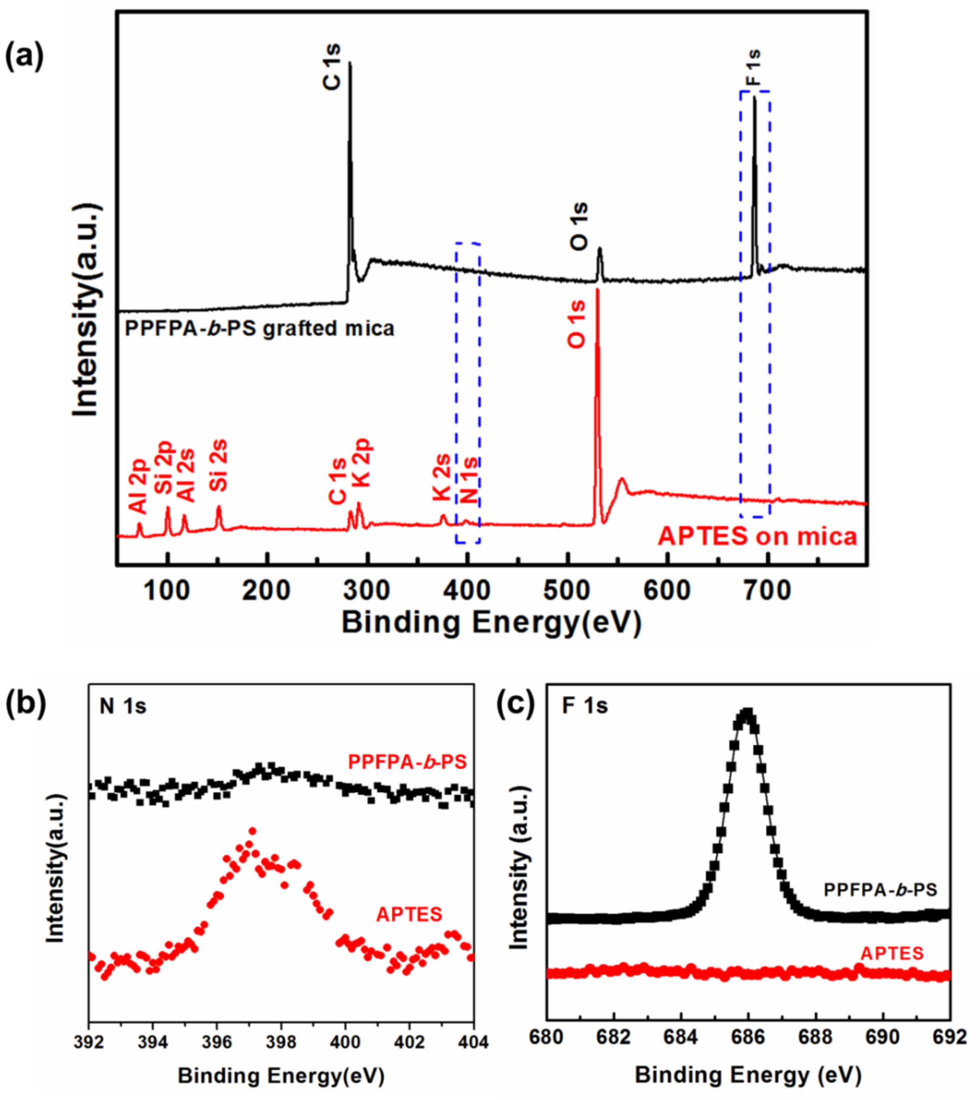

Figure 4.5 (a) XPS survey scan of APTES treated mica surface (red line) and end-grafted PPFPA-*b*-PS surface (black line) (b) fine scan of N 1s spectrum shown in a; (c) fine scan of F 1s spectrum shown in (a).

4.3.4 Stability of End-grafted PPFPA-*b*-PS Surface

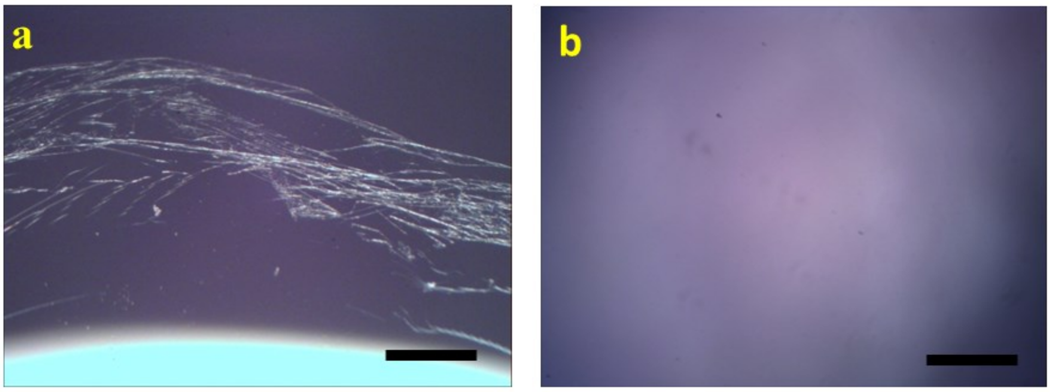

Figure 4.6 Optical images of spin coated polystyrene surface after conducting surface force measurement without (a) and with APTES layer (b), the scale bar is 100 μm.

Previous research suggest that physically adsorbed polymer films could easily get dewetted when immersed in water,[42] or under mechanic pressing,[8] especially when superhydrophilic surfaces such as mica has been used. In this research, mica surfaces before and after SFA experiments are characterized with optical microscope imaging, so as to check if the end grafted polymer film is stable enough under mechanic pressing in SFA experiment. As shown in Figure 4.6a and 4.6b, the spin coated PPFPA-*b*-PS film without APTES precursor layer could easily get detwetting after mechanic pressing in SFA with a normal load of ~20 mN/m in water, while the end-grafted surface is uniform without any obvious fracture, i.e., the dewetting behavior is not observed after continuous force measurement. Importantly, the end-grafted polymer films are found to be stable even after being immersed in water for 7 day, which is confirmed by the unchanged-surface morphology and water contact angle. Thus the chemical grafted polymer surfaces are more stable than physically adsorbed polystyrene films during surface force measurement. And the good stability of grafted polymer surface could rule out the influence of detwetting or rearrangement of polymer hydrophobic surfaces in aqueous solutions.

4.3.5 Contact Mechanics Measurement of PPFPA-*b*-PS Surfaces

Understanding the contact mechanics between polymer surfaces are important in many engineering and biological applications because contact mechanics can provide useful information on the surface deformation and adhesion[25,59] In this research, the contact mechanics between end-grafted PPFPA-*b*-PS surfaces were studied by SFA in air. The two surfaces were first brought into contact at zero-load, the loading process was achieved by applying gradually increased compressive load till a maximum load $F_\perp$ = 41.5 mN was reached, the unloading process was realized by reducing the applied load and followed by separation of the two contacted surfaces, both the loading and unloading rate ($dF_\perp/\mathrm{d}t$) was kept at ~0.2 mN/s. The two surfaces were kept at the maximum load $F_\perp$ for different contact time t_c ranging from 10s to 3600s. The surface deformation was monitored in situ and in real time using the Multiple Beam Interferometry technique.[102]

Figure 4.7a shows the typical plot of the contact diameter 2r as a function of the applied load, $F_\perp$, measured for two end grafted PPFPA-*b*-PS surfaces. When the two surfaces are brought towards each other using an electric motor, at some finite separation, the two surface “jump” into contact due to the attractive van der Waals force and contact adhesion when $F_\perp$ = 0, and a flattened circular contact area with a diameter $2r \sim 58$ μm if formed. When the two surface are further compressed, the contact diameter increases with increasing load, reaching $2r \sim 135$ μm at $F_{\perp} = 41.5$ mN. For the loading process, the widely used Johnson−Kendall−Roberts (JKR) theory could be used to fitting the contact radius of two elastically curved surfaces with increasing the normal load $F_{\perp}$ using Equation 4.2.[150,151]

$$r^3 = \frac{R}{K}\left(F_{\perp} + 3\pi RW + \sqrt{6\pi RF_{\perp}W + (3\pi RW)^2}\right) \tag{4.2}$$

$$\frac{1}{K} = \frac{3(1-\nu^2)}{2E} \tag{4.3}$$

where r is the contact radius, R is the radius of the surface curvature, K is the equivalent modulus which is related to Young's Modulus E of the surface material by Equation 4.3 (v is Poisson's ratio), $F_{\perp}$ is the normal load applied, and W is the adhesion energy between the two contacted surfaces (W=2γ for two surfaces of the same material). As shown in Figure 4.7a, the fitting curve (solid black line) agrees well with the experiment data with the fitted W to be 72 mJ/m^2. The fitted surface energy (γ=36 mJ/m^2) for end grafted polymer surface are comparable with previous reported thermodynamic surface energy value of 35-43 mJ/m^2 for polystyrene at room temperature.[143,180] For the unloading process, large adhesion is measured during separation. Theoretically, the adhesive force F_{ad} between two elastic bodies of the same material (i.e., sphere on a flat surface which is equivalent to the two crossed-cylinder configuration used in SFA), is related to the effective surface adhesion energy (W_{eff}) given by Equation 4.4 [24,25,106]

$$W_{\text{eff}} = 2F_{\text{ad}}/3\pi R \tag{4.4}$$

where R is the curvature of the surface. The calculated effective adhesion energies

W_{eff} for PPFPA-*b*-PS samples are 96 mJ/m^2 when the contact time is 30 s. Figure 4.7b shows the change of measured adhesion with different contact time ranging from 10s to 3600s. It is found that the effective adhesion energy increases with contact time at the same maximum normal load. The time-dependent adhesion between two end-grafted polymer surface agree with these previous studies,[24,143,156] confirm that the adhesion mechanism is mainly due to the enhanced polymer interdigitation of the polymer chains across the contact interface with prolonged contact time. Another important aspect is that the loading and unloading curve shows clearly adhesion hysteresis. Generally, the adhesion hysteresis suggests that taking apart two surfaces in contact dissipates more energy than bringing the surfaces together.[24, 157, 158] Plastic deformations, interdigitation / interpenetration of the surface functional groups or polymer chain ends, polar interaction, dynamic rearrangement and disentanglement of the polymer segments at contact interfaces could be the possible causes of adhesion hysteresis. [24,180]

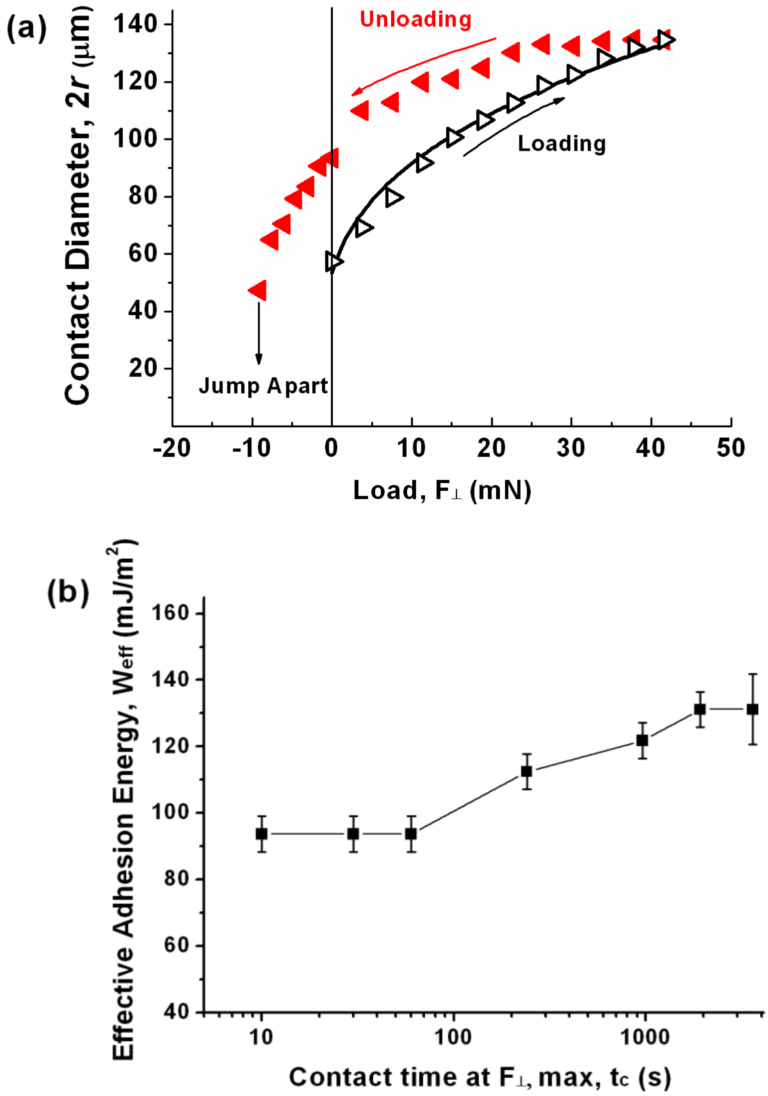

Figure 4.7 (a) Contact diameter 2*r* *vs.* applied load F$_\perp$ obtained through the JKR loading–unloading test for two PPFPA-*b*-PS films, the solid black line shows the JKR fitting curve. (b) Effective adhesion energy measured as a function of contact time at maximum load.

4.3.6 Interactions between End-grafted PPFPA-*b*-PS Surfaces

The interactions between two end-grafted PPFPA-*b*-PS surfaces in aqueous NaCl solutions were also measured using SFA. The effect of hydrophobicity, salt concentration and degassing has been investigated in detail in this section.

A) Effect of hydrophobicity

Hydrophobicity could greatly affect the water structure, the behavior of ions at interfaces, thus play critical roles for lots of engineering and biomedical applications.[1] In this study, two typical samples with low hydrophobicy (CA ~ 60^{o}) and high hydrophobicity (CA ~ 90^{o}) were chosen. Figure 4.8 shows the force-distance profiles on approach and separation, respectively, for two end-grafted PPFPA-*b*-PS mica surfaces with different hydrophobicity (*e.g.*, 60^{o} and 90^{o}), in 1 mM NaCl solution at neutral pH. Several features can be observed from the force-distance profiles. 1) The thickness of PPFPA-*b*-PS layer deposited on mica could be determined as half of the confined separation distance (or so-called hard-wall distance) when the two surfaces were brought into contact under relatively high load (~ 20 mN/m). And the zero separation distance (D=0) was defined as the mica-mica contact in air. The thickness of single polymer layers is measured to be ~11 nm and 13 nm for CA 60^{o} surface and CA 90^{o} surface, respectively. 2) Pure repulsion is measured when two PPFPA-*b*-PS surfaces (low hydrophobicity, CA 60^{o}) are approaching each other. However, long range attractive force (~ 100 nm) is measured for PPFPA-*b*-PS surface with higher hydrophobicity (CA 90^{o}). Generally, the observed force profiles during approaching could be attributed to the sum of several kinds of interactions, namely the DLVO interaction which includes attractive van der Waals forces and repulsive electrical double layer forces, the attractive hydrophobic interaction between hydrophobic domains on the surfaces, the repulsive hydrodynamic effect, the steric repulsion between surface asperities and aggregates and the possible bridging effect of micro-or nano- bubbles on polymer surface, especially for hydrophobic surface. The AFM fine scan shown in Figure 4.4 suggests that the grafted polymers are quite smooth with a peak-valley value less than 2 nm. And the covalent bonding state of the polymers minimize the chance of rearrangement for the grafted polymers on mica surface, thus the effect of steric repulsive due to polymer aggregates are negligible. Besides, the approaching speed of the two polymer surface is kept at 5-8 nm/s, so the repulsive hydrodynamic effect is also negligible. Polystyrene itself is a hydrophobic, neutral polymer, however, previous research showed that hydrophobic polystyrene/water interface will become negatively charged with hydroxyl ions selectively adsorbed onto surface, especially when aqueous solutions are saturated with air.[8, 33] The long range attraction (~100 nm) is close to the value reported previously based on two physically adsorbed polystyrene surfaces,[8] and the authors proved that micro-bubbles play important roles in the long range attraction. By considering all the factors mentioned above, the classic DLVO interactions, hydrophobic interaction and the bridging of bubbles could mainly contribute to the interaction of end-grafted PPFPA-*b*-PS surface under aqueous solution. For surface with low hydrophobicity, the electric double layer force between similar charged polymer surfaces could dominate the process during approaching. While for surface with high hydrophobicity, the effect of bubbles become more pronounced and needs to be considered during approaching. 3) Slight adhesion (~5 mN/m) is measured for surface with low hydrophobicity, while large adhesion (~280 mN/m) is observed when separating two end-grafted polymer surfaces with high hydrophobicity. The jump out are generally mechanical instabilities that occurs when the gradient of the force-distance profile is greater than the spring constant. The adhesive force measured during separation was mainly due to vDW force between two end-grafted PPFPA-*b*-PS surfaces and entanglement of grafted polymer chains. The increasing of adhesion could be attributed to the combination of higher probability for interpenetration of polymer chains at the contact interface when higher amount of polymer is presented, and at the mean time, higher surface hydrophobicity allowing a more intimate contact of the contacted hydrophobic polymer surface.[1,25,143]

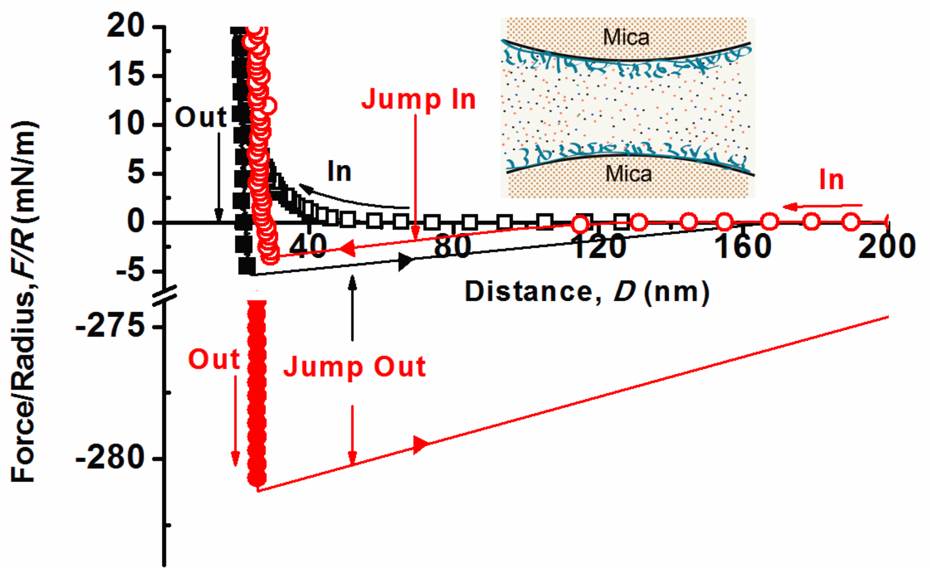

Figure 4.8 Force-distance profiles on approach and separation, respectively, for two end-grafted PPFPA-*b*-PS mica surfaces, with low hydrophobicity (shown in black, CA ~60°), high hydrophobicity (shown in red, CA ~90°), in 1 mM NaCl solution at neutral pH. The open symbols represent approaching and the filled symbols suggest separation. The inset shows the schematic view of two grafted polymer surface in 1 mM NaCl solution.

B) Effect of Salt Concentration

In order to confirm the origin of the measured repulsion and attraction during approaching process, we increase the concentration of NaCl to 100 mM so as to study the effect of ionic strength. In this study, the electrical static interaction would be restrained due to the decreasing of Debye length (~ 1 nm) in 100 mM NaCl. As shown in Figure 4.9, for low hydrophobicity surface (CA ~ 60^o), the repulsion range decreases to ~15 nm in 100 mM NaCl during approaching comparing with the relatively longer range of repulsion (~ 40 nm) measured in 1 mM NaCl. At mean time, the measured adhesion also decreases (black filled square), which could be attributed to the increased entropy effect of hydrated ions that reduces the chance of polymer interdigitation at the interface.[1,25] On the other hand, for chemical grafted surfaces with higher hydrophobicity(CA ~90 degree), the increasing of salt concentration will dramatically reduce the attraction force range to ~20 nm. Previous research suggested that there is strong connection between the long range attraction(> 50 nm) and dissolved gas on physically adsorbed polystyrene surface, and the increased ionic strength will reduce the amount of dissolved gas in the solution, thus reduce the attraction force range.[8, 174] In this study, the reducing of long range attraction when increasing salt concentration also provide indirect evidence for the existence of gas bubbles [181, 182] or gas layer at the interface.[183,184] Additionally, the measured adhesion in 100 mM NaCl also decreases compared to separation two PPFPA-*b*-PS surface in 1 mM NaCl, which could be due to the reduced chain interdigitation and increased steric effect when large amount of salt ions is presented at the interface.

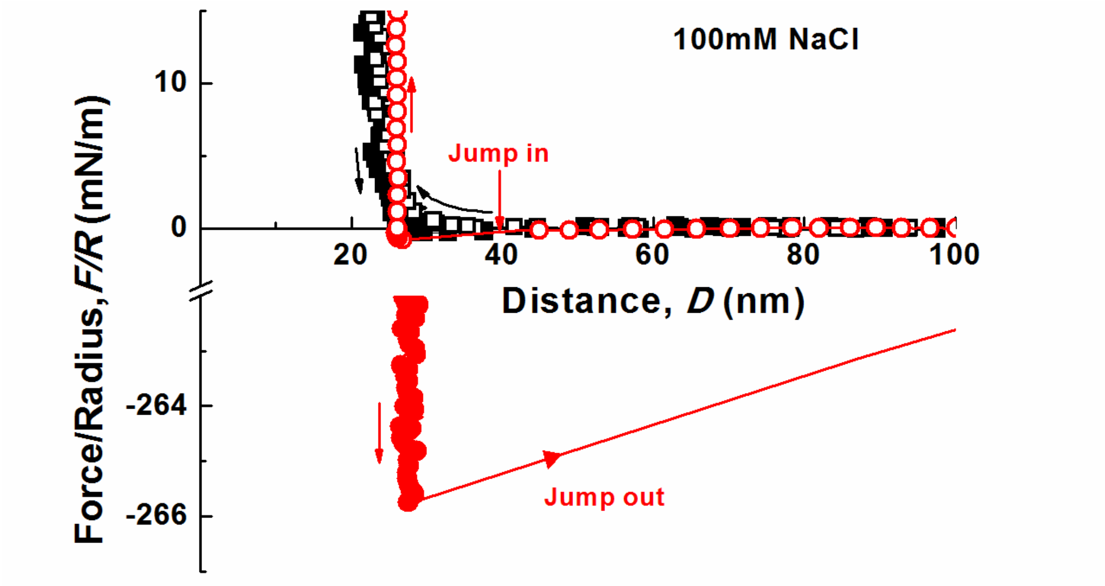

Figure 4.9 Force-distance profiles of PPFPA-*b*-PS surface in 100 mM NaCl solution, the black line and red line represent two surfaces with low hydrophobicity (water CA ~ 60^o), and high hydrophobicity (water CA ~ 90^o), respectively. The open symbols suggest approaching while the filled symbols indicate separation.

C) Effect of degassing

In order to further confirm the role of gas on the measured long range attraction, the degassing experiment has been conducted when measuring the interactions between PPFPA-*b*-PS surfaces with high hydrophobicity (water CA ~ 90^o). Figure 4.10 shows the typical force-distance plot before (red) and after (black) degassing during approaching. It is observed that the jump in distance decreases from ~120 nm in non-degassed NaCl solutions to ~ 70 nm in degassed solutions. It is worth mention that the measured attraction range after degassing is still larger than that measured in high concentration of salt, which could be due to the incomplete-degassing of the solution using simple mechanic pump, and the gases may quickly dissolve into the solutions during measurement. Overall, our SFA results proves that the long-range force measured by SFA could be influenced by both salt and degassing, which agree well with previous study based on physically adsorbed polystyrene surface, however, for this case, the rearrangement or dewetting of polymers on the surface could be totally excluded.[1,25]

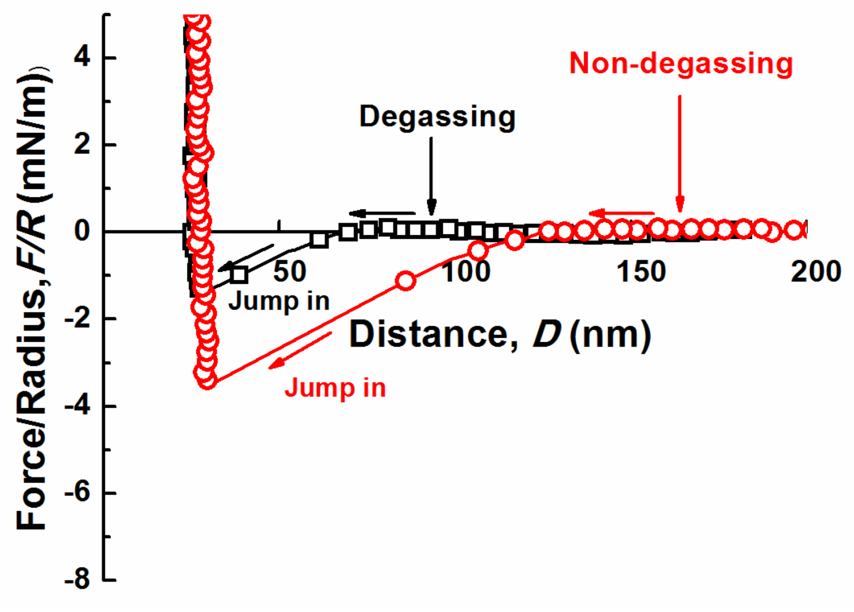

Figure 4.10 Approaching force-distance profiles of PPFPA-*b*-PS surface in 1 mM NaCl solution before (red) and after (black) degassing.

4.4 Conclusion

Chemical grafted, stable polymer coatings play important roles for scientific research and engineering applications. In this study, we reported the preparation of smooth poly(pentafluorophenyl acrylate)-*b*-polystyrene (PPFPA-*b*-PS) layers covalently end-attached to mica surface by using a "graft to" methodology. The grafting of the polymers was achieved *via* primary amines reacting with active petal-fluoro esters. The hydrophobicity of grafted mica surface can be modulated by adjusting the deposition time of the precursor layer (3-Aminopropyl) triethoxysilane (APTES). The interactions between grafted PPFPA-*b*-PS surfaces in aqueous solutions were systematically measured as a function of separation distance using a Surface Forces Apparatus. Pure repulsive forces were measured during approaching of two grafted polymer surfaces with relatively low hydrophobicity (water contact angle, CA ~60°). However, long-range attractive forces were detected for surfaces with higher CA (~90°). Both degassing and increasing NaCl concentrations led to shortened range of attraction, indicating the important role of dissolved gas or surface-supported bubbles on the long range attraction between hydrophobic polymer surfaces in aqueous media. Importantly, the as-obtained polymer films show good stability after compressing during continuous force measurement. The force-distance results obtained based on end-grafted PPFPA-*b*-PS surfaces provide fundamental insights into the molecular interaction mechanism of polymers acting on mica surfaces through chemical bondings, with implications in many related areas.

CHAPTER 5

MULTIFUNCTIONAL POLYMERIC FILMS PREPARED BY A FAST AND COVALENT BONDED LAYER-BY-LAYER ASSEMBLY PROCESS

5.1 Introduction

Thin multi-component films have attracted great research interests recently due to its versatile applications in areas such as sensors,[185] integrated optics,[186] friction-reducing coatings,[187] biological surfaces[188] and membrane design.[189] The layer-by-layer (LbL) deposition is a convenient and versatile route to fabricate thin multi-component films for decades. Traditional LbL deposition process is generally achieved by dipping technique, where polyelectrolyte chains or active species will diffuse toward the substrate mainly under the influence of electrostatic interaction and followed by chains rearrangement on the surface. Lots of factors such as adsorption time, concentration of the polyelectrolyte, pH and ionic strength should be considered.[190,191] The typical dipping LbL deposition process is usually time consuming (at least hours for preparing thick polymer films). Therefore, a more effiency route for preparing multi-component thin films is needed. The spin-assisted deposition process is mainly influenced by the centrifugal force, viscous force and air shear force in addition to electrostatic interactions.[192-194] The rearrangement of polymer chains onto a substrate, and the desorption of weakly bound chains happens in a very short time (< 1 min). Thus, the spin-assisted LbL deposition can obtain multi-component films more efficiently as compared to the dipping LbL technique.[191] Additionally, this technique also facilitates the precise control of film thickness by simply adjusting the spin speed and polymer concentration.

Multi-component films obtained by LbL method through electrostatic interactions generally suffer from chemical and mechanical weakness, especially in high-salt environment, those weakly adsorbed polyelectrolyte chains will diffuse and further increase the surface roughness of the films, which will result in poor-film-quality.[191] Hence, robust layer-by-layer deposited films exploiting other interactions are desirable. Recently, the scope of LbL assembling has been widely extended by employing other interactions such as hydrogen bonding,[195] crosslinker chemistry,[196,197] charge-transfer[198] and so on. Among those interactions, crosslinker chemistry that proceeded rapidly with high yields under mild conditions for creating robust organic coatings has attracted much attention.[196,199] The reaction between activated esters with amines, first reported in 1972,[200, 201] is one of the useful synthetic methods in amine-reactive crosslinker chemistry. Poly (pentafluorophenyl acrylate), PPFPA, is an active pentafluorophenyl ester that reacts with aliphatic amines and aromatic amines under mild conditions with short reaction time.[167, 202] This reagent provides versatile ways for grafting polymeric materials onto amine functionalized surfaces. In addition, the interfacial layers that contain un-reacted pentafluorophenyl ester groups or amine groups can facilitate post-polymerization and the preparation of multifunctional surfaces. Chemical compounds such as carboxyl reagents or dye molecules have been successfully incorporated into those multi-layer structure.[199, 203] So far as we know, much work has been focused on preparation and characterization of covalent bonded LbL films based on time-consuming dipping process, an efficiency method for preparing robust, covalent bonded LbL film using the spin-assisted deposition has not been reported yet, understanding on the surface interactions between LbL films is also quite limited. Moreover, freestanding covalent bonded polymeric film with excellent flexibility and integrity was seldom reported before.

In this chapter, we reported an efficiency way of preparing multi-layer polymer film based on covalent bonding between active ester and primary amines using spin casting LbL deposition. Highly branched polymer polyethyleneimine (PEI) which contains both prime amine, secondary, and tertiary amine (ratio 1:2:1) and active ester copolymerized polystyrene polymer, polypentafluorophenylacrylate-*b*-polystyrene (PPFPA-*b*-PS) were selected as typical amine and active ester polymer, respectively. The film shows switched hydrophobicity by alternated deposition of PEI layers (hydrophilic) and PPFPA-*b*-PS layers (hydrophobic). The interactions forces between the as-obtained multi-layer films in aqueous solutions were also measured by using the SFA technique under different experimental configurations. Strong adhesion was measured between PEI and PPFPA-*b*-PS, which shows significant stretching behavior before the two surfaces were separated.

Post treatment of multi-layer polymer films by immersing those films in different solutions suggested that this multi-layer film has very good stability in organic solvent but could become freestanding after immersing in 1 M NaOH or 1 M HCl for several hours. Interestingly, the obtained free-standing film is rather stable in acid, base and organic solvents for more than 2 weeks, mostly probably due to the covalent bonded network of the films. On the other hand, by immersing the amine-rich multi-layer polymer film in perfluoro caprylic acid (PFOA), those excess amines could further react with carboxyl groups and produce surfaces with higher hydrophobicity (water contact angle to be 125^o). Overall, the PPFPA-*b*-PS & PEI multilayer films we obtained demonstrate great potential for preparing multifunctional surfaces in the future.

5.2 Experiment Section

5.2.1 Materials

Highly branched poly(ethyleneimine) (branched PEI, average M_w ~25000) containing primary, secondary and tertiary amine groups (ratio 1:2:1) and chemicals for polymer synthesis were purchased from Sigma-Aldrich. Ruby mica sheets were purchased from S & J Trading Inc. (GlenOaks, NY). Silicon wafer was bought from Nanofab in University of Alberta, glass slides were bought from Fisher Scientific (Canada). Milli-Q water with a resistance of ≥18.2 MΩ·cm was used for preparing aqueous solutions. Azobisisobutyronitrile (AIBN) was purified by recrystallized twice from ethanol. Styrene was passed through a short column of basic aluminum oxide to remove inhibitor. Pentafluorophenyl acrylate (PFPA) and Reversible Addition-Fragmentation Chain Transfer (RAFT) agent, 2-(dodecylthiocarbonothioylthio)-2-methylpropionic acid (DDMAT), were synthesis according to the procedures reported in references.[171, 176] The preparation of poly(pentafluorophenyl acrylate)-*block*-polystyrene (PPFPA-*b*-PS) polymer was follow the same route described in Chapter 4, and a concentration of 0.5 wt% in toluene was prepared for further spin coating method.

5.2.2 Polymer Synthesizing and Reaction Mechanism

Figure 5.1 shows the chemical structure and reaction mechanism for poly(ethyleneimine), PEI, and Poly(pentafluorophenyl acrylate)-*block*-polystyrene, PPFPA-*b*-PS, forming covalent bonded multi-layer structure. The PEI has both primary and secondary amine which could react quickly with PPFPA groups on the side chain of PPFPA-*b*-PS in minutes. The functional block copolymer, PPFPA-*b*-PS, was prepared by RAFT polymerization using a PFPA based macro-RAFT agent as described in Chapter 4. Briefly, the macro-RAFT agent, $PPFPA_{-30}$, was synthesized by polymerization of PFPA in dioxane using DDMAT as the chain transfer agent and AIBN as initiator. The synthesized polymer was diluted with dichloromethane and precipitated into methanol for three times. The molecular weight for the macro-raft agent was measured to be $M_{n,NMR} = 7140$ kg/mol;. $M_{n,GPC} = 8,000$ kg/mol, $M_w/M_n = 1.10$. The block copolymer, PPFPA-*b*-PS, was obtained by copolymerization of $PPFPA_{30}$ with styrene using AIBN as the initiator. The polymer was diluted with chloroform and precipitated into methanol three times. The molecular weight of the product was measured to be $M_{n,NMR} = 97140$ kg/mol;. $M_{n,GPC} = 100,000$ kg/mol,

$M_w/M_n = 1.10$.

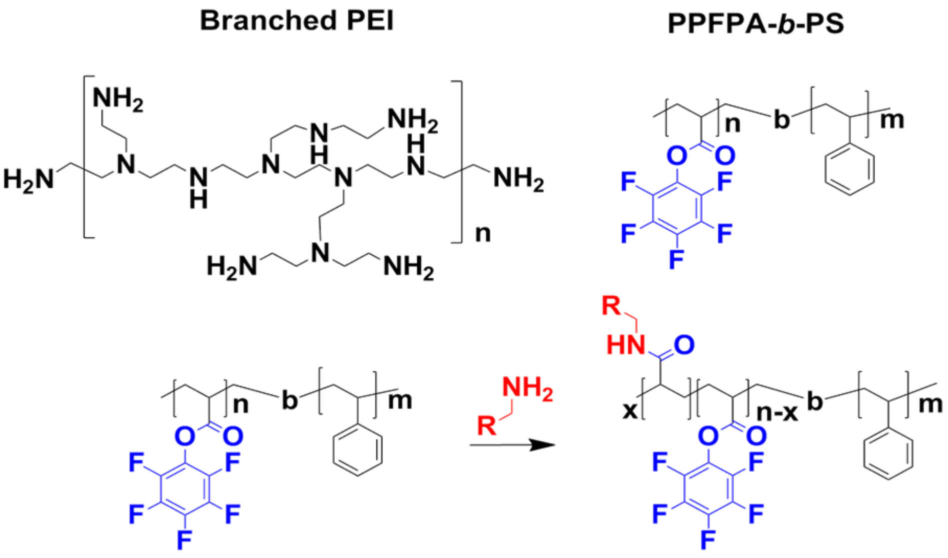

Figure 5.1 Chemical structure of branched polyethylenimine (PEI) and Poly(pentafluorophenyl acrylate)-*block*-polystyrene and PPFPA-*b*-PS. The bottom formula shows the chemical reaction between PPFPA-*b*-PS active ester and primary amine.

5.2.3 Spin Casting

The spin casting was conducted using a KW-40 spin coating machine. The sample holder were first kept at low spin speed (< 500 rpm) for 5 s, and then increased to a higher rotation speed (1500 rpm/s) and kept for another 40 s. For the spin coating process (Figure 5.2), generally there are two ways to disperse the solution onto the flat substrate, either through static disperse or dynamic dispense. The static disperse method add the liquid drop before spinning and is suitable for liquids with large viscosity and good wettability on substrate. The dynamic dispense method is dispensing the liquid drop while the substrate is rotating (usually first at low speed, then increase to speed to get thin films). Spreading of the liquid takes place due to centrifugal force and air shear force during high speed spinning. The dynamic dispense method is more suitable when the liquid itself has poor wettability on the substrate, and this method also has the advantage of eliminating voids and defects that may form using other coating method. Due to the poor wettability and easily evaporation property of toluene and acetone, the dynamic dispense method with a spin speed of 1500 rpm are chosen to prepare multi-layer PEI & PPFPA-*b*-PS polymer films.

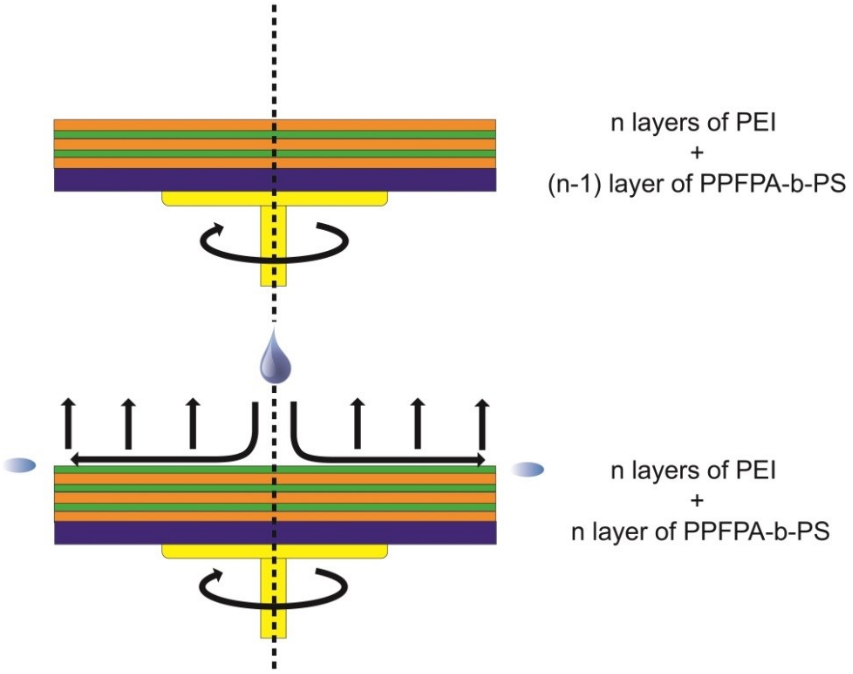

Figure 5.2 Schematic illustration of the spin coating process for preparing multilayer PEI and PPFPA-*b*-PS polymer films.

5.2.4 Solution and Substrates

PEI solution was prepared by dissolving highly branched PEI in acetone at 0.2-1.0 wt%. PPFPA-*b*-PS was dissolved in toluene with a weight percentage of

0.2-2.5 wt%. Four types of substrates, fresh cleaved mica, gold coated mica, silicon wafer and transparent glass slides were chosen as typical coating subjects to measure different properties: fresh cleaved mica surfaces were used for morphology imaging using AFM technique, gold coated mica surface were used for Fourier Transform Infrared Spectroscopy measurement, silicon surfaces were used for ellipsometry measurement, glass slides (2 × 2 cm) were used for transparency measurement. All types of substrates were first treated with UV ozone for 15 min, and then cleaned with acetone and ethanol mixture (50:50 vol%) in ultrasonic cleaner for 10 min, and blow-dryed with N_2 to remove possible organic contamination.

5.2.5 Atomic Force Microscope for Topography Imaging

Morphology of LbL assembled multi-layers on mica and silica were characterized with an Atomic Force Microscope (Bruker Icon, USA). Silica cantilevers (Bruker Nano) with a nominal resonance frequency of 300−400 kHz and spring constant of ~ 40 N/m were used for tapping mode imaging. The peak-force mode was employed during AFM characterization.

5.3 Results and Discussion

5.3.1 Contact Angle Measurement

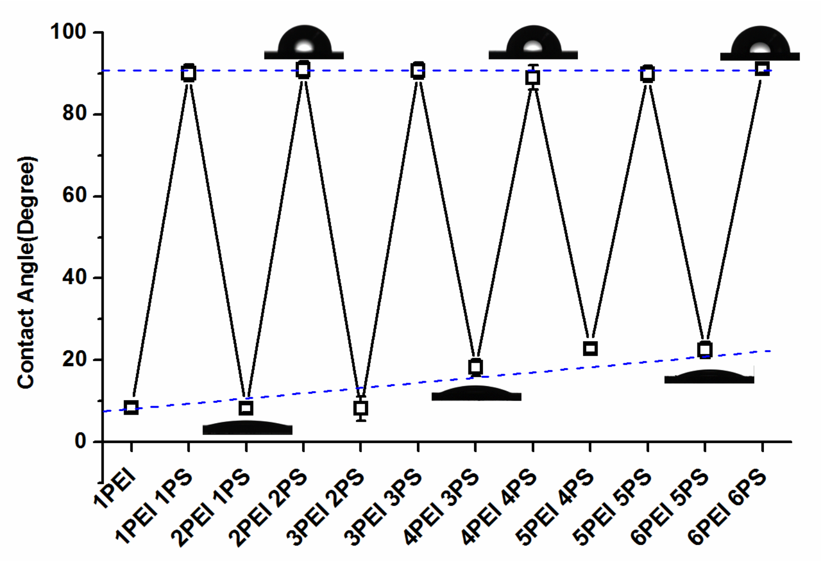

Figure 5.3 Contact angle *vs.* polymer coating layers on silicon substrates. The insets show the contact angle image of water on polymer films. PEI stands for polyethyleneimine and PS stands for poly(pentafluorophenyl acrylate)-*block*-polystyrene.

Water contact angle has been employed to assess the hydrophobicity of alternated deposited multi-layer polymer surface. PEI is a hydrophilic polymer due to the large amount of polar amine groups while the PPFPA-*b*-PS film is a hydrophobic polymer due to the hydrocarbon chains and aromatic rings. As shown in Figure 5.3, alternated hydrophobicity switching between hydrophobic and hydrophilic is achieved by sequence depositing PEI or PPFPA-*b*-PS polymer. And the static contact angle of PEI exposed surface gradually increases from less than 10^o to about 20^o with the increasing of deposited layers, probably due to the increase of surface roughness and the expose of PPFPA-*b*-PS chains underneath PEI layer. However, for surfaces with PPFPA-*b*-PS polymer layer on the top, the water contact angle stays at 89°±3°. The alternated hydrophobicity switching during deposition could be further applied for preparing superhydrophobic or superhydrophilic surfaces in the future.

5.3.2 Film Thickness Measurement

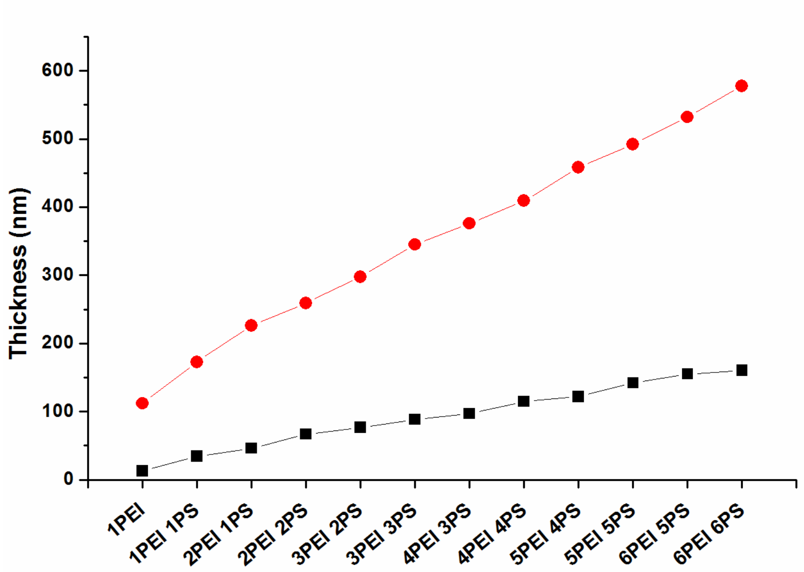

Figure 5.4 Thickness measurement of PEI & PPFPA-*b*-PS multi-layer films, PS stands for PPFPA-*b*-PS polymer in this case, the solid black square stands for the case with lower concentration of PEI (0.2 wt%) and PPFPA-*b*-PS (0.5 wt%), the solid red circle stands for the case with high concentration of PEI (1 wt%) and PPFPA-*b*-PS (2.5 wt %).

Ellipsometry has been employed to monitor the thickness change after each spin coating step. Figure 5.4 shows the film thickness as a function of deposition layers at both high concentration (1 wt% PEI in acetone, 2.5 wt% PPFPA-*b*-PS in toluene) and low concentration (0.2 wt% PEI in acetone, 0.5 wt% PPFPA-*b*-PS in toluene) of polymer reagents. It is noted that the thickness of film increases almost linearly for the two different concentrations. And when low concentrations (i.e., 0.2 wt% of PEI and 0.5 wt% of PPFPA-*b*-PS) are used, the film thickness gradually increases from less than 20 nm to 200 nm after deposition with 6 bi-layers. However, when the concentration of polymer increased by five-fold, the thickness of obtained film increases from 100 nm to 550 nm after deposition for 6 bi-layers. The ellipsometry results here prove that the thickness of polymer film could be adjusted in a wide range from less than 20 nm to more than 550 nm by simply changing the solution concentrations. Another alternated way for adjusting the film thickness would be changing the spin speed for coating process. Higher spin speeds generally lead to large centrifuge force and air shear force, which will lead to a thinner film. In this research, in order to reduce the number of variables, the spin speed is fixed at 1500 rpm/min and the polymer concentration was adjusted to different concentrations. It is worth mention that it takes less than 10 min to prepare a multi-layer polymeric sample with the thickness to be greater than 500 nm. The deposition rate (50 nm/min) is much higher than previous reported value employing dipping method.[199]

5.3.3 Transparency Measurement

The optical property of the polymeric thin film such as transparency has also been tested. Figure 5.5 shows the UV-Vis absorption spectrum of thin film deposited on transparent glass slides. And it is found that the transparency for visible light region can reach as high as ~ 90 % after repeated deposition for 10 bi-layers, proving that the polymer film should be in amorphous state regardless of thickness. The transparent polymer multi-layer film could be employed for preparing transparent conductive polymer films when conductive nanowires were incorporated.[204]

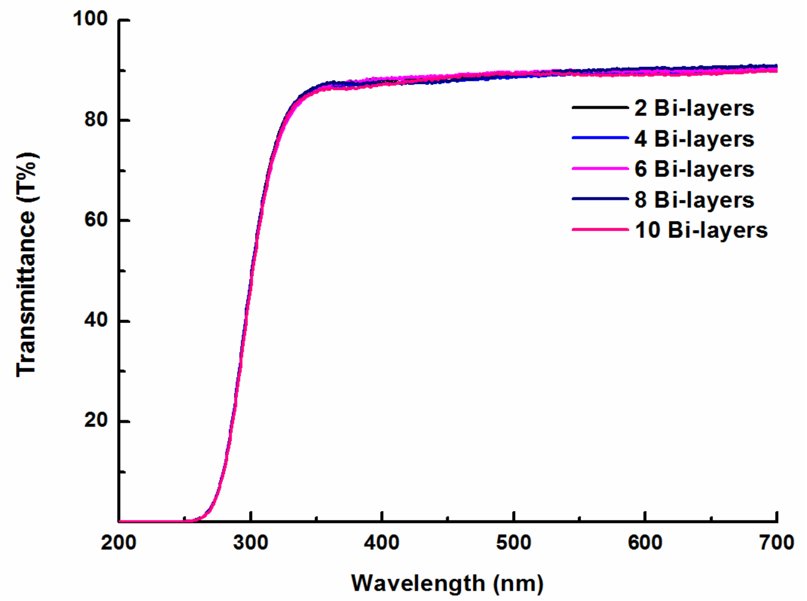

Figure 5.5 Transmitted spectrum for spin assist layer-by layer deposited polymer film with different bilayer numbers.

5.3.4 XPS Measurement

XPS measurement was conducted to study the elements composition of multilayer polymer films, and two samples with either PEI or PPFPA-*b*-PS on top are chosen for characterization. Before XPS measurement, those prepared PEI and PPFPA-*b*-PS polymeric films are thoroughly washed with both acetone and toluene in ultrasonic bath to remove possible un-bonded polymer reagents. Figure 5.6 shows the full survey XPS scan for multi-layer polymeric film with either PEI (red line) or PPFPA-*b*-PS (black line) polymer on the top. Several interesting features could be observed. Firstly, the semi-quantitative calculation based on the survey spectrum indicates that the atomic ratio of C:N decreases from 20:1 to around 3:1 when the top layer changes from PPFPA to PEI. The increasing of nitrogen concentration was mainly due to large amount of amine groups in PEI. Secondly, the fluorine signal of 3PEI-3PS sample (PS layer on the top) decreases obviously after coating with one more layer of PEI layer, and the calculated atomic ratio of N:F increases from 4.6:1 to about 230:1. The XPS results suggest the possible existence of free active ester and amine groups in the multi-layer polymer film, especially for amine groups, which will facilitates post-treatment of the obtained multi-layer polymer film. However, due to the detection limitation of XPS, this technique can only provide information about the element composition at the range of 5-10 nm on top of the surface.

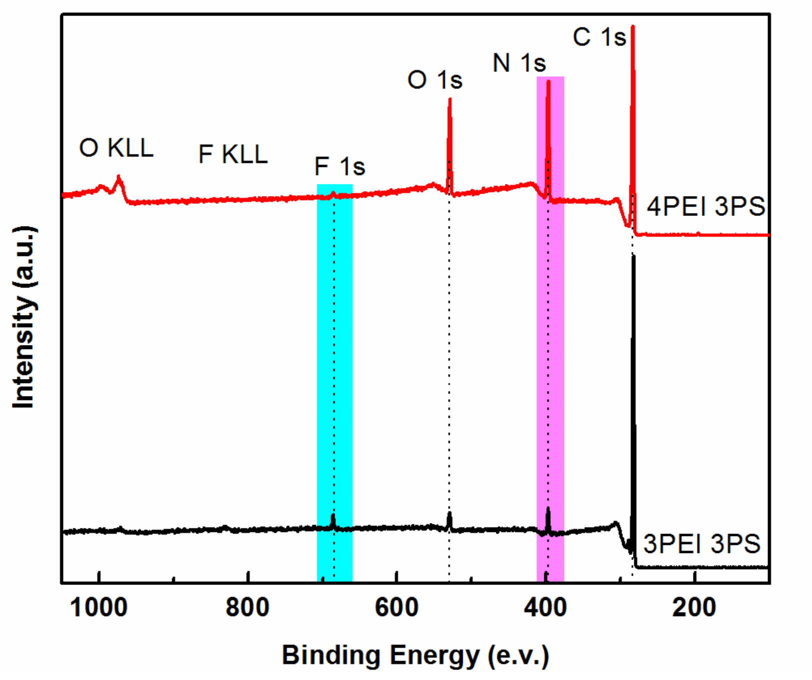

Figure 5.6 XPS survey spectrum of spin deposited polymer thin films with either PEI (red line) or PPFPA-*b*-PS (black line) on top, respectively. PS stands for PPFPA-*b*-PS polymer in this case.

5.3.5 FTIR results

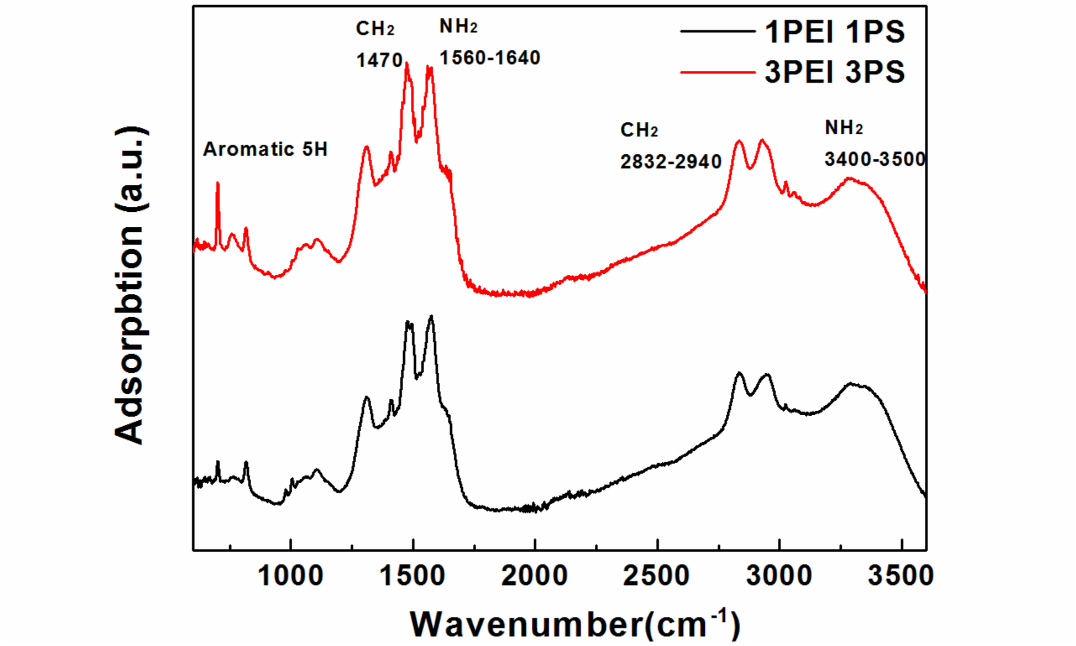

Figure 5.7 FTIR spectrum of single bi-layer (1PEI-1PS, black line) and three bi-layer (3PEI-3PS, red line) polymer films.

In order to understand the chemical bonding state in the polymer films, Attenuated Total Reflectance Fourier Transform Infrared Spectroscopy (ATR-FTIR) measurement has been conducted. The polymer films are deposited on gold-coated mica surface (~40 nm) so as to obtain the resonance FTIR signal during measurement. Figure 5.7 shows the typical ATR-FTIR spectrum of one bi-layer and three bi-layers of PEI & PPFPA-*b*-PS film. The FTIR spectrum shows four features: a) there are large amount of free amine groups (peak position 1560-1640 cm^{-1} and 3400-3500 cm^{-1}) in the polymer film; b) the signal intensity of benzene ring (700-900 cm^{-1}) increases, which is due to the increased amount of PPFPA-*b*-PS in the multi-layer film. c) the active carbonyl group of the poly(active ester) at the range of 1730-1830 cm^{-1} is not observed for both single layer and three bi-layer polymer surfaces, proving most of the active esters have reacted with amine groups in PEI layer.[171] However, according to the XPS measurement, the conversion rate of active ester and amine may not be 100% because a large amount of fluorine (>1% atomic ratio) was measured in the polymer film, especially when PPFPA-*b*-PS layer is on the top; d) other characteristic bands are mostly assigned to -CH_2 vibration at 1470 cm^{-1} and 2832-2940 cm^{-1}, respectively. The large amount of free amine could facilitate further functionalization of the multi-layer polymer surface, which will be mentioned in the following sections.

5.3.6 AFM Images

In order to understand the deposition behavior of polymers during each step, fresh cleaved mica surfaces spin coated with polymer films are imaged with the AFM technique. Figure 5.8 shows the morphology of bare mica surface and as-obtained single or multi-layer polymer films measured by AFM. Fresh cleaved mica surface is featureless with mean square roughness less than 0.1 nm (Figure 5.8 a, b), and the peak-valley height fluctuation is less than 0.2 nm (Figure 5.8 c). After depositing with PEI layer, small particles are observed on the surface (Figure 5.8 d, e), and the peak-valley height fluctuation increases to 1 nm (Figure 5.8 f). Further depositing a layer of PPFPA-*b*-PS will increase the surface roughness to 0.3 nm, which is shown in Figure 5.8 g, h. At mean time, more scattered particles with the height of several nanometers are observed. The peak-valley value is measured to be 5 ~ nm for single bi-layer (Figure 5.8i). For three bi-layer of PEI & PPFPA-*b*-PS on mica surfaces, the film roughness increase to 2 nm (Figure 5.8j, k) and the peak-valley height fluctuation further increases to ~ 20 nm (Figure 5.8l). The AFM results here indicate a quick rise in roughness when the number of bi-layer increases. And the surface roughness could greatly influence the surface interactions, which will be mentioned in later sections.

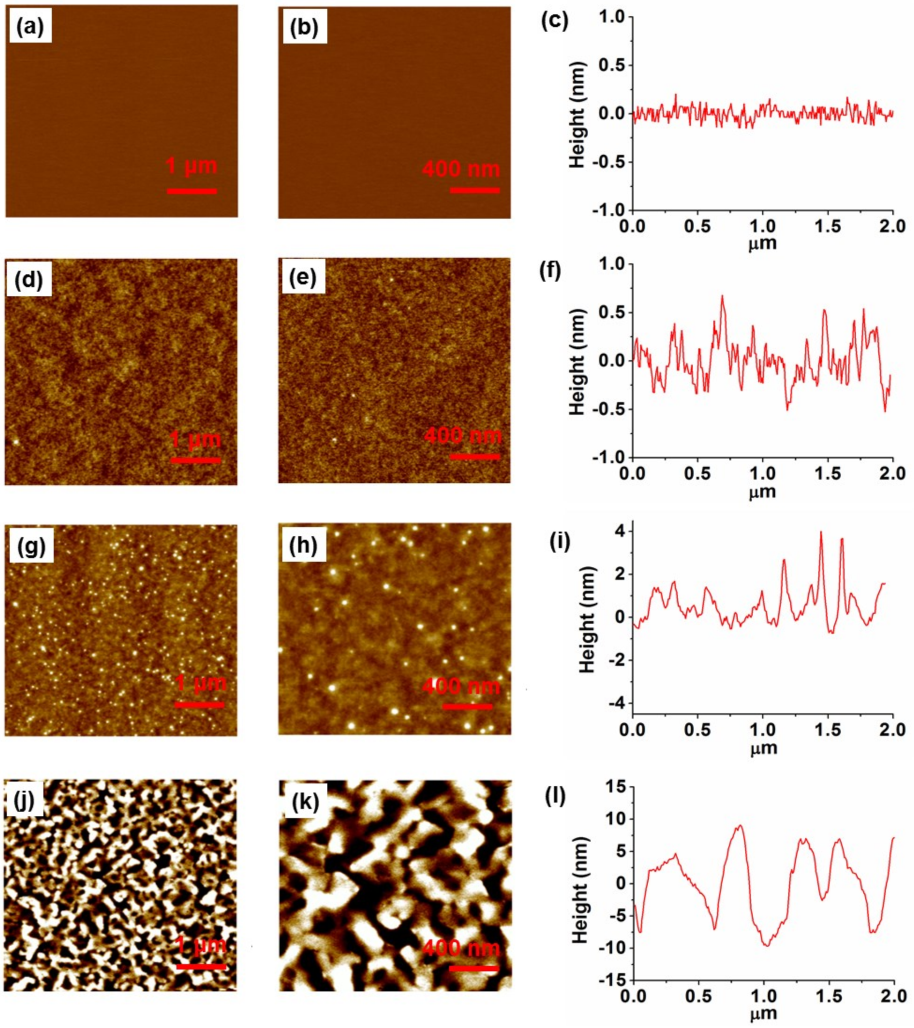

Figure 5.8 AFM images and cross-section profiles of spin assisted LbL polymer thin films with different layers, (a-c) fresh cleaved mica, (d-f) PEI coated mica surface, (g-i) single bilayer of PEI and PPFPA-*b*-PS polymer (j-l) three bi-layers of PEI and PPFPA-*b*-PS polymer surfaces.

5.3.7 Stability Test of PEI and PPFPA-*b*-PS Films

Stability of polymeric films plays an important role for engineering applications. In this research, polymeric films (PEI&PPFPA-b-PS)n obtained on silicon surface with differet bilayer numbers have been immersed into different solutions, including strong base (1 M NaOH), strong acid (1 M HCl), high concentration of salt (1 M NaCl), typical organic solvents such as toluene, tetrahydrofuran and aceton for 48 h, respectively. As shown in Table 5.1, (PEI&PPFPA-b-PS)$_n$ films are quite stable in high salt concentration (1 M NaCl), but the films will be automatically peeled off from silicon substrate after immersing in 1 M HCl or 1 M NaOH for 48 h. It has been reported that the isoelectric point of silicon dioxide is between 1.7-3.5,[1] under strong acid solution, the silicon dioxide surface could become positve charged, and the protonated PEI layer is also positve charged, thus the repulsion between the PEI layer and silicon dioxide layer will play dominate roles, which will lead to the peel off of multilayer films from silicon wafer. On the other hand, for the case of strong base, the peeling off of polymer layers could be mainly due to the chemical reaction between thin layer of silicon dioxide and concentrated hydroxyl ions that will reduce the bonding strength between PEI layer and silicon wafer, as evidencd by the uneven surface obtained after the polymer layers was peeled off in strong base. On the other hand, the multilayer film shows excellent stability in tetrahydrofuran, toluene and aceton, even at elevated temperature(< 80 ^{o}C), which further demonstrates the intrisic covalent bonding between polymer layers. Another interesting point is that the same result for stability test was obtained for polymer films with different bilayer numbers, suggesting film thickness will not affect the film stability. The excellent stability of PEI&PPFPA-*b*-PS coatings in organic solvents prove that this film may have potential applications in surface coatings of pipelines for engineering applications.

Table 5.1 Stability test of spin-assist deposited PEI and PPFPA-*b*-PS thin film on silicon surface, here "S" stands for staying on the substrate, "F" stand for freestanding.

	1M NaCl	**1M HCl**	**1M NaOH**	**Acetone**	**Tetrahydrofuran**	**Toluene**
1PEI + 1PPFPA-*b*-PS	S	F	F	S	S	S
3PEI + 3PPFPA-*b*-PS	S	F	F	S	S	S
6PEI+ 6PPFPA-*b*-PS	S	F	F	S	S	S

5.3.8 Surface Force Measurement

On the basis of studying the deposition behaviors and composition of PEI & PPFPA-*b*-PS film on mica surfaces, the interaction forces between two spin-assisted LbL deposited polymer surfaces were also measured by SFA technique. The obtained SFA results could provide valuable information about the force interactions when those multi-layer polymer films are immersed in water. And in this section, we will mainly discuss the surface forces results based on multi-layer polymer films obtained under three different configurations in 1 mM NaCl: PEI *vs.* PEI, PPFPA-*b*-PS *vs.* PPFPA-*b*-PS, PEI *vs.* PPFPA-*b*-PS.

a) PEI *vs.* PEI

Initially, the force-distance results are measured by approaching and separating two multi-layer polymer films (PEI as the top layer) in a SFA 2000 system. As shown in Figure 5.9, there is no attractive force between the multi-layer polymeric surfaces during approaching, which indicates that the repulsive forces between the two surfaces are predominant. The measured repulsion range is ~ 35 nm, which is larger than the the peak-valley value obtained using AFM imaging (~20 nm in Figure 5.8f). This repulsion should be due to the combination of steric repulsion between swelled PEI chains and repulsive electric-double-layer forces between two surface with similar charges. Besides that, slightly adhesion with a magnitude of 3-4 mN/m is measured during separation. The interaction acting between two polymer-coated surfaces mainly comes from several parts: the DLVO forces that contain both vdW force and double-layer force; polymer induced forces which include polymer bridging attraction and steric repulsion; elastic repulsive force due to surface asperities. An early research that have studied the adsorption behavior of highly branched PEI on smooth mica surface found that at low ionic strength, the electrostatic force will predominate while at higher ionic strength, the conformation of the PEI layers changes into a more compact configuration.[205] Thus the pure repulsion we have measured could be mainly attributed to electrostatic repulsion between two similar charged PEI layers. While the adhesion during separation is mainly because of vdW force and bridging effect between adsorbed PEI molecule since a large stretch behavior is observed. Another point is that the magnitude of adhesion we measured (<5 mN/m) is lower than that reported by Claesson *et al.*. The smaller adhesion could be due to lower adsorption amount and different configurations of PEI on mica surface.[205]

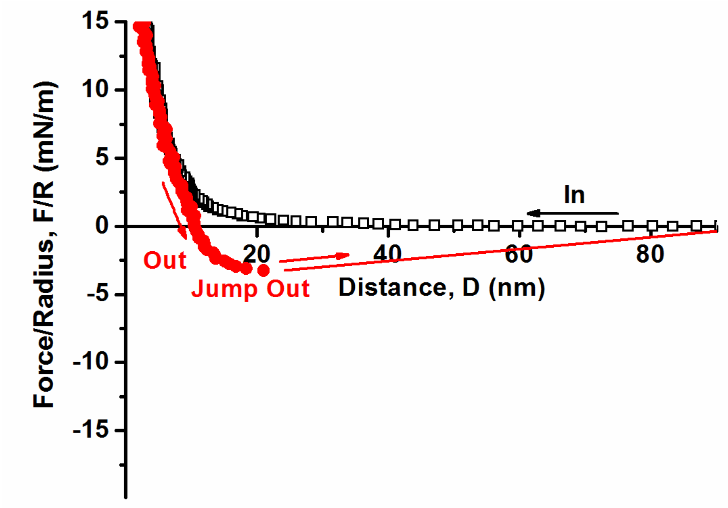

Figure 5.9 Force-distance profile of PEI surface *vs.* PEI surface in 1mM NaCl solution.

b) PPFPA-*b*-PS *vs.* PPFPA-*b*-PS

Figure 5.10 shows the force-distance profile between two multi-layer polymer films with PPFPA-*b*-PS polymer layer on top. Although the contact angle of these surfaces reach 90 degree, unlike the force-distance results mentioned in Chapter 4 where long range attractive force it is observed, only pure repulsion with relatively long range (~ 60 nm) is measured during approaching. An adhesion (~ 16 mN/m) is measured during separation, which is one magnitude lower than the adhesion value measured between two smooth PPFPA-*b*-PS surfaces (~ 280 mN/m). The pure repulsion during approaching and the reduced adhesion when separating the two surfaces might be related to the increasing of surface roughness which would affect the amount of bubbles on polymer surface and the effective-contact area. We also noticed that further increasing the number of bi-layers (e.g., > 5 bi-layers) will result in double-contact during SFA measurement, which leads a very long range steric force (> 100 nm) during both approaching and separation.

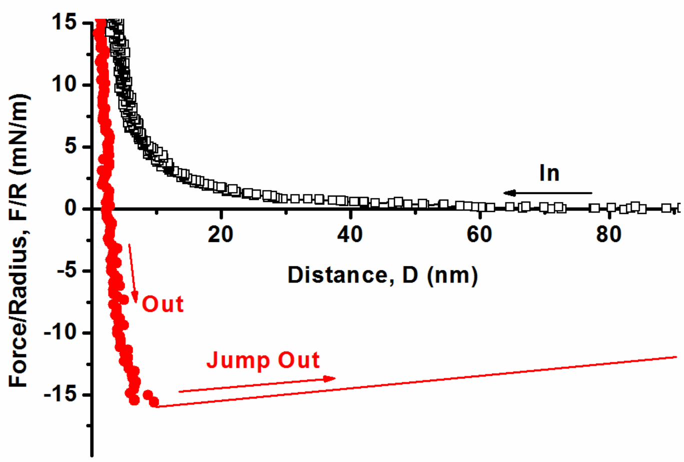

Figure 5.10 Force distance profile of PPFPA-*b*-PS *vs.* PPFPA-*b*-PS surface in 1mM NaCl solution with a symmetric configuration.

b) PEI *vs.* PPFPA-*b*-PS

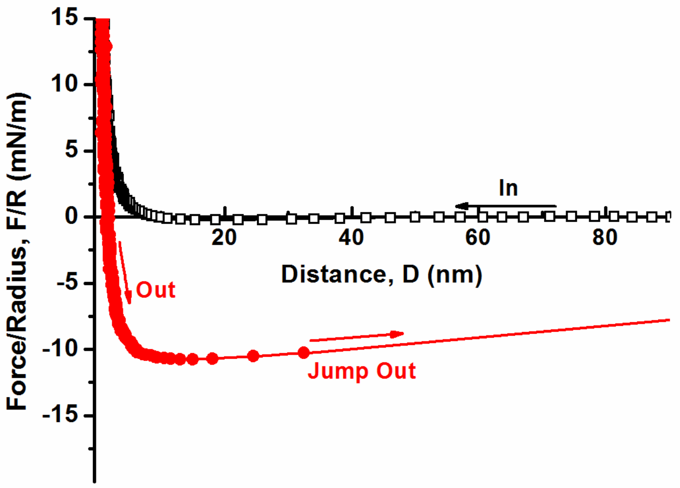

Figure 5.11 Force distance profile of PEI surface *vs.* PPFPA-*b*-PS surface in 1mM NaCl solution under an asymmetric configuration.

In previous sections, we mainly talked about the force results obtained under symmetric configurations, and here we also conducted force measurement between multi-layer polymer films under asymmetric configurations, *viz.*, PEI *vs.* PPFPA-*b*-PS surface under aqueous solutions. Figure 5.11 shows the force-distance profile between two PEI & PPFPA-*b*-PS polymer film with one surface to be PEI on the top, the other surface to be PPFPA-*b*-PS on the top. It is observed that the force-distance profile shows an inward curve around 40 nm during approaching, suggesting a slight attractive force was measured during approaching. This attractive force could be mainly due to the electrostatic interaction between opposite charged polymer surfaces. More importantly, a large strength with a length of around 35 nm is observed during separation, which is a typical bridging behavior of polymers during force measurement.

Overall speaking, the surface forces acting between two polymer-coated surfaces in 1mM NaCl mainly come from three parts: the DLVO forces that contain both vdW force and double-layer force; polymer induced forces which include polymer bridging attraction and steric repulsion; elastic repulsive force due to surface asperities. The above force results demonstrate that surface charges could play dominant roles for surface interaction of PEI&PPFPA-*b*-PS multi-layer films in aqueous solutions. The SFA results based on active ester surface and amine could provide fundamental insights into the adsorption and interaction of LbL deposited films.

5.3.9 Post-treatment of LbL Assembling Films

a) Freestanding polymer films

Stability test suggest that the multi-layer polymer film could become free-standing in either strong acid or base solution. Inspired by this result, we hypothesized that the freestanding polymer film would preserve excellent integrity due to the strong covalent bonding. Further experiment results do proved our hypothesis: the multi-layer polymer film could be peeled off from the substrate without rupture or using any sacrifice layer, which is shown in detail in Figure 5.12, where freestanding film with different thickness and shapes was obtained.

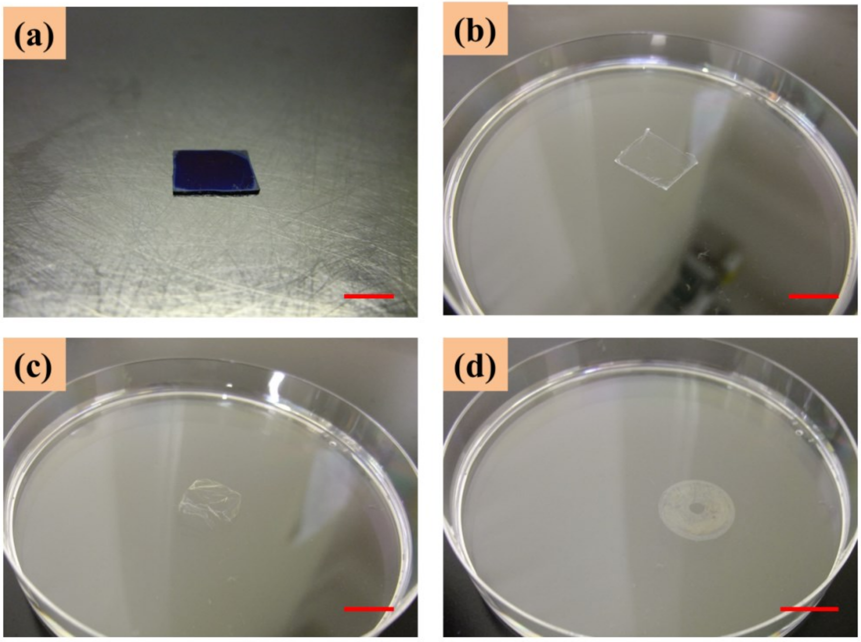

Figure 5.12 (a) as prepared multi-layer polymer film on silica surface, the blue color is due to the interference of visible light, (b) freestanding multi-layer polymeric film (6 bi-layers) with perfect integrity, (c) thin freestanding film with single bi-layer, (d) freestanding multi-layer polymeric film with circle shape.

Scanning Electron Microscope imaging and element mapping have been employed to understand the morphology and element composition of the polymer film on silicon surface. Figure 5.13 shows the morphology of partially peeled multi-layer polymer film on silicon wafer. The element mapping results of carbon suggest that polymer film at the top corner has been peeled off, and the folded part shows stronger carbon signal. Due to the high penetration depth of electron beams (~ tens of μm), the strong signal of substrate (Si) is also observed.

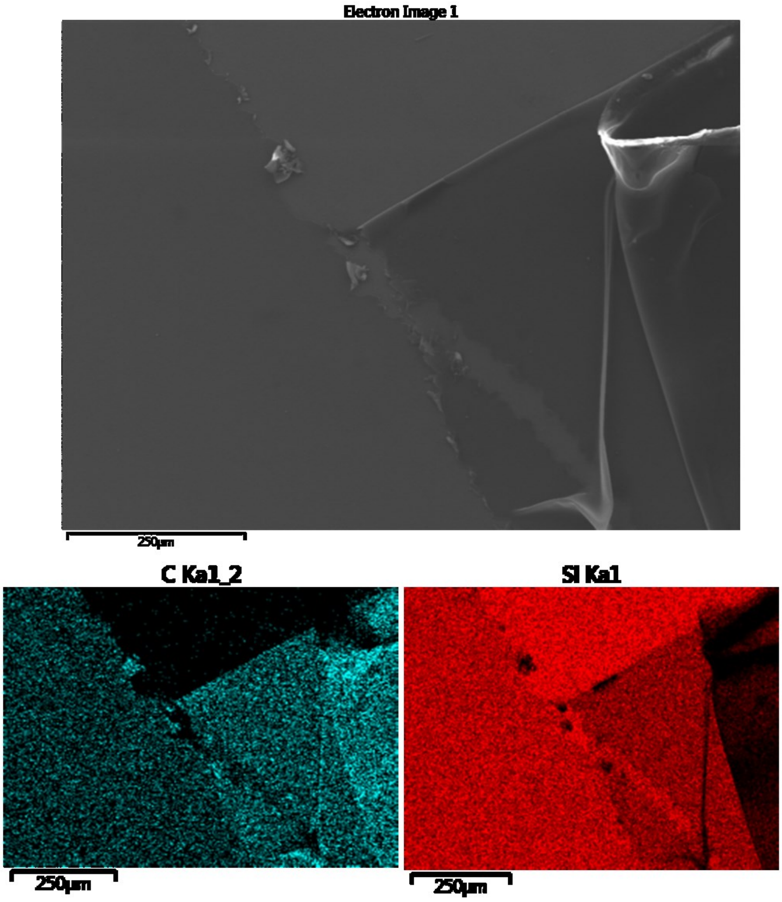

Figure 5.13 Scanning electron microscope image and related element mapping results of partially peeled polymer film. The bottom figure shows the distribution of carbon (left) and silicon (right) on this specific area.

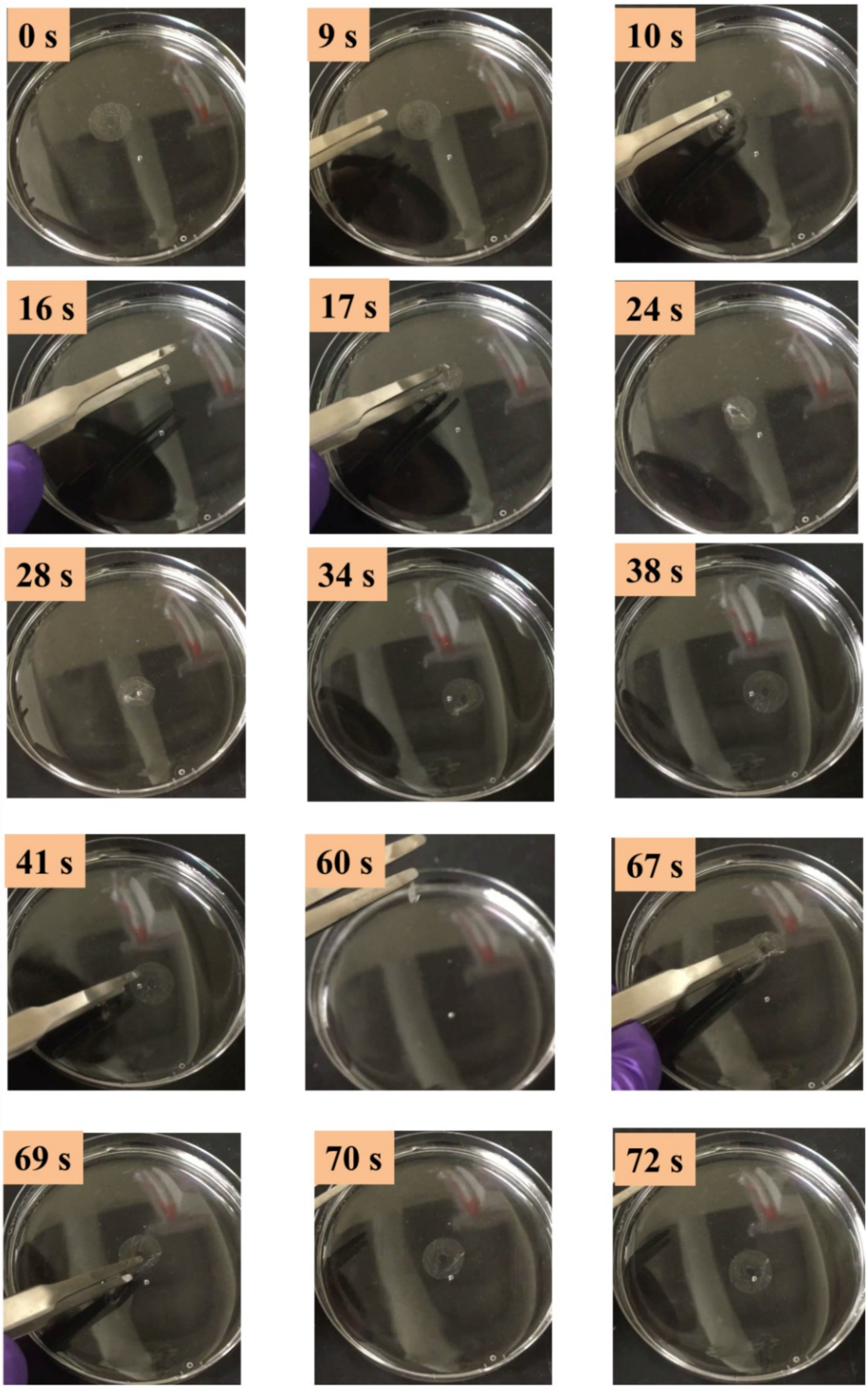

Figure 5.14 Folding and unfolding of freestanding PEI&PPFPA-*b*-PS multilayer films in water for two cycles.

Additionally, we also tested the mechanic strength of the freestanding multi-layer thin film using a qualitative method, by simply folding and unfolding the film using a tweezer (Figure 5.14). It is noting that the film is quite strong and shows an amazing ability to folding and unfolding for multiple times (N>10), it seems that the strong covalent bonding network between the multilayer polymers and the specific hydrophobicity helps to keep the integrity of the free-standing film. The unique stability and mechanic strength of the film could be further employed to various areas such as transparent electronics, protective coatings, drug release and *etc*.

b) Fluorination

XPS and FTIR results shows that there are both free amine and free active ester inside the polymer, which suggest that the as obtained polymer films could be further functionalized with other compounds. As a demon of concept, we immersed the prepared film into Perfluorooctanoic acid (PFOA, a typical perfluoro-carboxylic acid) for 1 h. As shown in Figure 5.15, surface hydrophobicity increases from 90^o to around 125^o after treating with PFOA solution. The cross-section SEM image of the multi-layer polymeric film clearly shows layered structure for this modified polymer film. The increasing of surface hydrophobicity demonstrates that those free amine could be further modified to prepare multifunctional surfaces.

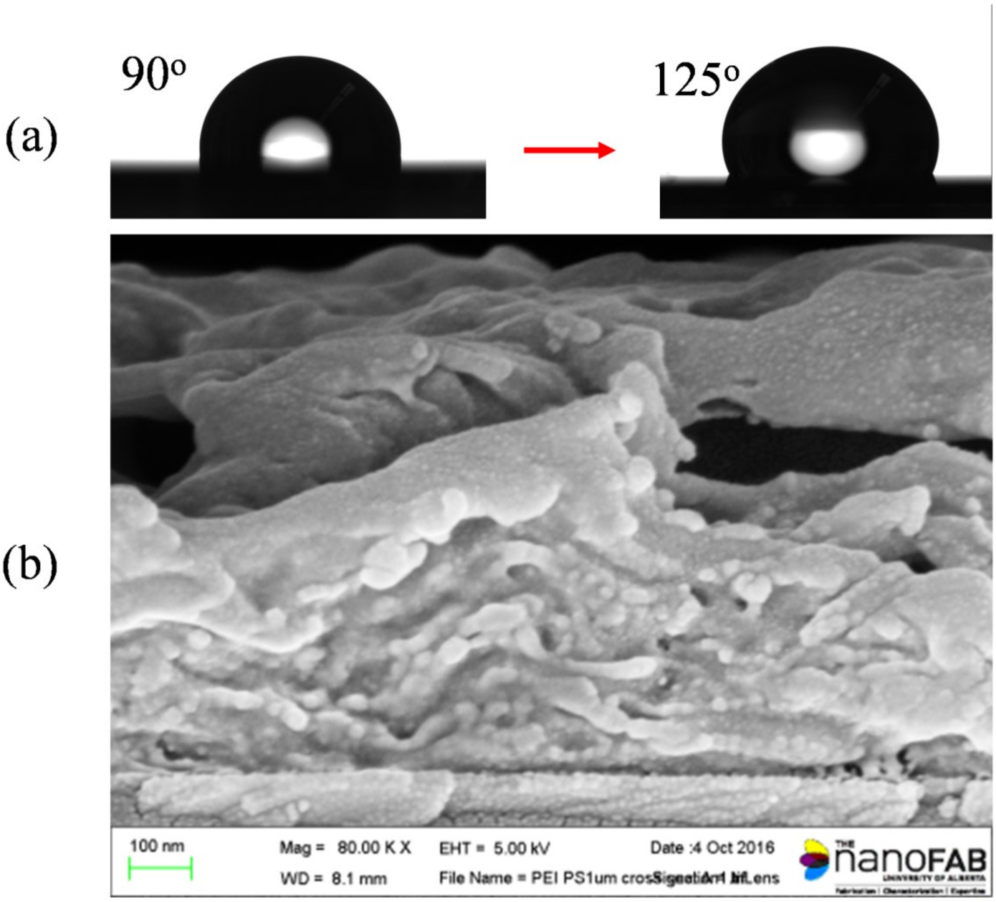

Figure 5.15 (a) Water contact angle images of (PEI&PPFPA-*b*-PS)$_6$ film before (left) and after (after) treating with perfluoro caprylic acid solution. b) Cross-section SEM structure of fluorinated (PEI&PPFPA-*b*-PS)$_6$, which shows typical layered structure.

5.4 Conclusion

In this chapter, a new type of covalent bonded multi-layer polymer surfaces was achieved by forming amido bond between poly(pentafluorophenylacrylate)-*b*-polystyrene polymer with primary amine (highly branched PEI) using spin-assisted LbL deposition. This functional coating could be applied to a series of substrate including mica, silicon and glass slide and shows switched hydrophobicity by alternated deposition of PEI (hydrophilic) and PPFPA-*b*-PS (hydrophobic). SFA measurements based on three different configurations including PEI *vs.* PEI, PPFPA-*b*-PS *vs.* PPFPA-*b*-PS, and PEI *vs.* PPFPA-*b*-PS. Strong adhesion between PEI layer and PPFPA-*b*-PS layer with significant stretching behavior was observed between PEI and PPFPA w layers, the force results provide further information on the interaction between PEI and PPFPA-*b*-PS layers from molecular scale.

Post treatment of multi-layer polymer films by immersing those films in different solutions suggest that this multi-layer film has very good stability in organic solvent or low salt aqueous solution, but could become freestanding after immersing in 1 M NaOH or 1 M HCl. On the other hand, by immersing the multi-layer polymer film in perfluoro caprylic acid, those excessive amines could further react with carboxyl groups and producing surfaces with higher hydrophobicity (water contact angle to be 125^o), and this film demonstrate great potential for preparing superhydrophobic surface in the future. Our research here shows a versatile route for preparing multi-functional surfaces based on active ester and amines using spin LbL deposition.

CHAPTER 6

UNDERSTANDING THE NANOMECHANICS OF MUSSEL-INSPIRED POLY(CATECHOLAMINE) COATINGS IN AQUEOUS SOLUTIONS

6.1 Introduction

It is well known that most glues do not work well in aqueous environment because water molecules or water layer could hinder the formation of adhesive bonds on the surface or cohesive bonds within the bulk phase.[18,206] Achieving strong underwater adhesion is of great significance for biotechnological applications such as drug delivery and tissue engineering in the human body, where water is ubiquitous. Mussels could secrete protein-based underwater adhesive materials that facilitate the attachment of mussel threads to almost all types of surfaces in marine environments and achieve strong underwater adhesion.[207] *L*-3,4-dihydroxy-phenylalanine (*L*-DOPA), a unique amino acid with additional amine group to be the side chain (Figure 6.1a), *i.e.,* catecholamine structure, is widely found in the protein-based adhesive materials of mussels threads.[60] Dopamine (DA) is a small molecule that mimics the adhesive component *L*-DOPA in marine mussels, and it has similar catecholamine structure like *L*-DOPA, which is shown in Figure 6.1b.[61] In 2007, Lee *et al.* first reported that DA has the capability to self-polymerize and form polydopamine (pDA) films on virtually any solid interfaces from metal oxides, ceramics to polymers.[19] Since then, mussel-inspired poly(catecholamine) coatings have rapidly been emerged as a toolkit for controlling surface properties for tissue engineering,[208] cell attachment,[209] drug delivery, [210] sensors,[211] microfluidic devices,[212,213] Li-ion batteries,[214] and so on.

One of the big challenges for using dopamine as coating material is that the surface roughness and morphology of DA treated surface is usually difficult to control due to the complexity in oxidation chemistry of catecholamine. Aggregates can easily grow both from surface or solution by polymerization, which generally results in uneven coatings on the surface.[19] Uncontrolled polymerization of catecholamine results in undefined assembled nano-aggregates presented at interface when measuring surface interactions, which will adds up to the difficulty of understanding the mechanism for underwater adhesion. In order to solve this problem, other chemicals that contain catecholamine groups with the ability to generate smooth coatings are developed. Norepinephrine (NE) is one of the catecholamine neurotransmitters (Figure 6.1c) that could self-polymerization to form surface coatings on variety of surfaces. NE is of great biological significance because it is working as a neurohormone and neurotransmitter for controlling responsiveness to stress and fear in human body.[70, 215] Unlike pDA surfaces, the poly-norepinephrine (pNE) surfaces can achieve almost perfect smoothness at the nanometer scale, which provides a suitable platform that allows a variety of experiments such as accurate surface interaction measurement to be feasible. [16]

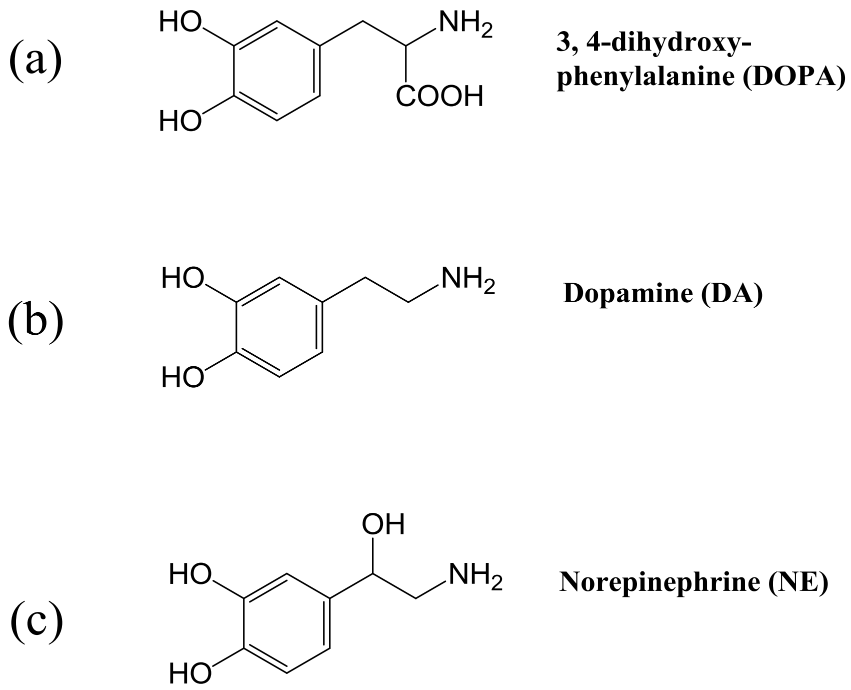

Figure 6.1 Chemical Structure of (a) *L*-3, 4-dihydroxy-phenylalanine (*L*-DOPA), (b) dopamine (DA), (c) norepinephrine (NE).

In adhesion mechanism of poly(catecholamine) onto different substrates, the two functional moieties, catechol and amine, are reported to have a synergistic interplay in wet adhesion and substrate-independent coating ability.[77] The adhesion mechanism of catechol has been relatively well studied by previous studies utilizing Atomic Force Microscopy (AFM) and Surface Forces Apparatus (SFA). The AFM force measurements of a single DOPA residue contacting a wet titanium oxide surface reveal a reversible and high strength non-covalent interaction with a force magnitude between 0.7 and 0.8 nN by a coordination mechanism instead of hydrogen bond during separation. And the oxidation of DOPA groups will result in decreasing of adhesive strength on metal oxide surface but irreversible covalent bond with the force strength increase up to 2 nN due to the breaking of covalent bonds for amine presenting organic surface.[71] On the other hand, the research based on mussel foot protein (mfp) using the SFA technique shows that the adhesion between mussel proteins largely depends on factors that could influence the DOPA redox or chelation such as pH or substrate. And it is reported that the adhesion between two mfp-3 protein films at pH 5.5 and pH 7.5 could be reduced by ~80% and ~95% as compared to the value at pH 3 due to the oxidation of DOPA to dopaquinone. [216,217] At mean time, the SFA technique also reveals that the chelation between catechol groups and divalent and trivalent cations such as Ca^{2+} or Fe^{3+} that can induce considerable adhesion of non-adhering mfps such as mfp-2 and mfp-1. Overall, the adhesion could be influence by various factors such as the type of protein tested, the surface chemistry, the contact time, the oxidation state of DOPA groups and the type of metal ions in the environment.[74, 75,76]

Despite the importance of amines in material-independent surface chemistry, investigating the adhesion force of catechol and amine at an interface remains to be a challenge due to the complex DOPA redox chemistry and uncontrolled surface morphology for pDA. A study aiming at cooperative adhesion mechanisms of catechol and amine together is essential and has not been reported yet. Therefore, in this chapter, we measured the interaction forces with or without amine systematically by utilizing NE (a model catecholamine compound) instead of DA and pyrocatechol (PC, a typical catechol compound without amine) in a SFA system so as to explicate the role of primary amines in the strong adhesion of catecholamine materials. The challenges such as uncontrolled polymerization and formation of nanoparticles at interfaces are solved by controlled polymerization of pNE. Our results indicate that the adhesive strength between poly(catecholamine) layers measured by SFA is 30 times higher than that of a poly(catechol) coating without any amine moiety at the same polymerization time. This result implies that the contribution of the primary amine group to the catecholamine coating is a vital factor in the design and development of mussel-inspired catechol-based coating materials.

6.2 Materials and Experimental Section

Dopamine hydrochloride (DA), Pyrocatechol (PC), DL-norepinephrine hydrochloride (NE), sodium phosphate monobasic (NaH_2PO_4, ReagentPlus), sodium phosphate dibasic (Na_2HPO_4, ReagentPlus), ammonium hydroxide ($NH_3 \cdot H_2O$, 28 wt%), hydrochloric acid (HCl) and sodium hydroxide (NaOH) were purchased from Sigma-Aldrich and used as received. Mill-Q water was used to prepare aqueous solutions. Phosphate buffer solution (PBS) was prepared by mixing sodium phosphate dibasic and sodium phosphate monobasic at certain ratio and dissolved in Mill-Q water, then adjusted the pH to 8.4 using 0.1 M HCl or 0.1 M NaOH.

Preparation of pDA, pNE, pPC coated surface

The polydopamine (pDA) coated surface was prepared by immersing fresh cleaved mica surface into 2 mg / ml dopamine hydrochloride solution made from 10 ml ethanol, 20 ml water, stirring for 1 min, 0.15 ml of ammonium hydroxide are added to adjust the pH to 8.5. Oxygen from air will initiate the polymerization process, the solution become brown and finally dark after polymerization for 12 h. The coated mica substrates were washed with deionized water and dried using nitrogen gas afterwards.

The poly-norepinephrine (pNE) coated surface was prepared by immersing fresh cleaved mica surface for 24 h at room temperature in 2 mg / ml NE solution, which was prepared by dissolving DL-norepinephrine hydrochloride in 10 mM PBS buffer (pH 8.4) at 2 mg/ml. The polymerization process was triggered by dissolved oxygen. Finally the solution turned into deep dark and the mica substrates were washed with deionized water and dried using nitrogen gas.

The poly-pyrocathcol (pPC) coated surface was prepared using the similar procedure except for dissolving pyrocatechol (PC) in 10 mM PBS buffer (pH 8.4) at 2 mg / ml. The coated substrates were washed with deionized water and dried using nitrogen gas.

Element composition of the pNE and pPC coating was characterized by X-ray Photoelectron Spectroscopy (XPS, K-alpha, Thermo VG Scientific, USA) and Secondary Ion Mass Spectroscopy (SIMS) measurement. The surface morphology of the coated substrates was measured by Atomic Force Microscope (AFM, Bruker Icon, USA and MFP-3D, Asylum, USA).

Nanomechanical measurement using Surface Forces Apparatus

An SFA 2000 (SurForce LLC, Santa Barbara, CA, USA) system was used to measure the nanomechanical properties of polymerized NE and PC in aqueous solutions. Back-silvered muscovite mica surfaces (S&J Trading, NY, USA) were glued onto cylindrical glass disks using an epoxy glue (EPON 1004, Exxon Chemicals, USA) with the thickness of silver to be ~ 50 nm. After that, the two disks were mounted into the SFA chamber in a cross-cylinder configuration. For the in situ polymerization experiment, the NE or PC solutions were then prepared using the same method as described in surface characterization part. Then a droplet of ~70 μL NE or PC solution was directly injected into the two opposing mica surfaces for polymerization, and the SFA chamber was saturated with water vapor to reduce the evaporation rate of water. The film thickness and absolute separation distance were obtained in situ by employing an optical technique named Multiple Beam Interferometry (MBI) using the Fringes of Equal Chromatic Order (FECO). [24] The measured force, F, between two curved surfaces, was correlated to the interaction energy per unit area ($W(D)$) of two planar surfaces using the Derjaguin approximation (Equation 6.1) [1]

$$F(D) = 2\pi R W(D) \tag{6.1}$$

The interactions between the two pNE layers and two pPC layers were measured at an interval of ~30 min at room temperature.

6.3 Results and Discussion

6.3.1 Morphology of Polycatecholamine Coatings and Pyrocatechol Coatings

Poly(dopamine) is a candidate polymer for determining the effect of amine groups on the adhesion mechanism of polycatecholamine coatings. Thus the polydopamine coating experiment on fresh mica surface was conduct first. Figure 6.2 shows the typical morphology of pDA surface obtained *via* tapping mode AFM imaging. After polymerization for 10 h, scattered particles are observed on mica surface (Figure 6.2a). The surface root-mean-square (RMS) roughness is measured to be 5.6 nm. Compared to fresh cleaved mica surface with a RMS roughness less than 0.2 nm, the pDA surface roughness increases for one order of magnitude. The cross-section height profile shown in Figure 6.2b suggests that those tiny particles are unevenly distributed with a maximum height of ~ 40 nm and lateral dimension of ~ 100 - 600 nm.

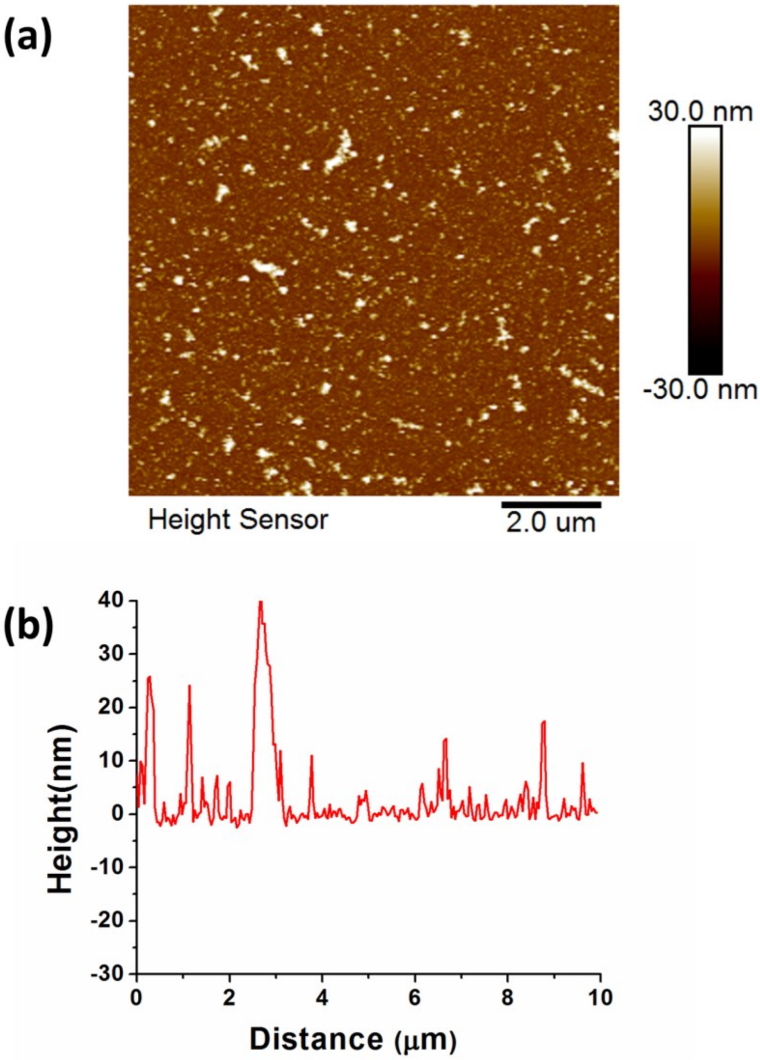

Figure 6.2 (a) Topography AFM image of dopamine after polymerization for 10 h on fresh cleaved mica surface (10 μm × 10 μm), (b) cross-section line scan profile of (a).

In order to confirm the fully coverage of pDA, high resolution AFM scan has been conducted on those area without large particles, and related AFM images and height section profile are shown in Figure 6.3. It is clearly observed that the whole image is covered by pDA aggregates with the height variation of 5-25 nm and their lateral dimension was ranged from tens of nanometers to hundreds of nanometers. The AFM images shown in Figure 6.2 and Figure 6.3 are consistent with previous reported result that uncontrolled polymerization of dopamine generally resulted in undefined assembled nano-aggregates at interface due to the complexity in oxidation chemistry. Because of unavoidable steric force induced by large particles during approaching, the rough pDA surface is not a good platform for conducting nano-mechanical techniques such as SFA.

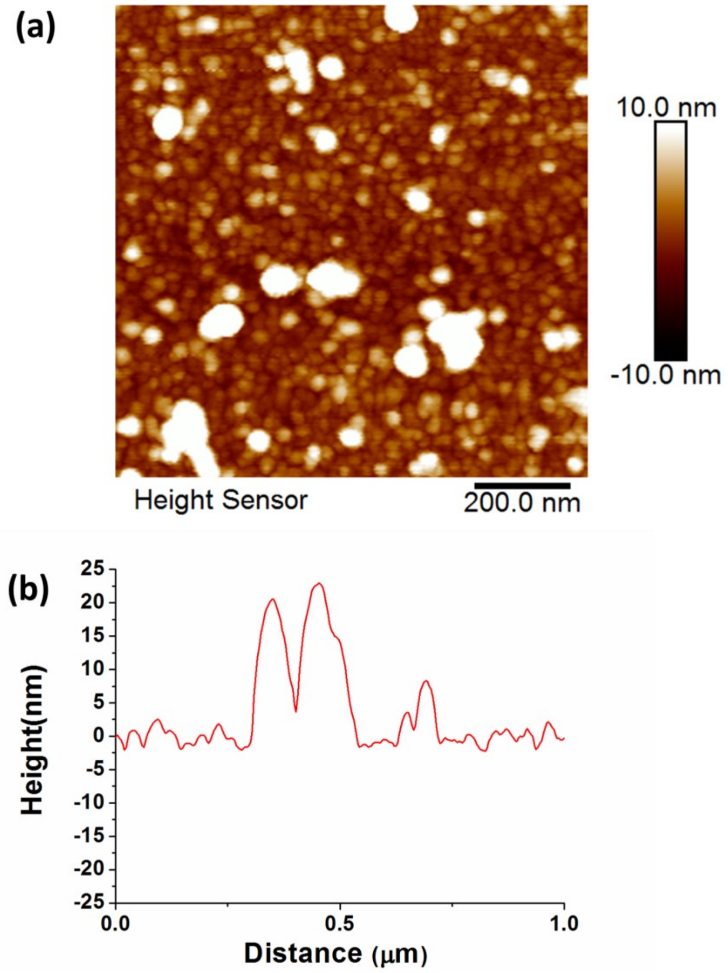

Figure 6.3 (a) Topography AFM image of dopamine after polymerization for 10 h on fresh cleaved mica surface, scan size to be 1 μm × 1 μm, (b) typical cross-section height profile of (a).

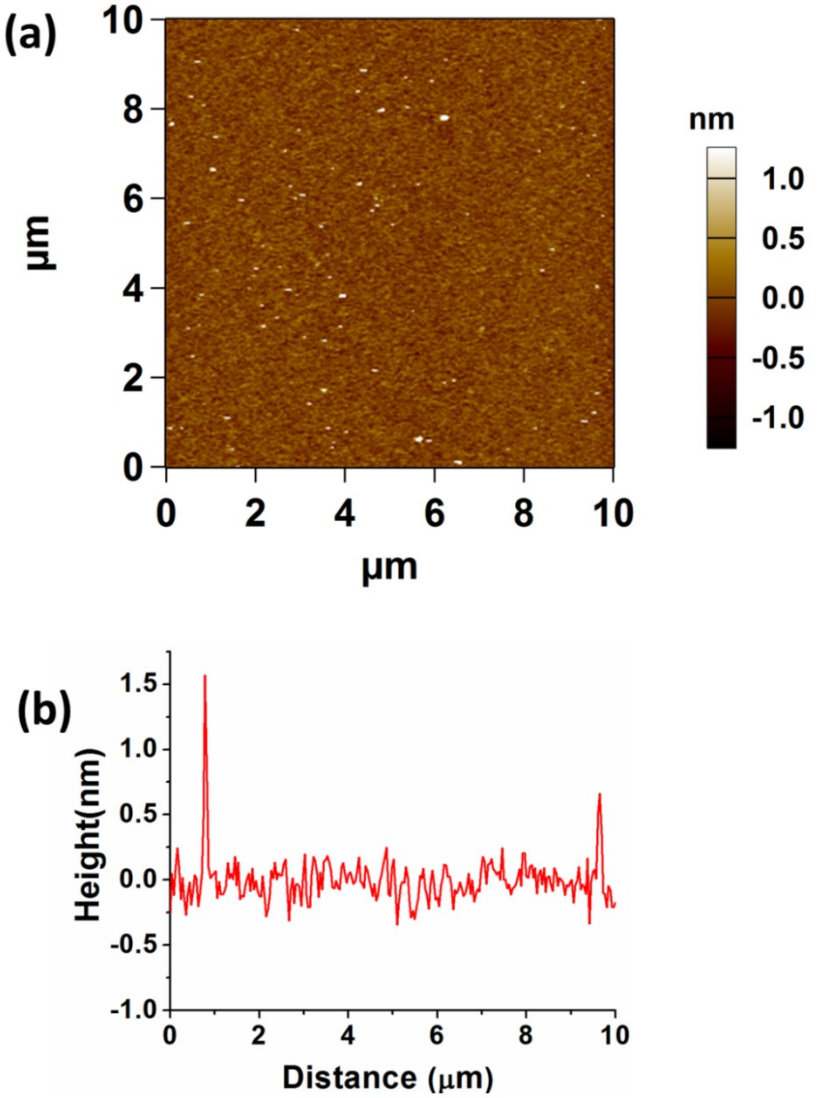

Figure 6.4 (a) Topography AFM image of norepinephrine (NE) after polymerization for 24 h on fresh cleaved mica surface, (10 μm × 10 μm) (b) cross-section line scan profile of (a).

In order to achieve smooth polycatecholmaine coatings, we change DA into NE for polymerization. Figure 6.4 shows the topography AFM image of pNE coatings with a polymerization time of 24 h. Still some scattered particles are observed on mica surface. However, the line scan profile shown in Figure 6.4b suggests that the heights of those nanoparticles are less than 2 nm with the lateral dimension to be less than 20 nm. The measured height and size of those particles are much smaller as compared to pDA surface shown in Figure 6.2. The surface root-mean-square (RMS) roughness was measured to be only 0.6 nm, which is one magnitude lower than pDA surface with the same scan size.

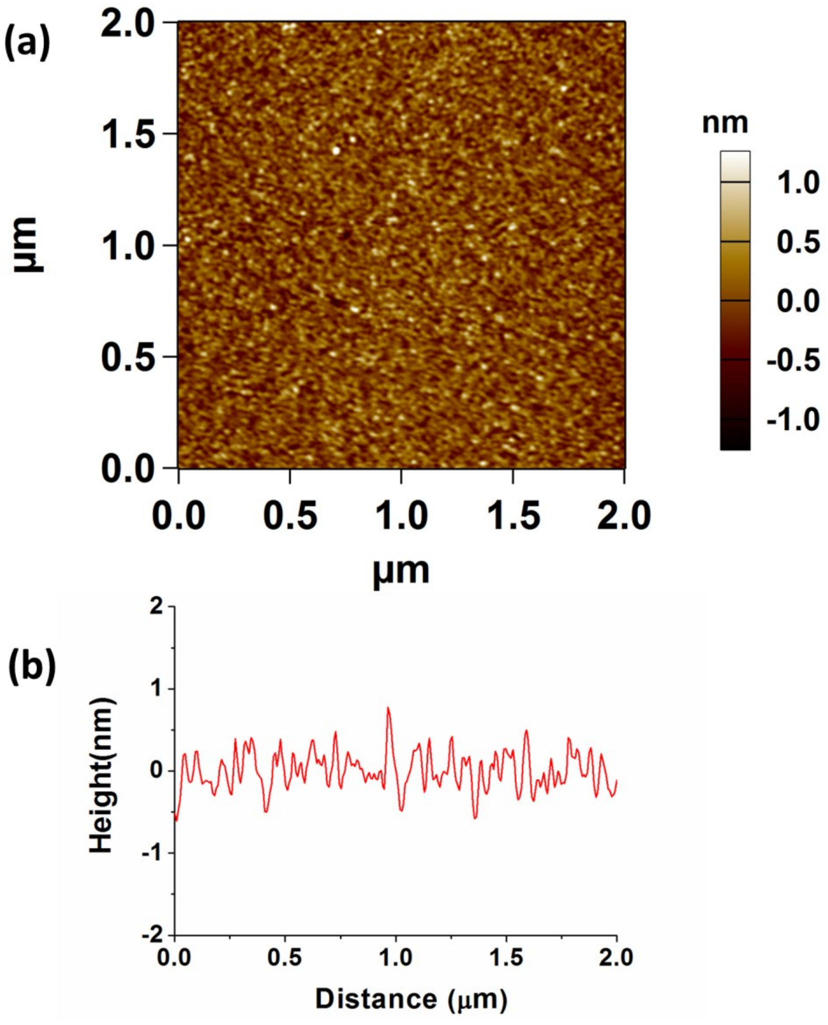

Figure 6.5 (a) Topography AFM image of norepinephrine (NE) after polymerization for 24 h on fresh cleaved mica surface (2 µm × 2 µm), (b) cross-section line scan profile of (a).

Figure 6.5 shows the higher resolution AFM image with a scan size to be 2 μm × 2 μm. Compared to pDA coatings, the fine scan of pNE shows much lower height fluctuation (ca 1.5 nm) and lower surface roughness (~ 0.4 nm). The AFM result shown in Figure 6.4 and Figure 6.5 proves that the pNE surface could achieve nearly perfect smoothness at the nanometer scale, which makes the measurement of the interaction forces between catechol and amine feasible by using the SFA technique. Therefore, by utilizing NE, we can explicate the role of primary amines in the strong adhesion of catechol-based materials.

As a control, the surface morphology of poly(pyrocatechol) (pPC), a self-polymerized catechol without any amine moiety, was also characterized using AFM technique operated in tapping mode. Related AFM images are shown in details in Figure 6.6 (5 μm × 5 μm) and Figure 6.7 (1 μm × 1 μm). Uneven coating with scattered of aggregates is observed on pPC coated mica surfaces (Figure 6.6a). According the the section profile shown in Figure 6.6b, the height of the particles on the surface is ~ 0.2 - 2.5 nm, and their lateral dimension could reach hundreds of nanometers. The detailed fine scan shown in Figure 6.7 further proves that the relatively smooth area are also covered with small particles with the maximum height fluctuation less than 1.5 nm, and the lateral dimension of the particles ranges from tens of nanometers to hundreds of nanometers. The RMS surface roughness of pPC surface is less than 0.5 nm, which is also suitable for measuring surface forces using the SFA technique.

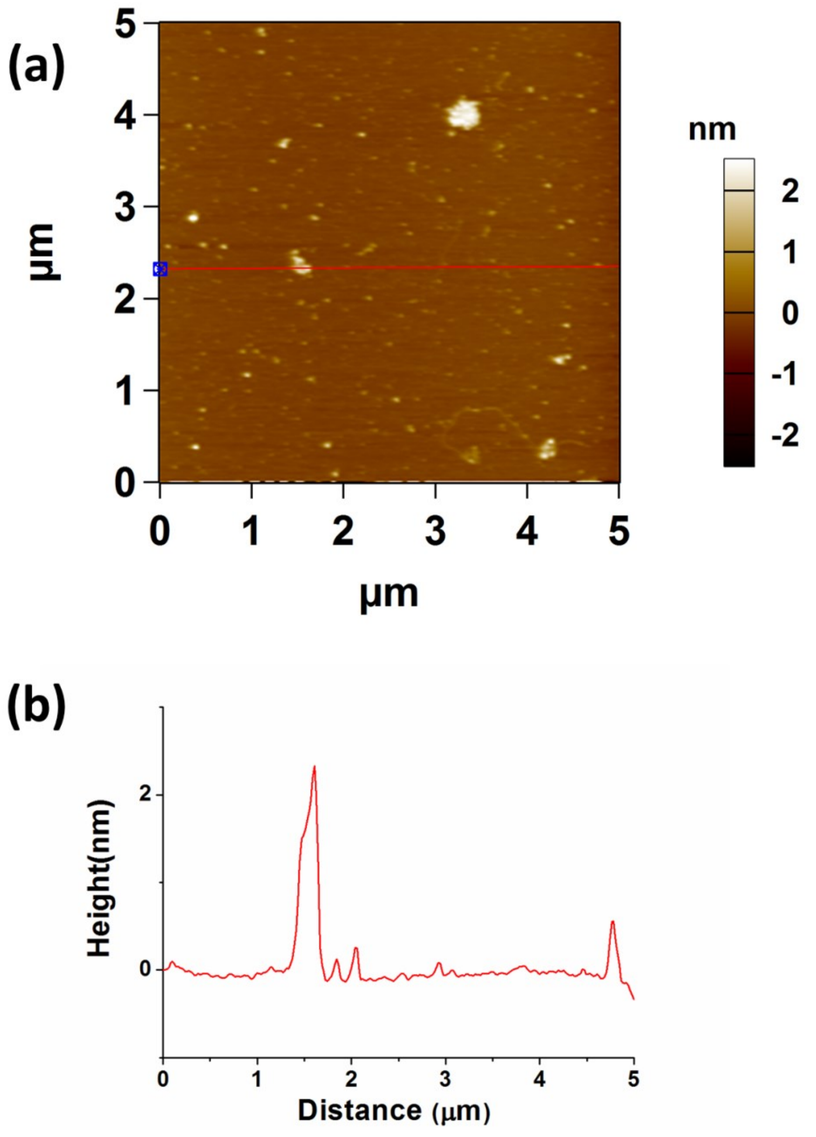

Figure 6.6 (a) Topography AFM image of pyrocatechol (PC) after polymerization for 24 h on fresh cleaved mica surface (5 µm × 5 µm), (b) typical cross-section-line scan profile of (a).

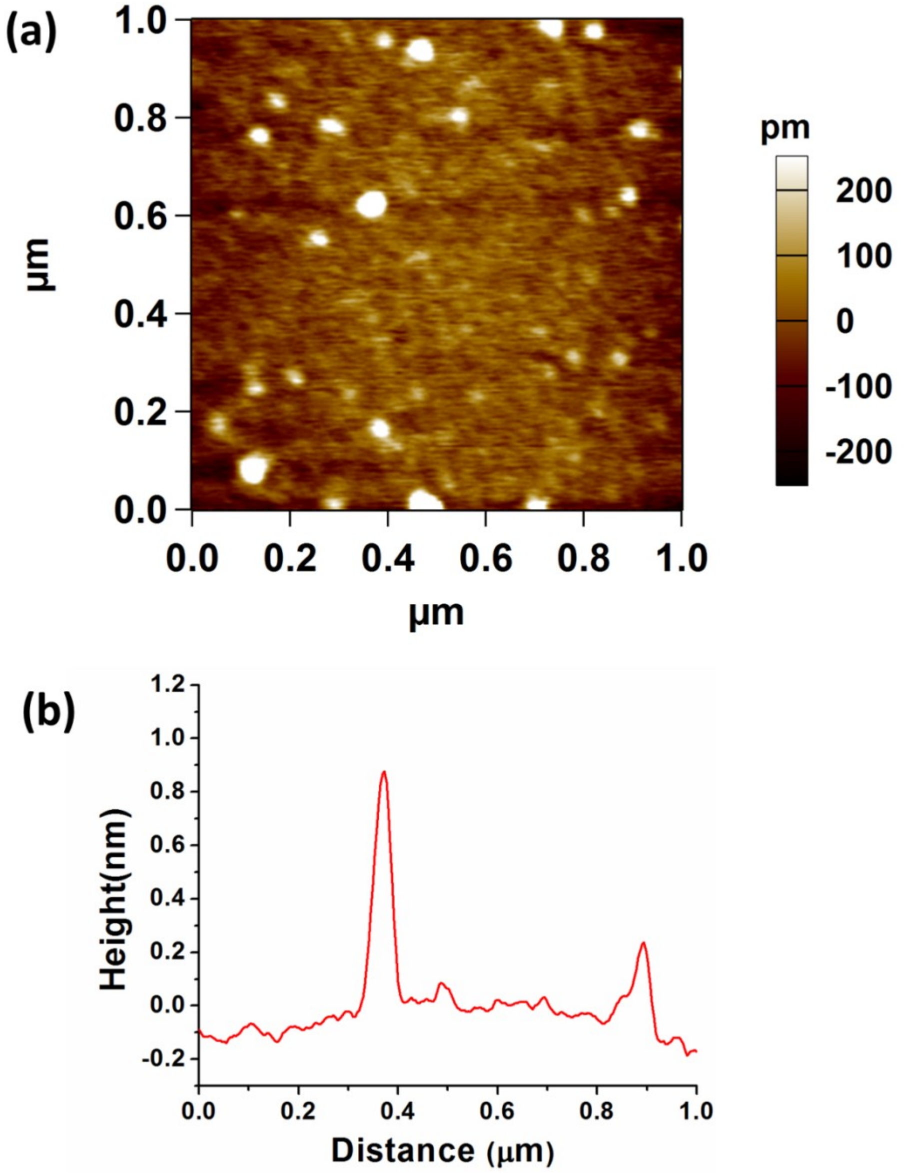

Figure 6.7 (a) Fine scan topography AFM image of pyrocatechol (PC) after polymerization for 24 h on fresh cleaved mica surface (1 µm × 1 µm), (b) typical cross-section-line scan profile of (a).

Above Topographic AFM images show that the pDA surface is composed of sphere particles with a relatively higher RMS roughness value (~ 5.6 nm), which is not suitable for measuring surface force using SFA technique. However, thin layers of both pNE and pPC films coated on mica substrates were achieved, and pNE provides a denser coating than pPC on mica. The AFM images also demonstrate that the primary amine groups could also facilitate the film deposition and should not be overlooked when coat a surface based on catechol chemistry. The smooth feature of pNE and pPC surfaces makes them suitable for measuring the influence of amine groups on surface forces. And the following discussion will be mainly focused on pNE an pPC coated polymer surfaces.

6.3.2 Chemical Composition of pNE and pPC Coatings

In order to confirm the element composition of pNE and pPC polymer surface, X-ray Photoelectron Spectroscopy is conducted. Figure 6.8a shows the XPS elemental survey spectrum of mica, and mica coated with pNE and pPC, respectively. The strong nitrogen peak of pNE implies that pNE successfully deposited on to the mica surface; however, pPC exhibited a similar survey spectrum to that of mica (no nitrogen peak), which was mainly because the pPC coating is very thin (< 10 nm) and the penetration depth of X-ray is larger than the thickness of pPC film. The coated pNE and pPC surfaces exhibited water contact angles of 30^{o} and 40^{o}, respectively, while mica is a superhydrophilic surface with a water contact angle around 0^{o}. The contact angle result also proves successful deposition of pNE and pPC coatings. The fine scan of C 1s spectrum was also conducted to verify the chemical state of carbon in the pNE and pPC coatings. Two features can be clearly observed. Firstly, as shown in Figure 6.8b, the intensity of C 1s peak follows the order of pNE > pPC > mica, suggesting pNE surface has the highest amount of organic coating which is consistent with previous AFM results, that there is dense polymer coating on pNE surface. Secondly, the C 1s peaks of pNE could be resolved into five different peaks regarding π-π* satellite peak, RO-C=O, R-C=O, C-O/C-N, and C-C/C-H, respectively, however the C 1s peak of pPC can be only resolved into two main peak regarding R-C=O and C-C/C-H. The XPS results here further confirms the presence of the coatings on mica surface after polymerization.

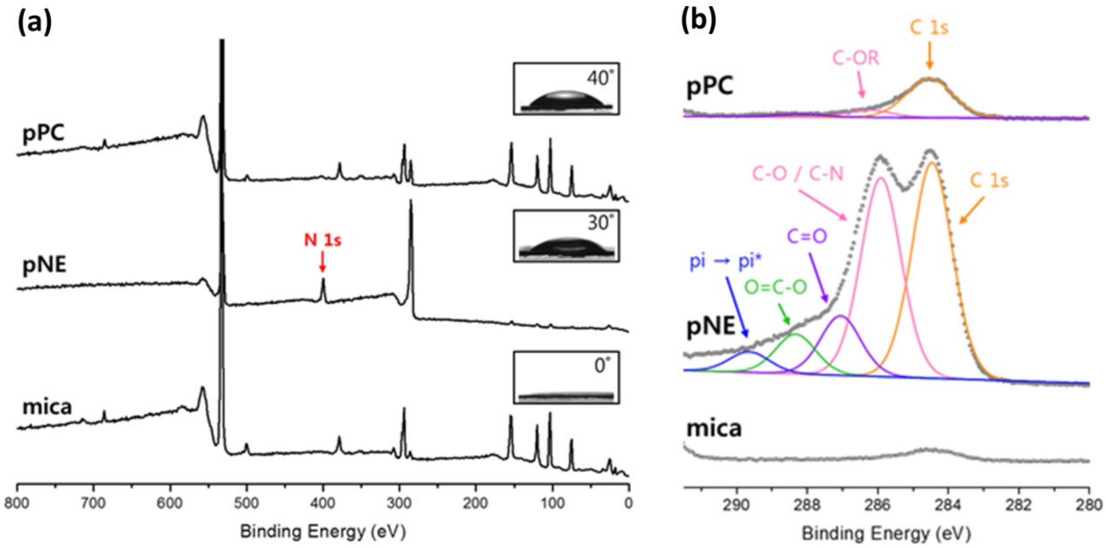

Figure 6.8 (a) XPS survey scan of mica, pNE and pPC surfaces, the insets shows the contact angle of each surface. (b) Fine scan of C 1s peak for mica, pNE and pPC surfaces, respectively.

The carbon 1s peak proves that pPC and mica shows similar spectrum but different amount of carbon. In order to check if the pPC surface are fully covered with pPC coating, Secondary Ion Mass Spectroscopy (SIMS) are also conducted to measure the element distribution of pPC coatings on mica surface. Fresh cleaved mica and pPC coated mica (24 h) are chosen for studying. Figure 6.9 shows the signal intensity of different fractions such as C_6-, SiO-, and AlO- collected under the same condition. Interestingly, the results suggest that after pPC coating, the signal intensity of AlO- and SiO- decrease obviously from 36700 to 10500 and 85500 to 48400, and the element distribution of C_6 is not distinguishable. Combining with the fine scan AFM results shown in Figure 6.7 and the element characterization results shown in Figure 6.8 and Figure 6.9, there is a thin layer of organic coating on pPC coated mica surface.

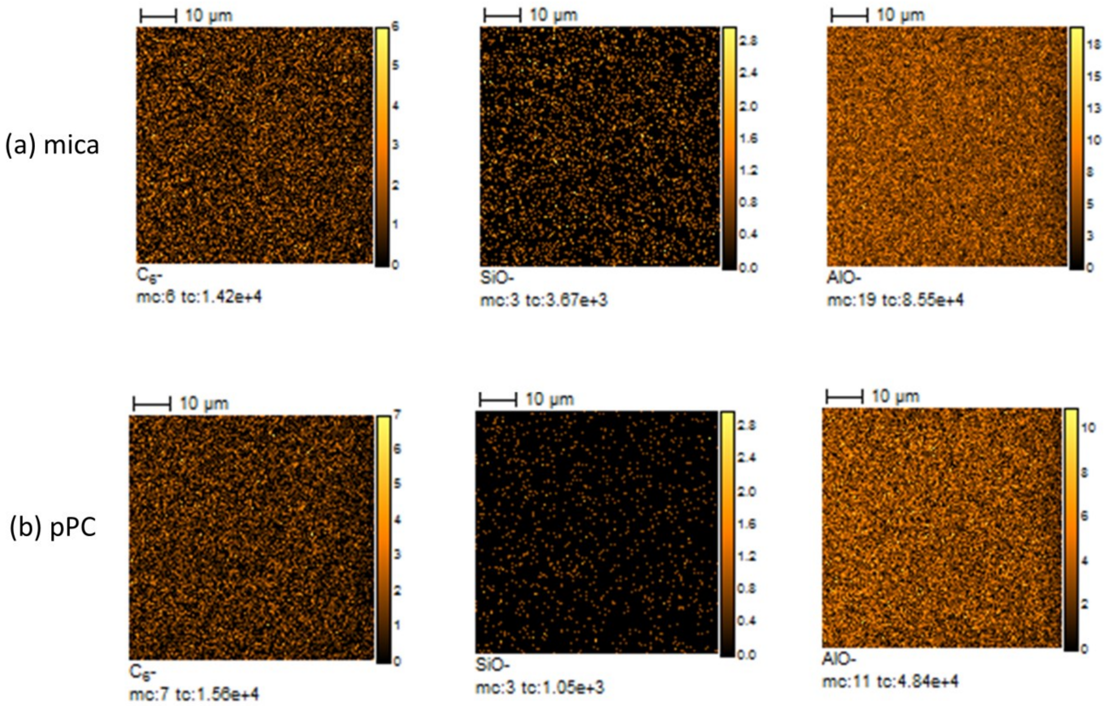

Figure 6.9 Secondary Ion Mass Spectroscopy (SIMS) result of mica (a), and pPC (b) surfaces, the figures from left to the right shows the signal intensity of of C6-, SiO-, AlO- fragments, respectively.

6.3.3 Deposition Mechanism of pDA, pNE, pPC on Mica

The successful deposition of poly-catecholamine materials depends on the polymerization process and the interaction between polymer and substrate. In this part the proposed deposition mechanism for those three catechol reagents, dopamine, norepinephrine and pyrocatechol will be described.

Firstly, we would like to discuss the polymerization process of dopamine (pDA) because it is the most well studied polycatechol material since the first report of its substrate-independent coating ability.[19] Generally, the basic chemical reactions during polymerization of dopamine include oxidation, cyclisation, reorganization, coupling, oxidative degradation and dismutation, which are shown in Figure 6.10.

The catechol group of dopamine is easily oxidized to quinone under an alkaline aqueous environment due to the presence of oxidizing agent such as oxygen, hydrogen peroxide, sodium periodate ($NaIO_4$), *etc.* Then the dopamine-quinone will cyclisation to another form named leukdopaminechrome, and then leukdopaminechrome can undergo further oxidation to dopaminechrome, then rearrange into an important intermediate named 5,6-dihydroxyindole (DHI), which acts as a monomer for subsequent polymerization.[218, 219] The DHI could easily get oxidized into Indole-quinone (IQ) form, and the dismutation of IQ and DHI will generate semi-quinone radicals.[220,221] Then dopamine polymerization progresses through a radical-induced intra-molecular cross-linking process.[63,222,223] Finally, polycatecholamine coatings on different substrates are formed with lots of particle could easily be observed (Figure 6.3). During the polymerization process, other factors such as π-π stacking,[90] van der Waals force,[1] hydrophobic interaction,[8] cation-π interactions,[224] co-ordination bonds,[71] chelating effect with metal ions,[74] hydrogen bonding,[90,218,] dynamic covalent bond[225] and quinhydrone charge-transfer complexes[90] will facilitate the deposition of polycatechol coatings onto different substrates. Meanwhile, those interactions will also add up to the complexity of the polymerization process. It was worth mention that during the polymerization process, re-oxidation of catechol groups can also take place through Schiff base and Michael addition reactions due to the existence of amine groups.[18,167] Although we describe the formation of coating on substrate using the term polymerization, however, pDA coatings generally contains significant amount of non-covalent component because it is reported that pDA can be incompletely degraded in conditions that disturb the inherit supramolecular interactions.[63,90] The actually molecular structure of pDA coatings is still under great debate.

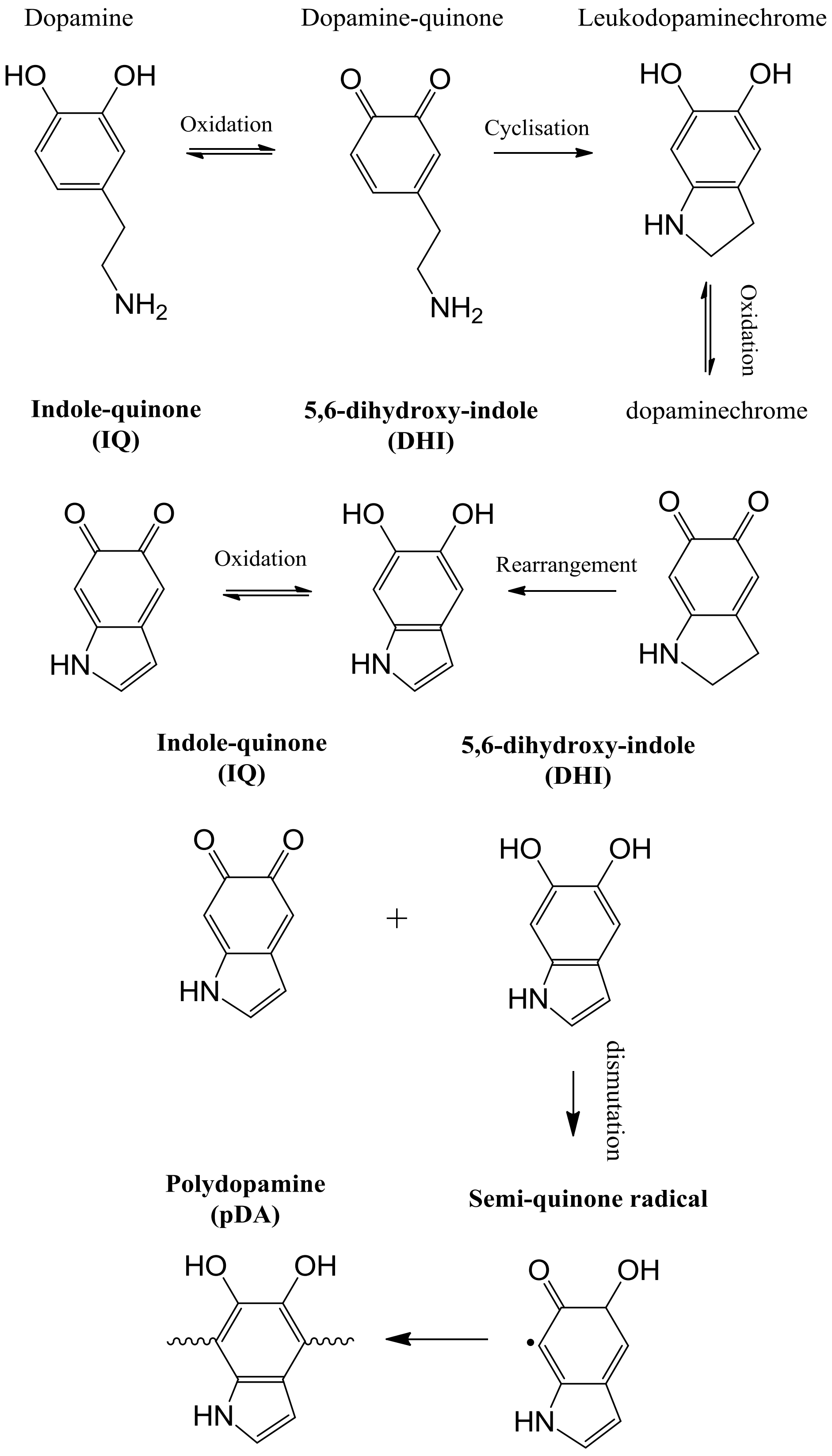

Figure 6.10 Scheme illustrating the formation process of polydopamine.

Coating mechanism for pNE

It is known that the coexist of nanosphere and nanosheet when DHI (a critical intermediate in pDA coating) is polymerized generally result in roughness surfaces. And there is even report for preparing pDA spherical nanoparticles utilize the intrinsic nature of the oxidative polymerization of DHI to render spherical particle.[226] Norepinephrine (NE), another key analogue of dopamine with a hydroxyl group attached to the alkyl chain, shows sustained capacity for material-independent surface chemistry and smoother, more hydrophilic coatings is achieved as compared to pDA coatings.[67] Detailed research using high-performance liquid chromatography and mass spectrometry reveals that beside DHI, a new intermediate named 3,4-dihydroxybenzaldehyde (DHBA) was identified during the polymerization of NE. And this new intermediate resulted in a remarkable difference in surface morphology.[67]

Figure 6.11 and 6.12 shows the detailed process of how DHBA was generated during reaction and the formation of pNE film. Firstly, NE could easily get oxidized into O-quinone form, then cyclisation, reaction and rearrangement take place to generate the intermediate DHI, which is the same as pDA polymerization process. At the meantime, the tautomerization and non-melanogenic breakdown happens to the O-quinone to generate a new intermediate DHBA. The subsequent reaction contains a reversible Schiff-base formation reaction between DHBA and NE with subsequent reduction of the imine bond aggregates. Then the intra-molecular reduction triggered by the catechol in DHBA rather than in NE results in the DHBA-NE product, which plays an important role in decreasing the roughness of functionalized surfaces.[67] The intra-molecular cross-linking between DHBA-NE, DHI and oxidized DHI will be trigged by semi-quinone radicals generate by dismutation of DHI. Finally, smooth pNE film was formed on substrate with the structure defined in Figure 6.12.

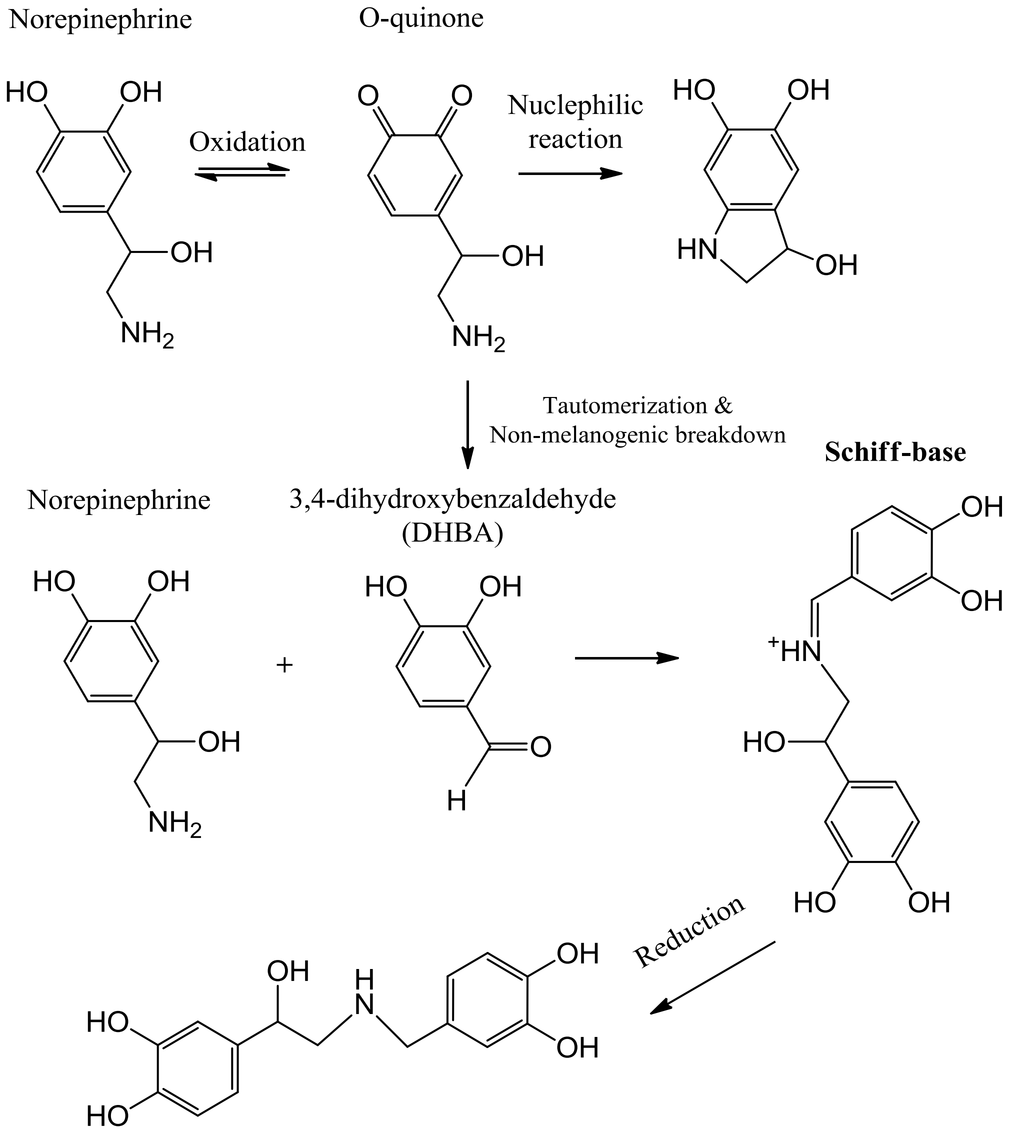

Figure 6.11 Scheme of the oxidation pathways of pNE in which the new catecholamine intermediate called DHBA-NE was identified.[67]

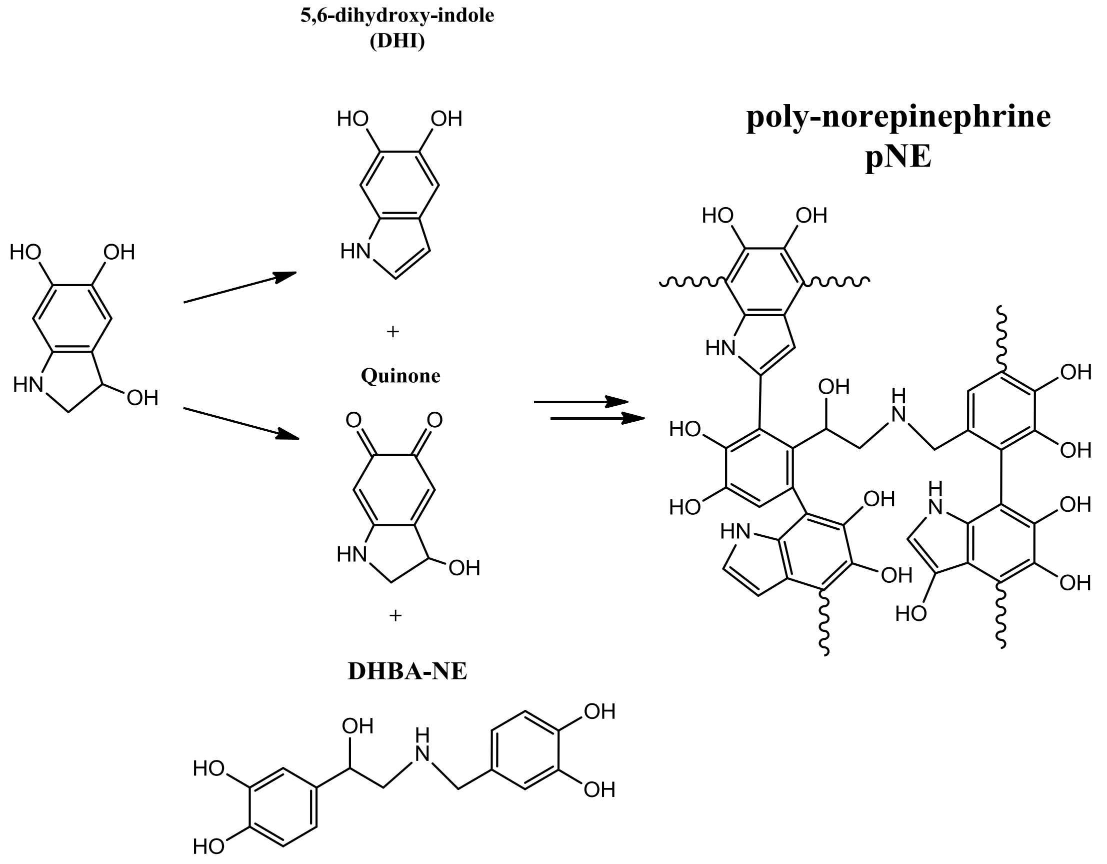

Figure 6.12 Scheme of the formation and structure of pNE through DHI and DHBA-NE.[67]

In addition to the cross-link process mentioned above, other interactions that play important roles for dopamine polymerization such as π-π stacking,[90] van der Waals force,[1] hydrophobic interaction,[43] cation-π interactions,[224] co-ordination bonds,[71] chelating effect with metal ions,[74] hydrogen bonding,[90,218] and quinhydrone charge-transfer complexes[90] could play important roles in the substrate independent adhesion and coating as well.

Coating mechanism of PC

In previous paragraphs, we briefly described the polymerization process of DA and NE. In this paragraph, we would like to discuss the polymerization process of polypyrocatechol (pPC) on mica. It is known that pyrocatechol is an excellent molecular model for studying oxidative polymerization process since it is the simplest molecule containing the very reactive O-diphenol group, which is quickly oxidized to corresponding semiquinone or quinine form (Figure 6.13).[227] The free radicals generated during dismutation will trigger the polymerization process and forming a layer of coating on substrates. And it was worth mention that the polymerization of pyrocatechol mainly through either forming C-C bond or C-O-C bond (Figure 6.13). These reactions increase when the pH of the solution is raised, although the same reactions can take place at appreciable rates under acidic conditions, especially if metal catalysts are present. Similar to the polymerization of DA and NE, other factors mentioned above such as π-π stacking, van der Waals force, hydrophobic interaction, chelating effect with metal ions, hydrogen bonding, quinhydrone charge-transfer complexes could also contribute to the deposition of polycatechol coatings onto different substrates. According to previous AFM imaging results, the pPC shows less density as compared to pDA and pNE film, probably due to the lack of intermediates such as DHI and DHBA during oxidation.

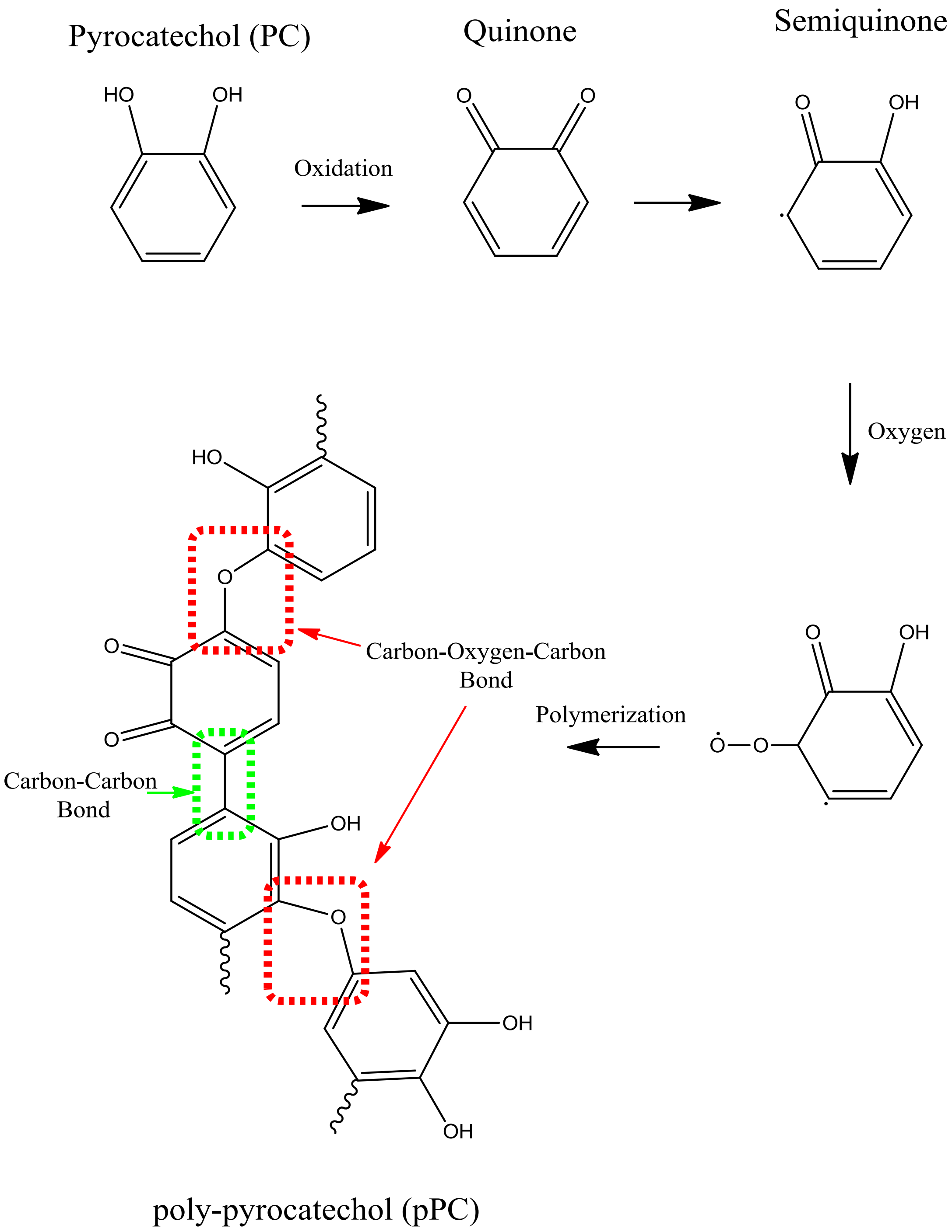

Figure 6.13 Scheme of the formation and structure of pPC through C-C bond or C-O-C bond.

6.3.4 Surface Interactions

In previous sections, surface morphology and possible deposition mechanism of the three compounds pDA, pNE and pPC were described, and smooth pNE and pPC coating with roughness less than 1 nm could be achieved. So in this part, the effect of amine groups on the molecular interactions and nanomechanics of pPC and pNE were investigated in situ by using the SFA technique. The interaction force as a function of separation distance (F/R *vs.* D) were obtained by coating either pNE or pPC layer on two opposing mica surfaces in 10 mM PBS buffer, at pH 8.4, with the schematic view shown in Figure 6.14.

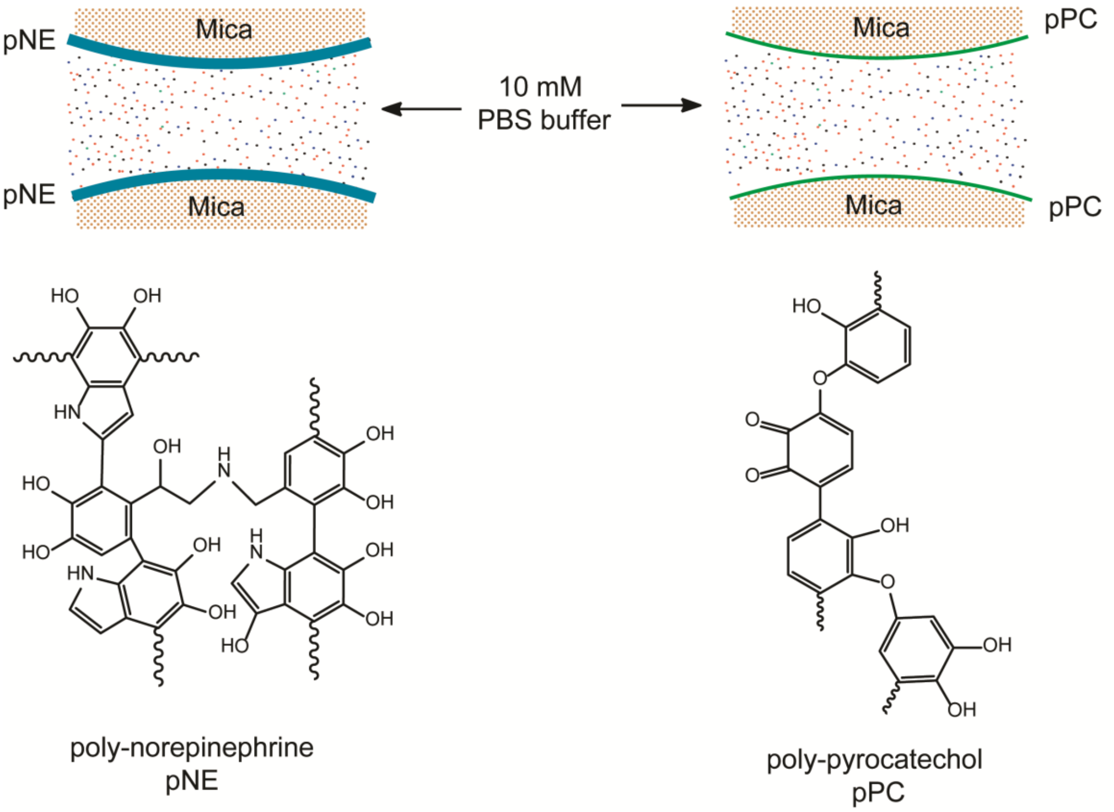

Figure 6.14 Chemical structure and schematic illustration of surface forces measurements of pNE and pPC coated mica surfaces using the SFA technique.

In order to exclude possible influence of mica substrate, surface force measurements were firstly conducted between two fresh cleaved mica surfaces in 10 mM PBS buffer. Figure 6.15 shows the force-distance profile for fresh cleaved mica surfaces when approaching (black solid circle) and separating (red open circle) from each other in 10 mM PBS buffer. Only repulsive force was observed with the repulsion force starts from 20 nm during approaching and the separation force curve almost overlaps with the approaching curve. The confined film thickness is measured to be 0.9 nm, which is close to the diameter of single layer hydrated ion layers (~0.8 nm), suggesting a monolayer of hydrated sodium ions was confined in between two mica surface. This layer of hydration ion will lead to the so called hydration repulsion force during both approaching and separation. This result is consistent with previous report based on fresh mica surfaces in salt aqueous solutions.[1,228]

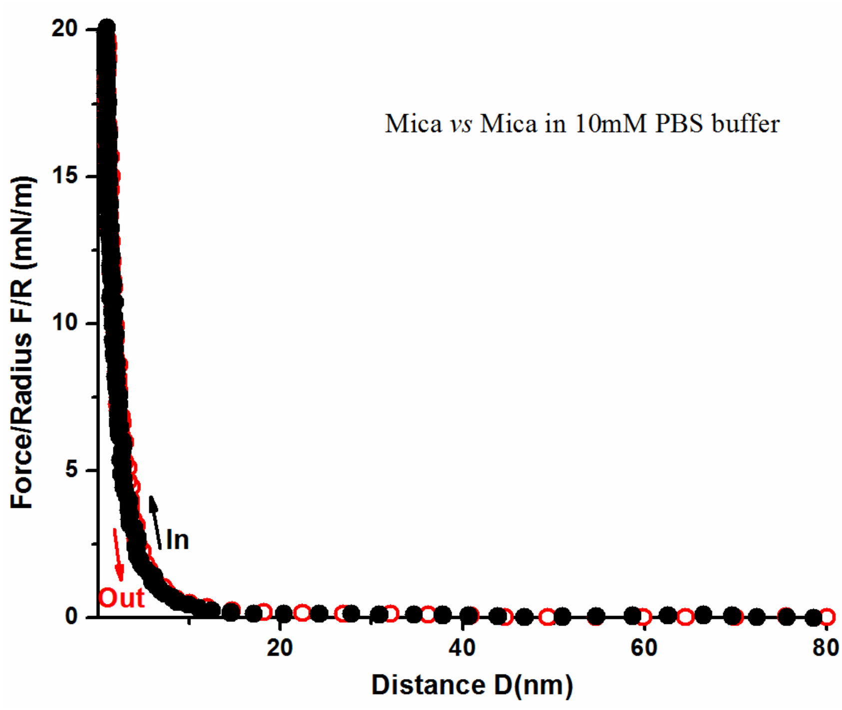

Figure 6.15 Force-distance (*F/R vs. D*) profile of mica *vs.* mica surface in 10 mM PBS buffer.

By injecting NE or PC that dissolved in 10 mM PBS buffer at pH 8.4, into the gap between two opposing mica surfaces, in situ polymerization of polycatechols and their coating on both the mica surfaces in the SFA chamber was initiated due to the presence of oxygen in solution. Figure 6.16 shows the schematic illustration of force measurements between two mica surfaces after in situ polymerization of pNE or pPC for 2 min (Figure 6.16a) and 480 min (Figure 6.16b), respectively. It is found that only pure repulsive force is measured during approaching for both pNE and pPC coatings at different deposition time. However, no significant adhesion was detected in the case of pPC after solution injection immediately and after polymerization for 480 min: $F_{ad}/R < \sim 0.5$ mN/m when t = 2 min, and $F_{ad}/R < \sim 0.9$ mN/m when t = 480 min (blue squares shown in Figure 6.16). In contrast, pNE induced large adhesion hysteresis and strong adhesion (F_{ad}/R ~ 6.35 mN/m) between the two interacting surfaces after the in situ polymerization of pNE for only 2 min (red circles, Figure 6.16a), and more importantly, the measured adhesion reached ~ 30.2 mN/m after polymerization for 480 min (red circles, Figure 6.16b).

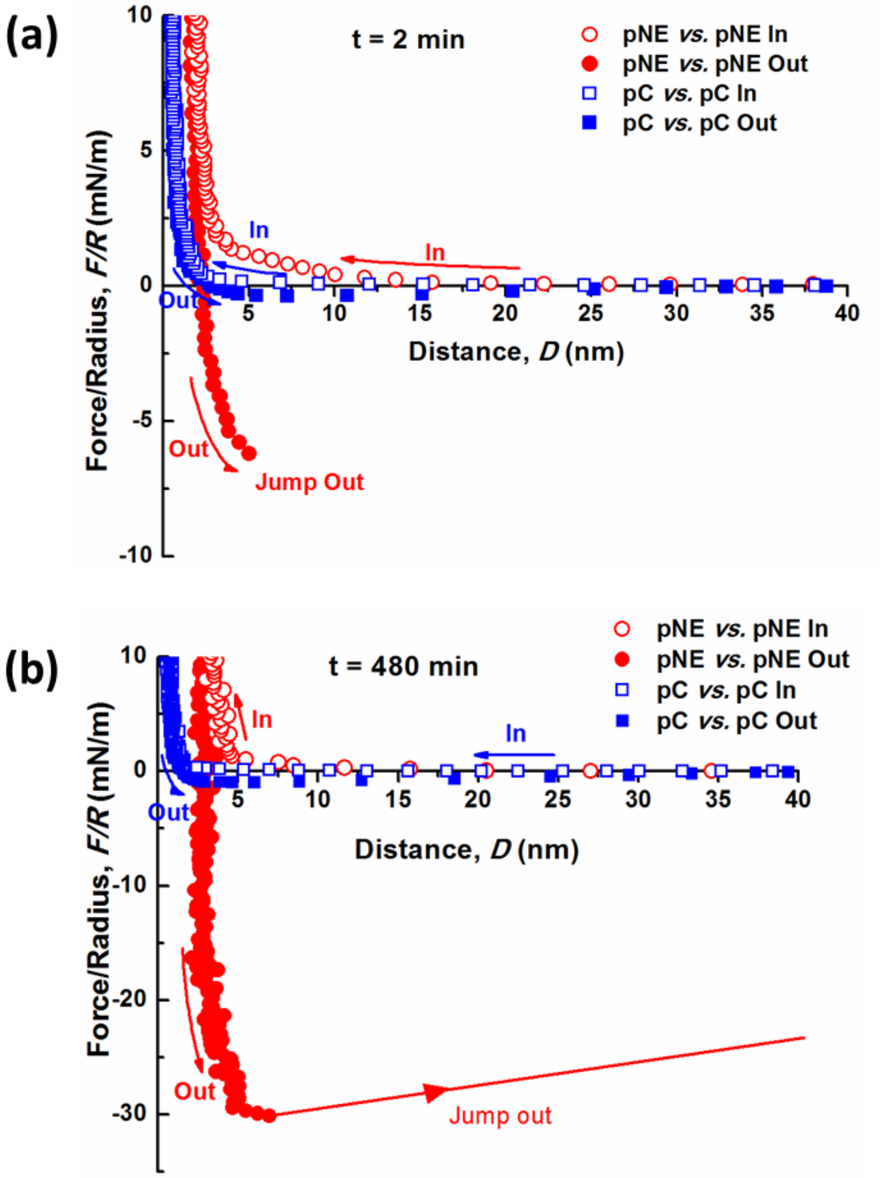

Figure 6.16 Force-distance curves (F/R vs. D) of *in situ* polymerization at 2 min (a) and 480 min (b) between two opposing pNE (red) and pPC (blue) surfaces. Open circle indicates approach and closed circle suggests separation.

During the polymerization process, the interaction forces between two polycatechol or polycatecholamine layers on mica were measured at an interval of approximately 30 min so as to monitor the change of adhesion and film thickness. Figure 6.17a shows that for the case of pNE, the adhesion strength gradually increased after the polymerization initiation and reached up to F_{ad}/R ~ 30 mN/m after in situ polymerization for 480 min, however, the adhesion strength of pPC coatings remains to be less than 1 mN/m at the same polymerization time. The adhesive strength between pNE layers was approximately 30 times higher than that of pPC 8 h after initiating the polymerization process. In addition, as shown in Figure 6.17b, the “hardwall” distance D_h, *i.e.*, the thickness of confined coating materials between two opposing mica surfaces that does not seem to change with an increasing normal compressive load or pressure, was also carefully monitored to probe the time dependence of the thickness of the polycatechol coating on mica. More importantly, the pNE film thickness (*i.e.*, half of the measured steric wall distance) increased almost 2-fold from 0.8 nm at a polymerization time of t = 20 min to 1.6 nm at t = 480 min, whereas the thickness of pPC only increased by approximately 35% over the same polymerization time (Figure 6.17b). These results imply that amine functional groups can significantly contribute to the adhesion between polyphenol films.

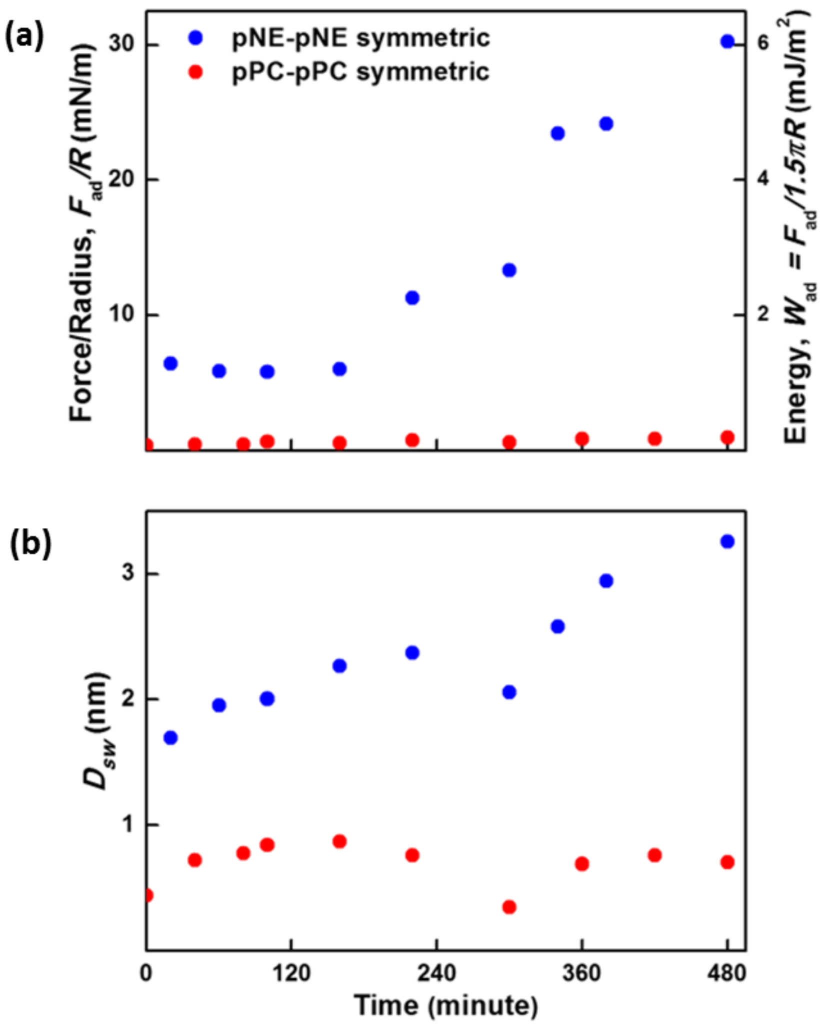

Figure 6.17 Time dependent a) adhesion and b) film thickness of pNE and pPC films on mica, which shows that the pNE possessed a much stronger cohesion capacity than pPC.

Another point needs to be mentioned is that, as shown in Figure 6.18, Force-distance curves for three sequential force measurements using pNE film (polymerization for 480 min) shows reversible adhesion with the adhesion strength stays at the range of 28-30 mN/m during separation for the same contact time and the same position. The adhesion strength even increases a little bite after the first approaching and separation, and the increase of adhesion could be due to the conformation change of non-covalent bonded functional groups on pNE film. The measured reversible adhesion between two pNE surface provides strong evidence that covalent bonding is not the main reason for the adhesion measured. And this results is consistent with previous report based on solid state spectroscopic, which proves that polycatecholamine may not be a purely covalent polymer but instead a supramolecular aggregates with multiple kind of interactions.[33] Non-covalent bonds such as cation-π interaction, hydrophobic interaction or hydrogen bonding could play important roles for pNE films, and the detailed discussion will be given in later sections.

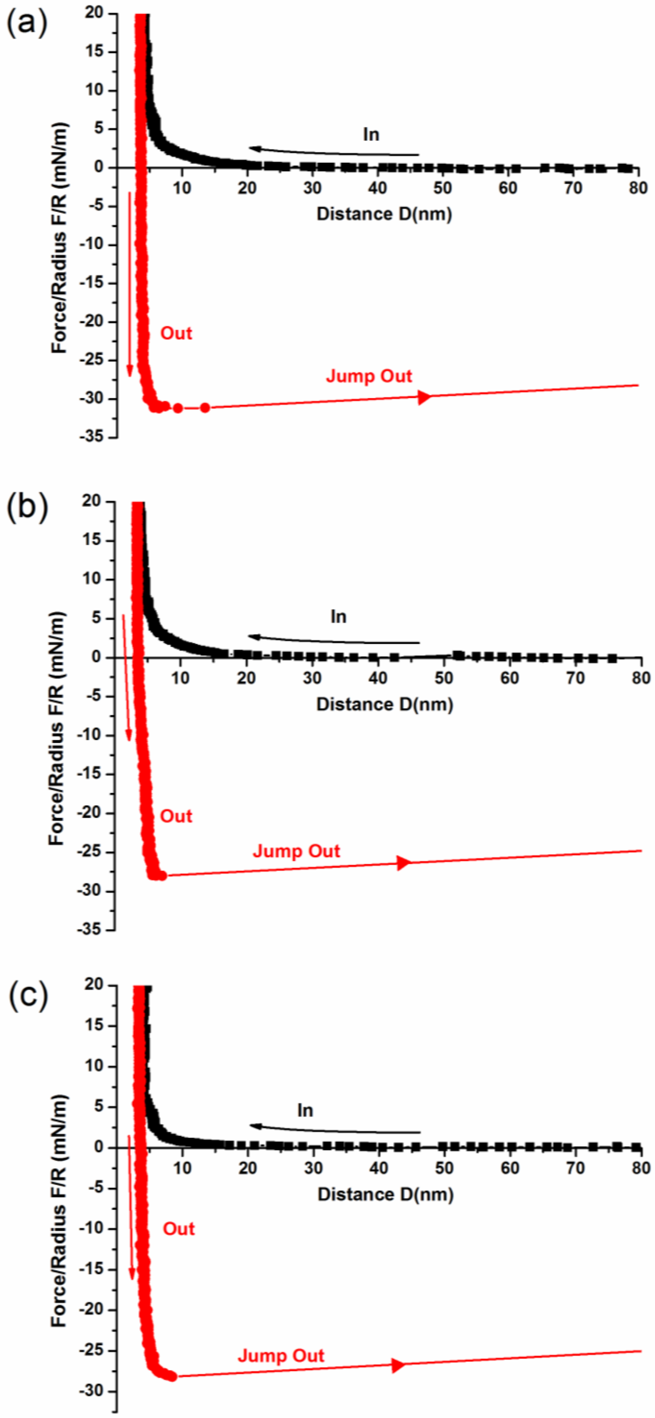

Figure 6.18 Force-distance curves for three sequential force measurements (a), (b) and (c) between two pNE layers 8 h after *in situ* polymerization at the same interaction position, which show repetitive and reversible adhesion.

In order to further confirm the adhesion measured between two pPC surfaces was not due to mica and pPC interaction, another control experiment based on mica surface and a pPC film coated by in situ polymerization at 20 mg/ml PC for 8 h in 10 mM PBS pH 8.4 was conducted. As shown in Figure 6.19, pure repulsive forces is measured during both approaching and separation, and the two curves almost overlaps, which excludes the possible contribution of adhesion measured between pPC and fresh mica surface. The film thickness is measured to be 8 nm, which is higher than lower concentration of PC for polymerization.

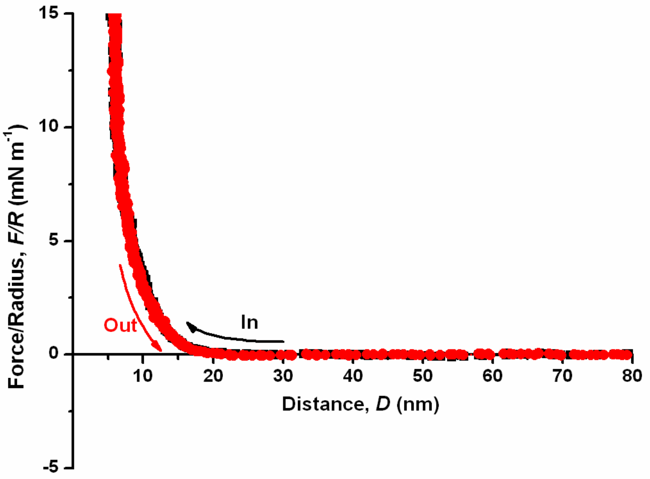

Figure 6.19 Force-distance profiles between a bare mica surface and a pPC film coated by in situ polymerization at 20 mg/ml PC for 8 h in 10 mM PBS pH 8.4, and pure repulsive forces were measured.

6.3.5 Interaction mechanisms between catecholamine and substrates

One might wonder how to enhance the molecular attraction of the poly(catechol) coating by introducing a primary amine group when poly(catechol) polymerizes in aqueous solutions. Herein in this section, we would like to discuss the possible driving mechanisms for the adhesive force we measured based on both our experiment results and previous reported results.

For a typical polycatecholamine deposition process onto a smooth surface, those non-covalent interactions such as vDW force, hydrogen bonding, coordination and chelation effect, hydrophobic interactions and electrostatic interaction could play dominant role for the initial coating step especially for metal and metal oxide surfaces. Later on, other interactions like intra-layer π-π-interactions, cation–π interactions, covalent-bonding formation and cross-linking could take over along with other interactions at the same time.

Previous research indicates that poly(catecholamine) coating is generally negative charged at pH 8.4,[40] and mica surface is also negatively charged at pH 8.4, so the electrostatic attraction is repulsive instead of attractive. The good reversibility of the adhesive force between in situ deposited pNE surface proves that covalent bonds is not the major cause of the measured adhesion, thus those non-covalent interactions, such as cation-π interaction, π-π interaction, vdW forces, hydrogen bond, hydrophobic forces could play dominant roles for this case. which will be discussed in the following sections.

a) Cation-π interaction

The cation-π interaction is a monopole–quadrupole electrostatic forces that widely present between positively charged ions and an electron-rich π system.[85] This interaction is related to lots of important biological phenomena such as protein folding, potassium channel blockers, nicotinic acetylcholine receptors.[86] Additionally, the cation–π interactions is reported to be the strongest non-covalent interaction in the aqueous environment due to the low desolvation penalty of the aromatic group in water.[88,229] Recent SFA study proved that cation–π interaction is critical to achieve strong underwater adhesion and cross-linking.[230] Our recent study demonstrated that this short-ranged cation–π interaction is even strong enough to induce a like charged coacervation, *viz.* liquid-liquid phase separation, of two positively charged polyelectrolytes by overcoming the longer-range electrostatic repulsion in aqueous environment.[88] Thus in the pNE case, cation–π interaction between positively charged amine groups, the indolic crosslinks and other electron-rich structure could all contribute to the adhesion we measured. Previous research indicated that the cation–π interaction can be affected by the presence of other types of cations, such as K^+, Na^+, tetraethylammonium ions, nicotinic acetylcholine, thus we designed further experiments by adding compete ions such as K^+ into the solution to testify our hypothesis. As shown in Figure 6.20, after gradually increase the concentration of KNO_3 in the pNE solution, the measured adhesion quickly decreases from ~ 30 mN/m in 0 mM KNO_3 to ~9 mN/m in 10 mM KNO_3, and finally goes to less than 1 mN/m in 100 mM KNO_3. The significant decreasing of adhesion after adding K^+ proves that the positively changed amine groups could be replaced by K^+ ions, thus reducing the cation-π interactions between amine and π rich systems such as indole and benzene groups.

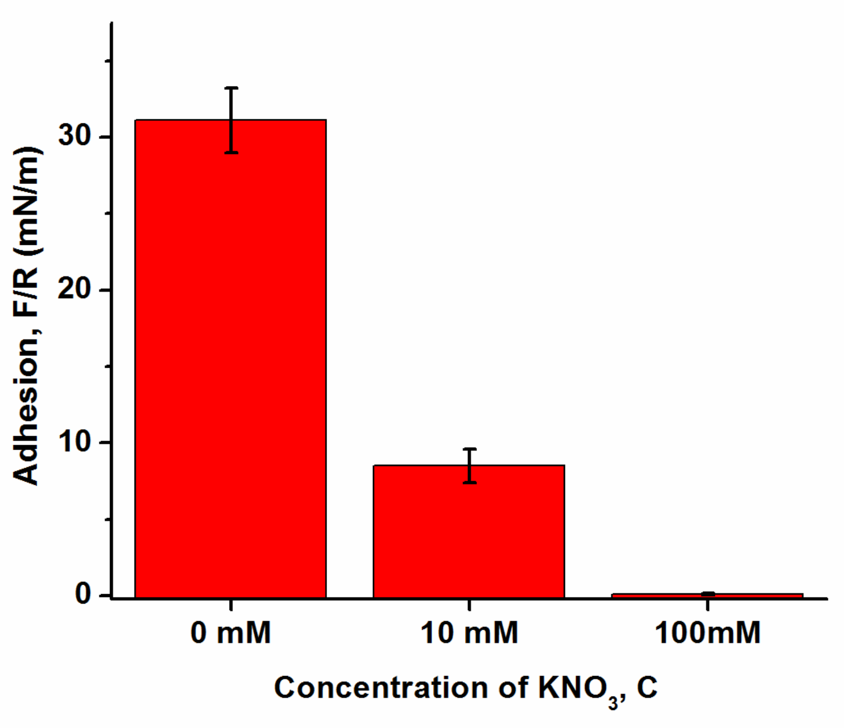

Figure 6.20 Adhesion measured between two pNE surfaces with the increasing of KNO_3 concentration.

b) Synergistic effect between catechol and amine groups

A recent study suggested that the catechol and amine groups could perform synergistically to enhance interfacial adhesion. The lysine groups appears to displace hydrated potassium ions on mica surface, thus facilitate the further chelation and attaching of catechol groups onto mineral surfaces.[77]

c) Hydrogen Bond

Hydrogen bonding has the ability to compete with water molecules adsorbed on surface, thus this kind of interaction could plays an essential role in the initial stage of molecular assembly. The oxygen atoms of the oxides such as mica and silica could also form hydrogen bonding with the phenolic OH groups. For the case of pNE, this interaction could also contribute to the measured adhesion but it may not be the main reason.

d) *π*-*π* stacking

π-π-interaction, a type of quadrupole–quadrupole interaction between aromatic rings of indolic and catechol-phenyl complexes, could also facilitate the cross-linking and polymerization of catecholamine compounds. The π-π-interaction plays an important role for the stability of proteins in biological systems since this interaction could provide a significant amount of binding enthalpy. And theπ-π-interaction between indolic cross-links and other electron-rich structures could enhance the measured adhesion.

e) VdW force

Van der Waals force is a dispersion force which is omnipresent and plays important roles in adhesion of surfaces. For both pNE or pPC coatings that are in contact under symmetric configurations, this factor could also enhance the adhesion during the separation.

f) Hydrophobic force

Although the contact angle result suggests that the pNE surface is hydrophilic, there are still some hydrophobic domains such as benzene rings in the polymerized film, which might also add up to the adhesion between the two polymer surface during separation in aqueous solutions.

The above mentioned mechanisms are the typical ones that could play dominant roles for the adhesion between two pNE surface, for other cases such as when there are multi-valence ions (e.g., Fe^{3+}, Ti^{4+}) in the solution or on the surface, the metal-catechol coordination and chelation effect cannot be ignored.

6.4 Conclusion

In this chapter, we described the study of deposition, polymerization and nanomechanics of poly-dopamine, poly-norepinephrine and poly-pyrocatecol on fresh cleaved mica surface, respectively. We report on the direct evidence regarding the interfacial contributions of a primary amine group to material-independent surface chemistry by utilizing pNE as a model system. As a control, the interaction of poly(pyrocatechol) (pPC), a self-polymerized catechol without any amine moiety, was also tested using SFA. Our data suggest that the contribution from the primary amine groups or assistance from metal ions or metal oxides should not be overlooked when attempting to coat a surface evenly and thickly.

CHAPTER 7

CONCLUSIONS AND FUTURE DIRECTIONS

7.1 Conclusion and Original Contributions

This thesis research was mainly focused on understanding the deposition and related surface interaction mechanisms of functional coatings on various kinds of substrates using nano-mechanic tools such as SFA and AFM. The original contributions were listed as below.

1. The deposition of the long chain hydrocarbon silane, octadecyltrichlorosilane (OTCS), on fresh mica surface with few active sites *via* a vapor deposition method was systematically studied for the first time. AFM imaging reveals that the deposition process mainly contains two stages: silane molecules first react with the limited silanol groups to form a smooth layer and then the initial layer could serve as nucleation sites for further deposition to form a rough OTCS coating. Secondly, the as-obtained OTCS multi-layer films can undergo hydrolysis in strongly acidic conditions, removing the majority of the multilayered OTCS coating and leaving scattered nanoaggregates on the substrate. Additionally, the contact mechanics tests on the as-obtained OTCS-modified mica surfaces using SFA demonstrate that the OTCS coatings could significantly reduce the surface adhesion and adhesion hysteresis. The surface interactions of the OTCS-2h and OTCS-8h samples can be reasonably

described by the classic DLVO theory. However, for the samples obtained with longer deposition times (i.e., OTCS-48h), the hydrophobic interaction and steric interaction play an important role due to their enhanced surface hydrophobicity and surface roughness. The obtained experiment results in this work provide useful insights into the deposition behaviors of alkylsilanes on substrates possessing low density of reactive sites *via* vapor deposition method as well as the fundamental interactions of the deposited alkylsilane surfaces in aqueous solution.

2. A new type of smooth poly(pentafluorophenyl acrylate)-*b*-polystyrene (PPFPA-*b*-PS) polymer coating covalently end-attached onto mica surface was obtained using a “graft to” methodology *via* amino group reacting with petal-fluoro ester. The hydrophobicity of end grafted polymer surface can be modulated by adjusting the deposition time of the precursor layer (3-Aminopropyl) triethoxysilane. Surface force measurements show long-range attraction between two end-grafted polymer surfaces with water contact angle of ~91°. Both degassing and increasing NaCl concentrations could lead to shortened range of attraction, indicating the important role of dissolved gas or surface-supported bubbles on interactions between hydrophobic polymer surfaces in aqueous media. These experimental results obtained based on stable, grafted PPFPA-*b*-PS polymer surface help to better understand the interaction mechanisms between polymers surface in aqueous solutions.

3. A simple and efficiency approach for preparing stable and covalently bonded polymeric films through spin assisted layer-by-layer assembly has been developed.

The multi-layer polymer surfaces were achieved by forming amido bond between PPFPA-*b*-PS and polyethyleneimine (PEI). Switched hydrophobicity is achieved by alternated deposition of PEI layers (hydrophilic) and PPFPA-*b*-PS layers (hydrophobic). Moreover, this coating method could be applied to a series of flat substrates including mica, silicon and glass slides. SFA measurement based on three different configurations including PEI *vs.* PEI, PPFPA-*b*-PS *vs.* PPFPA-*b*-PS, and PEI *vs.* PPFPA-*b*-PS, provide further evidence for the covalent bonding between PEI and PPFPA-*b*-PS layers from molecular scale. Additionally, the multi-layer polymer film shows the possibility of post-functionalization by chemical reaction between excessive amine group and PPFPA ester groups. Importantly, a facile method has been developed for preparing robust freestanding polymeric films by peeling off the polymer films from silicon substrates in strong base or strong acid (*e.g.* 1 M NaOH, 1M HCl). The obtained free-standing films show good transparency, excellent mechanic property, easy transfer ability and excellent stability in strong acid, strong base, high salt and organic solvent.

4. The study on the deposition and polymerization mechanisms of poly(dopamine), poly(norepinephrine) and poly(pyrocatecol) on fresh cleaved mica surface has been conducted systematically. Based on the smooth poly(catecholamine) surface, the effect of amine groups on the polymerization and surface interactions of catecholamine reagents has been investigated. Importantly, the SFA results indicate that the adhesive strength between poly-norepinephrine layers measured by SFA is thirty times higher than that of a poly(pyrocatechol) coating without any amine

moiety at the same polymerization time. The significant improvement of adhesion after introducing primary amine provides direct evidence regarding the interfacial contributions of a primary amine group to material-independent surface chemistry and adhesion. Amine groups play vital roles in the design and development of mussel-inspired catechol- coating materials.

7.2 Future Work

Further steps can be taken to utilize those functional coatings to achieve novel smart surfaces.

1. For the OTCS functionalized surface, the vapor deposition method could be applied to prepare super-hydrophobic surface by combining with nanoscale roughness. The silane vapor treatment method can be extended to surfaces with irregular shapes, or even mesoporous materials. Furthermore, the OTCS-vapor functionalized surfaces could be etched selectively to prepare patterned surface with control hydrophobicity, which shows potential application in Nano/Micro Electro Mechanical Systems.

2. For end-grafted PPFPA-*b*-PS surface, the existence of air bubbles could be further characterized with in situ imaging techniques such as Atomic Force Microscope. The excessive amount of active ester groups could be further modified to realize other functions by reacting with compounds that are rich in primary or secondary amines. Moreover, PFPA is an active ester that can be used to prepare functional polymers which have the capability of grafting onto various kinds of amine-functionalized surfaces.

3. For multi-layer polymeric thin films, functionalized nano-particles such as Ag, Fe_2O_3, Au nano-particles could be incorporated into the polymeric films for achieving stimuli-responsive polymer films. Moreover, water-soluble components such as salts and glucose could be introduced into the layered structure for preparing porous, stable, freestanding film for applications like oil-water separation and gas separation.

4. Surface force results demonstrate that amines play critical roles on the polymerization and adhesion of catecholamine compound at the interface. Further research might be conducted to develop universal and low cost coatings on various substrates based on catechol chemistry and different amines.

BIBLIOGRAPHY

1. Israelachvili, J. N. *Intermolecular and surface forces: revised third edition*. Academic Press: 2011.

2. Arkles, B. Hydrophobicity, hydrophilicity and silane surface modification. **2009**, pp 1-80.

3. Feng, L.; Li, S.; Li, Y.; Li, H.; Zhang, L.; Zhai, J.; Song, Y.; Liu, B.; Jiang, L.; Zhu, D. Super‐hydrophobic surfaces: from natural to artificial. *Adv. Mater.* **2002,** *14*, 1857-1860.

4. Gao, X.; Jiang, L. Biophysics: water-repellent legs of water striders. *Nature* **2004,** *432*, 36-36.

5. Zheng, Y.; Gao, X.; Jiang, L. Directional adhesion of superhydrophobic butterfly wings. *Soft Matter* **2007,** *3*, 178-182.

6. Feng, L.; Zhang, Y.; Xi, J.; Zhu, Y.; Wang, N.; Xia, F.; Jiang, L. Petal effect: a superhydrophobic state with high adhesive force. *Langmuir* **2008,** *24*, 4114-4119.

7. Zhang, Y.-L.; Xia, H.; Kim, E.; Sun, H.-B. Recent developments in superhydrophobic surf aces with unique structural and functional properties. *Soft Matter* **2012,** *8*, 11217-11231.

8. Faghihnejad, A.; Zeng, H. Hydrophobic interactions between polymer surfaces: using polystyrene as a model system. *Soft Matter* **2012,** *8*, 2746-2759.

9. Patrick, H. N.; Warr, G. G.; Manne, S.; Aksay, I. A. Surface micellization patterns of quaternary ammonium surfactants on mica. *Langmuir* **1999,** *15*, 1685-1692.

10. Christenson, H.; Claesson, P.; Berg, J.; Herder, P. Forces between fluorocarbon surfactant monolayers: Salt effects on the hydrophobic interaction. *J. Phys. Chem.* **1989,** *93*, 1472-1478.

11. Meyer, E. E.; Rosenberg, K. J.; Israelachvili, J. Recent progress in understanding hydrophobic interactions. *Proc. Natl. Acad. Sci. U. S. A.* **2006,** *103*, 15739-15746.

12. Donaldson Jr, S. H.; Das, S.; Gebbie, M. A.; Rapp, M.; Jones, L. C.; Roiter, Y.; Koenig, P. H.; Gizaw, Y.; Israelachvili, J. N. Asymmetric electrostatic and

hydrophobic–hydrophilic interaction forces between mica surfaces and silicone polymer thin films. *ACS Nano* **2013,** *7*, 10094-10104.

13. Wong, T.-S.; Kang, S. H.; Tang, S. K.; Smythe, E. J.; Hatton, B. D.; Grinthal, A.; Aizenberg, J. Bioinspired self-repairing slippery surfaces with pressure-stable omniphobicity. *Nature* **2011,** *477*, 443-447.

14. Epstein, A. K.; Wong, T.-S.; Belisle, R. A.; Boggs, E. M.; Aizenberg, J. Liquid-infused structured surfaces with exceptional anti-biofouling performance. *Proc. Natl. Acad. Sci. U. S. A.* **2012,** *109*, 13182-13187.

15. Kim, P.; Wong, T.-S.; Alvarenga, J.; Kreder, M. J.; Adorno-Martinez, W. E.; Aizenberg, J. Liquid-infused nanostructured surfaces with extreme anti-ice and anti-frost performance. *ACS Nano* **2012,** *6*, 6569-6577.

16. Drelich, J.; Chibowski, E.; Meng, D. D.; Terpilowski, K. Hydrophilic and superhydrophilic surfaces and materials. *Soft Matter* **2011,** *7*, 9804-9828.

17. Carter, C. B.; Norton, M. G. *Ceramic materials: science and engineering*. Springer Science & Business Media: 2007.

18. Lee, B. P.; Messersmith, P. B.; Israelachvili, J. N.; Waite, J. H. Mussel-inspired adhesives and coatings. *Annu. Rev. Mater. Res.* **2011,** *41*, 99.

19. Lee, H.; Dellatore, S. M.; Miller, W. M.; Messersmith, P. B. Mussel-inspired surface chemistry for multifunctional coatings. *Science* **2007,** *318*, 426-430.

20. Sileika, T. S.; Barrett, D. G.; Zhang, R.; Lau, K. H. A.; Messersmith, P. B. Colorless multifunctional coatings inspired by polyphenols found in tea, chocolate, and wine. *Angew. Chem., Int. Ed.* **2013,** *52*, 10766-10770.

21. Barrett, D. G.; Sileika, T. S.; Messersmith, P. B. Molecular diversity in phenolic and polyphenolic precursors of tannin-inspired nanocoatings. *Chem. Commun.* **2014,** *50*, 7265-7268.

22. Ezzat, M.; Huang, C.-J. Zwitterionic polymer brush coatings with excellent anti-fog and anti-frost properties. *RSC Adv.* **2016,** *6*, 61695-61702.

23. He, K.; Duan, H.; Chen, G. Y.; Liu, X.; Yang, W.; Wang, D. Cleaning of oil fouling with water enabled by zwitterionic polyelectrolyte coatings: Overcoming the

imperative challenge of oil–water separation membranes. *ACS Nano* **2015,** *9*, 9188-9198.

24. Zeng, H.; Huang, J.; Tian, Y.; Li, L.; Tirrell, M. V.; Israelachvili, J. N. Adhesion and detachment mechanisms between polymer and solid substrate surfaces: using polystyrene–mica as a model system. *Macromolecules* **2016,** *49*, 5223-5231.
25. Zeng, H. *Polymer adhesion, friction, and lubrication*. John Wiley & Sons: 2013.
26. Muller, P. Glossary of terms used in physical organic chemistry (IUPAC Recommendations 1994). *Pure Appl. Chem.* **1994,** *66*, 1077-1184.
27. Ruths, M.; Israelachvili, J. N. Surface forces and nanorheology of molecularly thin films. In *Nanotribology and nanomechanics*, Springer: 2008; pp 417-515.
28. Huang, J.; Yan, B.; Faghihnejad, A.; Xu, H.; Zeng, H. Understanding nanorheology and surface forces of confined thin films. *Korea-Aust. Rheol. J.* **2014,** *26*, 3-14.
29. Chen, Y.; Au, J.; Kazlas, P.; Ritenour, A.; Gates, H.; McCreary, M. Electronic paper: flexible active-matrix electronic ink display. *Nature* **2003,** *423*, 136-136.
30. Israelachvili, J.; Pashley, R. The hydrophobic interaction is long range, decaying exponentially with distance. **1982**.
31. Beattie, J. K.; Djerdjev, A. M. The pristine oil/water interface: Surfactant ‐ free hydroxide ‐ charged emulsions. *Angew. Chem., Int. Ed.* **2004,** *43*, 3568-3571.
32. Meyer, E. E.; Lin, Q.; Israelachvili, J. N. Effects of dissolved gas on the hydrophobic attraction between surfactant-coated surfaces. *Langmuir* **2005,** *21*, 256-259.
33. Siretanu, I.; Chapel, J. P.; Drummond, C. Water− Ions Induced Nanostructuration of Hydrophobic Polymer Surfaces. *ACS Nano* **2011,** *5*, 2939-2947.
34. Parker, J. L.; Claesson, P. M.; Attard, P. Bubbles, cavities, and the long-ranged attraction between hydrophobic surfaces. *J. Phys. Chem.* **1994,** *98*, 8468-8480.
35. Craig, V. S. J. Very small bubbles at surfaces—the nanobubble puzzle. *Soft Matter* **2011,** *7*, 40-48.
36. Ljunggren, S.; Eriksson, J. C. The lifetime of a colloid-sized gas bubble in water

and the cause of the hydrophobic attraction. *Colloids Surf., A* **1997,** *129*, 151-155.

37. Brenner, M. P.; Lohse, D. Dynamic equilibrium mechanism for surface nanobubble stabilization. *Phys. Rev. Lett.* **2008,** *101*, 214505.

38. Johnson, B. D.; Cooke, R. C. Generation of stabilized microbubbles in seawater. *Science* **1981,** *213*, 209-211.

39. Liu, Y.; Wang, J.; Zhang, X.; Wang, W. Contact line pinning and the relationship between nanobubbles and substrates. *The Journal of Chemical Physics* **2014,** *140*, 054705.

40. Yang, J.; Duan, J.; Fornasiero, D.; Ralston, J. Kinetics of CO 2 nanobubble formation at the solid/water interface. *Phys. Chem. Chem. Phys.* **2007,** *9*, 6327-6332.

41. Berkelaar, R. P.; Zandvliet, H. J.; Lohse, D. Covering surface nanobubbles with a NaCl nanoblanket. *Langmuir* **2013,** *29*, 11337-11343.

42. Wang, Y.; Bhushan, B.; Zhao, X. Nanoindents produced by nanobubbles on ultrathin polystyrene films in water. *Nanotechnology* **2008,** *20*, 045301.

43. Ishida, N.; Kusaka, Y.; Ushijima, H. Hydrophobic attraction between silanated silica surfaces in the absence of bridging bubbles. *Langmuir* **2012,** *28*, 13952-13959.

44. CHRISTENSON, H. K.; CLAESSON, P. M. Cavitation and the interaction between macroscopic hydrophobic surfaces. *Science* **1988,** *239*, 390-392.

45. Palmer, L. A.; Cookson, D.; Lamb, R. N. The relationship between nanobubbles and the hydrophobic force. *Langmuir* **2010,** *27*, 144-147.

46. Attard, P. Long-range attraction between hydrophobic surfaces. *J. Phys. Chem.* **1989,** *93*, 6441-6444.

47. Podgornik, R.; Parsegian, V. An electrostatic-surface stability interpretation of the “hydrophobic” force inferred to occur between mica plates in solutions of soluble surfactants. *Chem. Phys.* **1991,** *154*, 477-483.

48. Meyer, E. E.; Lin, Q.; Hassenkam, T.; Oroudjev, E.; Israelachvili, J. N. Origin of the long-range attraction between surfactant-coated surfaces. *Proc. Natl. Acad. Sci. U. S. A.* **2005,** *102*, 6839-6842.

49. Galamba, N. Water’s structure around hydrophobic solutes and the iceberg model.

J. Phys. Chem. B **2013,** *117*, 2153-2159.

50. Mezger, M.; Reichert, H.; Schöder, S.; Okasinski, J.; Schröder, H.; Dosch, H.; Palms, D.; Ralston, J.; Honkimäki, V. High-resolution in situ x-ray study of the hydrophobic gap at the water–octadecyl-trichlorosilane interface. *Proc. Natl. Acad. Sci. U. S. A.* **2006,** *103*, 18401-18404.

51. Mezger, M.; Sedlmeier, F.; Horinek, D.; Reichert, H.; Pontoni, D.; Dosch, H. On the origin of the hydrophobic water gap: an X-ray reflectivity and MD simulation study. *J. Am. Chem. Soc.* **2010,** *132*, 6735-6741.

52. Ma, C. D.; Wang, C.; Acevedo-Vélez, C.; Gellman, S. H.; Abbott, N. L. Modulation of hydrophobic interactions by proximally immobilized ions. *Nature* **2015,** *517*, 347-350.

53. Chen, S.; Itoh, Y.; Masuda, T.; Shimizu, S.; Zhao, J.; Ma, J.; Nakamura, S.; Okuro, K.; Noguchi, H.; Uosaki, K. Subnanoscale hydrophobic modulation of salt bridges in aqueous media. *Science* **2015,** *348*, 555-559.

54. Zeng, H.; Shi, C.; Huang, J.; Li, L.; Liu, G.; Zhong, H. Recent experimental advances on hydrophobic interactions at solid/water and fluid/water interfaces. *Biointerphases* **2016,** *11*, 018903.

55. Klein, J.; Luckham, P. F. Long-range attractive forces between two mica surfaces in an aqueous polymer solution. *Nature* **1984,** *308*, 836-837.

56. Mao, Y.; Cates, M.; Lekkerkerker, H. Depletion force in colloidal systems. *Phys. A* **1995,** *222*, 10-24.

57. Lekkerkerker, H. N.; Tuinier, R. *Colloids and the depletion interaction*. Springer: 2011; Vol. 833.

58. Godfrey Alig, A.; Akbulut, M.; Golan, Y.; Israelachvili, J. Forces between surfactant‐coated ZnS nanoparticles in dodecane: effect of water. *Adv. Funct. Mater.* **2006,** *16*, 2127-2134.

59. Benz, M.; Rosenberg, K. J.; Kramer, E. J.; Israelachvili, J. N. The deformation and adhesion of randomly rough and patterned surfaces. *J. Phys. Chem. B* **2006,** *110*, 11884-11893.

60. Waite, J. H.; Tanzer, M. L. Polyphenolic substance of Mytilus edulis: novel adhesive containing L-dopa and hydroxyproline. *Science* **1981,** *212*, 1038-1040.

61. Waite, J. H. Surface chemistry: mussel power. *Nat. Mater.* **2008,** *7*, 8-9.

62. Fan, X.; Lin, L.; Messersmith, P. B. Cell fouling resistance of polymer brushes grafted from Ti substrates by surface-initiated polymerization: effect of ethylene glycol side chain length. *Biomacromolecules* **2006,** *7*, 2443-2448.

63. Dreyer, D. R.; Miller, D. J.; Freeman, B. D.; Paul, D. R.; Bielawski, C. W. Perspectives on poly (dopamine). *Chem. Sci.* **2013,** *4*, 3796-3802.

64. Li, Y.; Su, Y.; Zhao, X.; He, X.; Zhang, R.; Zhao, J.; Fan, X.; Jiang, Z. Antifouling, high-flux nanofiltration membranes enabled by dual functional polydopamine. *ACS Appl. Mater. Interfaces* **2014,** *6*, 5548-5557.

65. Wang, Y.; Park, J. P.; Hong, S. H.; Lee, H. Biologically inspired materials exhibiting repeatable regeneration with self‐sealing capabilities without external stimuli or catalysts. *Adv. Mater.* **2016,** *28*, 9961-9968.

66. Zhang, C.; Ou, Y.; Lei, W. X.; Wan, L. S.; Ji, J.; Xu, Z. K. CuSO4/H2O2‐induced rapid deposition of polydopamine coatings with high uniformity and enhanced stability. *Angew. Chem., Int. Ed.* **2016,** *128*, 3106-3109.

67. Hong, S.; Kim, J.; Na, Y. S.; Park, J.; Kim, S.; Singha, K.; Im, G. I.; Han, D. K.; Kim, W. J.; Lee, H. Poly (norepinephrine): ultrasmooth material‐independent surface chemistry and nanodepot for nitric oxide. *Angew. Chem., Int. Ed.* **2013,** *52*, 9187-9191.

68. Lim, C.; Huang, J.; Kim, S.; Lee, H.; Zeng, H.; Hwang, D. S. Nanomechanics of poly (catecholamine) coatings in aqueous solutions. *Angew. Chem., Int. Ed.* **2016,** *55*, 3342-3346.

69. Yang, H.-C.; Xu, W.; Du, Y.; Wu, J.; Xu, Z.-K. Composite free-standing films of polydopamine/polyethyleneimine grown at the air/water interface. *RSC Adv.* **2014,** *4*, 45415-45418.

70. Glavin, G. B. Stress and brain noradrenaline: a review. *Neurosci. Biobehav. Rev.* **1985,** *9*, 233-243.

71. Lee, H.; Scherer, N. F.; Messersmith, P. B. Single-molecule mechanics of mussel adhesion. *Proc. Natl. Acad. Sci. U. S. A.* **2006,** *103*, 12999-13003.

72. Li, Y.; Liu, H.; Wang, T.; Qin, M.; Cao, Y.; Wang, W. Single‐molecule force spectroscopy reveals multiple binding modes between DOPA and different rutile surfaces. *ChemPhysChem* **2016**.

73. Lin, Q.; Gourdon, D.; Sun, C.; Holten-Andersen, N.; Anderson, T. H.; Waite, J. H.; Israelachvili, J. N. Adhesion mechanisms of the mussel foot proteins mfp-1 and mfp-3. *Proc. Natl. Acad. Sci. U. S. A.* **2007,** *104*, 3782-3786.

74. Zeng, H.; Hwang, D. S.; Israelachvili, J. N.; Waite, J. H. Strong reversible Fe3+-mediated bridging between dopa-containing protein films in water. *Proc. Natl. Acad. Sci. U. S. A.* **2010,** *107*, 12850-12853.

75. Lu, Q.; Danner, E.; Waite, J. H.; Israelachvili, J. N.; Zeng, H.; Hwang, D. S. Adhesion of mussel foot proteins to different substrate surfaces. *J. R. Soc., Interface* **2013,** *10*, 20120759.

76. Hwang, D. S.; Zeng, H.; Masic, A.; Harrington, M. J.; Israelachvili, J. N.; Waite, J. H. Protein-and metal-dependent interactions of a prominent protein in mussel adhesive plaques. *J. Biol. Chem.* **2010,** *285*, 25850-25858.

77. Maier, G. P.; Rapp, M. V.; Waite, J. H.; Israelachvili, J. N.; Butler, A. Adaptive synergy between catechol and lysine promotes wet adhesion by surface salt displacement. *Science* **2015,** *349*, 628-632.

78. Ye, Q.; Zhou, F.; Liu, W. Bioinspired catecholic chemistry for surface modification. *Chem. Soc. Rev.* **2011,** *40*, 4244-4258.

79. Li, S.-C.; Wang, J.-g.; Jacobson, P.; Gong, X.-Q.; Selloni, A.; Diebold, U. Correlation between bonding geometry and band gap states at organic− inorganic interfaces: catechol on rutile TiO2 (110). *J. Am. Chem. Soc.* **2009,** *131*, 980-984.

80. Anderson, T. H.; Yu, J.; Estrada, A.; Hammer, M. U.; Waite, J. H.; Israelachvili, J. N. The contribution of DOPA to substrate–peptide adhesion and internal cohesion of mussel‐inspired synthetic peptide films. *Adv. Funct. Mater.* **2010,** *20*, 4196-4205.

81. Harrington, M. J.; Masic, A.; Holten-Andersen, N.; Waite, J. H.; Fratzl, P.

Iron-clad fibers: a metal-based biological strategy for hard flexible coatings. *Science* **2010,** *328*, 216-220.

82. Sommer, L. Titan (IV)-chelate mit brenzcatechin, brenzcatechin-3, 5-disulfonsäure und protocatechusäure. *Collect. Czech. Chem. Commun.* **1963,** *28*, 2102-2130.

83. Burley, S.; Petsko, G. Aromatic-aromatic interaction: a mechanism of protein structure stabilization. *Science* **1985,** *229*, 23-28.

84. Chen, F.; Xing, Y.; Wang, Z.; Zheng, X.; Zhang, J.; Cai, K. Nanoscale polydopamine (PDA) meets π–π interactions: an interface-directed coassembly approach for mesoporous nanoparticles. *Langmuir* **2016,** *32*, 12119-12128.

85. Dougherty, D. A. Cation-pi interactions in chemistry and biology: a new view of benzene, Phe, Tyr, and Trp. *Science* **1996,** *271*, 163.

86. Lu, Q.; Oh, D. X.; Lee, Y.; Jho, Y.; Hwang, D. S.; Zeng, H. Nanomechanics of cation–π interactions in aqueous solution. *Angew. Chem., Int. Ed.* **2013,** *52*, 3944-3948.

87. Lu, Q.; Hwang, D. S.; Liu, Y.; Zeng, H. Molecular interactions of mussel protective coating protein, mcfp-1, from Mytilus californianus. *Biomaterials* **2012,** *33*, 1903-1911.

88. Kim, S.; Huang, J.; Lee, Y.; Dutta, S.; Yoo, H. Y.; Jung, Y. M.; Jho, Y.; Zeng, H.; Hwang, D. S. Complexation and coacervation of like-charged polyelectrolytes inspired by mussels. *Proc. Natl. Acad. Sci. U. S. A.* **2016,** *113*, E847-E853.

89. Regeimbal, J.; Gleiter, S.; Trumpower, B. L.; Yu, C.-A.; Diwakar, M.; Ballou, D. P.; Bardwell, J. C. Disulfide bond formation involves a quinhydrone-type charge–transfer complex. *Proc. Natl. Acad. Sci. U. S. A.* **2003,** *100*, 13779-13784.

90. Dreyer, D. R.; Miller, D. J.; Freeman, B. D.; Paul, D. R.; Bielawski, C. W. Elucidating the structure of poly (dopamine). *Langmuir* **2012,** *28*, 6428-6435.

91. Liu, Y.; Ai, K.; Lu, L. Polydopamine and its derivative materials: synthesis and promising applications in energy, environmental, and biomedical fields. *Chem. Rev.* **2014,** *114*, 5057-5115.

92. Kord Forooshani, P.; Lee, B. P. Recent approaches in designing bioadhesive materials inspired by mussel adhesive protein. *J. Polym. Sci., Part A: Polym. Chem.* **2016**.

93. Israelachvili, J.; Min, Y.; Akbulut, M.; Alig, A.; Carver, G.; Greene, W.; Kristiansen, K.; Meyer, E.; Pesika, N.; Rosenberg, K. Recent advances in the surface forces apparatus (SFA) technique. *Rep. Prog. Phys.* **2010,** *73*, 036601.

94. Tabor, D.; Winterton, R. In *The direct measurement of normal and retarded van der Waals forces*, Proceedings of the Royal Society of London A: Mathematical, Physical and Engineering Sciences, The Royal Society: 1969; pp 435-450.

95. Israelachvili, J.; Adams, G. Direct measurement of long range forces between two mica surfaces in aqueous KNO3 solutions. *Nature* **1976,** *262*, 774-776.

96. Israelachvili, J. N.; Adams, G. E. Measurement of forces between two mica surfaces in aqueous electrolyte solutions in the range 0–100 nm. *J. Chem. Soc., Faraday Trans. 1* **1978,** *74*, 975-1001.

97. Tadmor, R.; Hernández-Zapata, E.; Chen, N.; Pincus, P.; Israelachvili, J. N. Debye length and double-layer forces in polyelectrolyte solutions. *Macromolecules* **2002,** *35*, 2380-2388.

98. Israelachvili, J. N.; Wennerstroem, H. Hydration or steric forces between amphiphilic surfaces? *Langmuir* **1990,** *6*, 873-876.

99. Israelachvili, J. Differences between non-specific and bio-specific, and between equilibrium and non-equilibrium, interactions in biological systems. *Q. Rev. Biophys.* **2005,** *38*, 331-337.

100. Israelachvili, J. N. Adhesion, friction and lubrication of molecularly smooth surfaces. In *Fundamentals of friction: macroscopic and microscopic processes*, Springer: 1992; pp 351-385.

101. Zeng, H. *Interactions of polymer surfaces and thin films*. ProQuest: 2007.

102. Israelachvili, J. N. Thin film studies using multiple-beam interferometry. *J. Colloid Interface Sci.* **1973,** *44*, 259-272.

103. Tolansky, S. *An introduction to interferometry*. John Wiley & Sons: 1973.

104. Clarkson, M. Multiple-beam interferometry with thin metal films and unsymmetrical systems. *J. Phys. D: Appl. Phys.* **1989,** *22*, 475.

105. Horn, R. G.; Smith, D. T. Analytic solution for the three-layer multiple beam interferometer. *Appl. Opt.* **1991,** *30*, 59-65.

106. Johnson, K.; Kendall, K.; Roberts, A. In *Surface energy and the contact of elastic solids*, Proceedings of the Royal Society of London A: Mathematical, Physical and Engineering Sciences, The Royal Society: 1971; pp 301-313.

107. Derjaguin, B. V.; Muller, V. M.; Toporov, Y. P. Effect of contact deformations on the adhesion of particles. *J. Colloid Interface Sci.* **1975,** *53*, 314-326.

108. Maugis, D. Adhesion of spheres: the JKR-DMT transition using a Dugdale model. *J. Colloid Interface Sci.* **1992,** *150*, 243-269.

109. Zeng, H.; Zhao, B.; Tian, Y.; Tirrell, M.; Leal, L. G.; Israelachvili, J. N. Transient surface patterns during adhesion and coalescence of thin liquid films. *Soft Matter* **2007,** *3*, 88-93.

110. Zeng, H.; Tian, Y.; Zhao, B.; Tirrell, M.; Israelachvili, J. Transient surface patterns and instabilities at adhesive junctions of viscoelastic films. *Macromolecules* **2007,** *40*, 8409-8422.

111. Binnig, G.; Quate, C. F.; Gerber, C. Atomic force microscope. *Phys. Rev. Lett.* **1986,** *56*, 930.

112. Morita, S.; Wiesendanger, R.; Meyer, E. Noncontact atomic force microscopy. **2009**.

113. Gross, L.; Mohn, F.; Moll, N.; Liljeroth, P.; Meyer, G. The chemical structure of a molecule resolved by atomic force microscopy. *Science* **2009,** *325*, 1110-1114.

114. Zhong, Q.; Inniss, D.; Kjoller, K.; Elings, V. Fractured polymer/silica fiber surface studied by tapping mode atomic force microscopy. *Surf. Sci. Lett.* **1993,** *290*, L688-L692.

115. Geisse, N. A. AFM and combined optical techniques. *Mater. Today* **2009,** *12*, 40-45.

116. Rabinovich, Y. I.; Yoon, R.-H. Use of atomic force microscope for the

measurements of hydrophobic forces between silanated silica plate and glass sphere. *Langmuir* **1994,** *10*, 1903-1909.

117.Ducker, W. A.; Senden, T. J.; Pashley, R. M. Direct measurement of colloidal forces using an atomic force microscope. **1991**.

118.Butt, H.-J.; Cappella, B.; Kappl, M. Force measurements with the atomic force microscope: Technique, interpretation and applications. *Surf. Sci. Rep.* **2005,** *59*, 1-152.

119.Rief, M.; Oesterhelt, F.; Heymann, B.; Gaub, H. E. Single molecule force spectroscopy on polysaccharides by atomic force microscopy. *Science* **1997,** *275*, 1295-1297.

120. Rief, M.; Gautel, M.; Oesterhelt, F.; Fernandez, J. M.; Gaub, H. E. Reversible unfolding of individual titin immunoglobulin domains by AFM. *Science* **1997,** *276*, 1109-1112.

121. Brune, D.; Hellborg, R.; Whitlow, H. J.; Hunderi, O. *Surface characterization: a user's sourcebook*. John Wiley & Sons: 2008.

122. Hüfner, S. *Photoelectron spectroscopy: principles and applications*. Springer Science & Business Media: 2013.

123. Azzam, R. M.; Bashara, N. M. *Ellipsometry and Polarized Light*. North-Holland. sole distributors for the USA and Canada, Elsevier Science Publishing Co., Inc.: 1987.

124. Yuan, Y.; Lee, T. R. Contact angle and wetting properties. In *Surface Science Techniques*, Springer: 2013; pp 3-34.

125. Hall, D. B.; Underhill, P.; Torkelson, J. M. Spin coating of thin and ultrathin polymer films. *Polym. Eng. Sci.* **1998,** *38*, 2039-2045.

126. Goldstein, J.; Newbury, D. E.; Echlin, P.; Joy, D. C.; Romig Jr, A. D.; Lyman, C. E.; Fiori, C.; Lifshin, E. *Scanning electron microscopy and X-ray microanalysis: a text for biologists, materials scientists, and geologists*. Springer Science & Business Media: 2012.

127. Wilson, R. G.; Stevie, F. A.; Magee, C. W. *Secondary ion mass spectrometry:*

a practical handbook for depth profiling and bulk impurity analysis. Wiley-Interscience: 1989.

128. Arkles, B.Hydrophobicity, hydrophilicity and silane surface modification. Gelest: Morrisville, 2009; pp 1-80.

129. Gao, L.; McCarthy, T. J. A perfectly hydrophobic surface (θA/θR= 180/180). *J. Am. Chem. Soc.* **2006,** *128*, 9052-9053.

130. Roach, P.; Shirtcliffe, N. J.; Newton, M. I. Progess in superhydrophobic surface development. *Soft Matter* **2008,** *4*, 224-240.

131. Yi, D.; Xu, C.; Tang, R.; Zhang, X.; Caruso, F.; Wang, Y. Synthesis of discrete alkyl ‐ silica hybrid nanowires and their assembly into nanostructured superhydrophobic membranes. *Angew. Chem., Int. Ed.* **2016,** *128*, 8515-8520.

132. Lung, C. Y. K.; Matinlinna, J. P. Aspects of silane coupling agents and surface conditioning in dentistry: An overview. *Dent. Mater.* **2012,** *28*, 467-477.

133. Ohno, K.; Morinaga, T.; Koh, K.; Tsujii, Y.; Fukuda, T. Synthesis of monodisperse silica particles coated with well-defined, high-density polymer brushes by surface-initiated atom transfer radical polymerization. *Macromolecules* **2005,** *38*, 2137-2142.

134. Ulman, A. Formation and structure of self-assembled monolayers. *Chem. Rev.* **1996,** *96*, 1533-1554.

135. Ito, Y.; Virkar, A. A.; Mannsfeld, S.; Oh, J. H.; Toney, M.; Locklin, J.; Bao, Z. A. Crystalline ultrasmooth self-assembled monolayers of alkylsilanes for organic field-effect transistors. *J. Am. Chem. Soc.* **2009,** *131*, 9396-9404.

136. Halik, M.; Klauk, H.; Zschieschang, U.; Schmid, G.; Dehm, C.; Schutz, M.; Maisch, S.; Effenberger, F.; Brunnbauer, M.; Stellacci, F. Low-voltage organic transistors with an amorphous molecular gate dielectric. *Nature* **2004,** *431*, 963-966.

137. Kessel, C. R.; Granick, S. Formation and characterization of a highly ordered and well-anchored alkylsilane monolayer on mica by self-assembly. *Langmuir* **1991,** *7*, 532-538.

138. Wang, Y. L.; Lieberman, M. Growth of ultrasmooth octadecyltrichlorosilane

self-assembled monolayers on SiO2. *Langmuir* **2003,** *19*, 1159-1167.

139. Fadeev, A. Y.; McCarthy, T. J. Trialkylsilane monolayers covalently attached to silicon surfaces: Wettability studies indicating that molecular topography contributes to contact angle hysteresis. *Langmuir* **1999,** *15*, 3759-3766.

140. Saner, C. K.; Lusker, K. L.; LeJeune, Z. M.; Serem, W. K.; Garno, J. C. Self-assembly of octadecyltrichlorosilane: Surface structures formed using different protocols of particle lithography. *Beilstein J. Nanotech.* **2012,** *3*, 114-122.

141. Liberelle, B.; Banquy, X.; Giasson, S. Stability of silanols and grafted alkylsilane monolayers on plasma-activated mica surfaces. *Langmuir* **2008,** *24*, 3280-3288.

142. Kan, Y.; Tan, Q.; Wu, G.; Si, W.; Chen, Y. Study of DNA adsorption on mica surfaces using a surface force apparatus. *Sci. Rep.* **2015,** *5*.

143. Zeng, H.; Maeda, N.; Chen, N.; Tirrell, M.; Israelachvili, J. Adhesion and friction of polystyrene surfaces around T g. *Macromolecules* **2006,** *39*, 2350-2363.

144. Pick, C.; Argento, C.; Drazer, G.; Frechette, J. Micropatterned charge heterogeneities via vapor deposition of aminosilanes. *Langmuir* **2015,** *31*, 10725-10733.

145. Yoon, R. H.; Flinn, D. H.; Rabinovich, Y. I. Hydrophobic interactions between dissimilar surfaces. *J. Colloid Interface Sci.* **1997,** *185*, 363-370.

146. Butt, H.-J.; Jaschke, M. Calculation of thermal noise in atomic force microscopy. *Nanotechnology* **1995,** *6*, 1.

147. Zeng, H. B. *Polymer adhesion, friction, and lubrication*. 2013.

148. Biggs, S.; Grieser, F. Atomic force microscopy imaging of thin films formed by hydrophobing reagents. *J. Colloid Interface Sci.* **1994,** *165*, 425-430.

149. Zhang, L.; Zeng, H. B.; Liu, Q. X. Probing molecular and surface interactions of comb-type polymer polystyrene-graft-poly(ethylene oxide) (PS-g-PEO) wuth an SFA. *J. Phys. Chem. C* **2012,** *116*, 17554-17562.

150. Zeng, H.; Pesika, N.; Tian, Y.; Zhao, B.; Chen, Y.; Tirrell, M.; Turner, K. L.; Israelachvili, J. N. Frictional adhesion of patterned surfaces and implications for

gecko and biomimetic systems. *Langmuir* **2009,** *25*, 7486-7495.

151. Johnson, K.; Kendall, K.; Roberts, A. Surface energy and the contact of elastic solids. *Proc. Math. Phys. Eng. Sci.,* **1971,** *324*, 301-313.

152. Johnson, K. L. *Contact mechanics*. Cambridge University Press: 1985.

153. Christenson, H. K. Adhesion and surface-energy of mica in air and water. *Journal of Physical Chemistry* **1993,** *97*, 12034-12041.

154. Teng, F. C.; Zeng, H. B.; Liu, Q. X. Understanding the Deposition and Surface Interactions of Gypsum. *J. Phys. Chem. C* **2011,** *115*, 17485-17494.

155. Qian, L.; Yu, B. Adhesion hysteresis. In *Encyclopedia of Tribology*, Wang, Q. J.; Chung, Y.-W., Eds. Springer US: Boston, MA, 2013; pp 29-32.

156. Maeda, N.; Chen, N.; Tirrell, M.; Israelachvili, J. N. Adhesion and friction mechanisms of polymer-on-polymer surfaces. *Science* **2002,** *297*, 379-382.

157. Horn, R. G.; Israelachvili, J. N.; Pribac, F. Measurement of the deformation and adhesion of solids in contact. *J. Colloid Interface Sci.* **1987,** *115*, 480-492.

158. Chen, Y. L.; Helm, C. A.; Israelachvili, J. N. Molecular mechanisms associated with adhesion and contact-angle hysteresis of monolayer surfaces. *Journal of Physical Chemistry* **1991,** *95*, 10736-10747.

159. Pashley, R. DLVO and hydration forces between mica surfaces in Li+, Na+, K+, and Cs+ electrolyte solutions: a correlation of double-layer and hydration forces with surface cation exchange properties. *J. Colloid Interface Sci.* **1981,** *83*, 531-546.

160. Wright, D. S.; Flavel, B. S.; Quinton, J. S. In *Streaming zeta potential measurements of surface-bound organosilane molecular species*, 2006 International Conference on Nanoscience and Nanotechnology, IEEE: 2006.

161. Ambrozewicz, D.; Ciesielczyk, F.; Nowacka, M.; Karasiewicz, J.; Piasecki, A.; Maciejewski, H.; Jesionowski, T. Fluoroalkylsilane versus alkylsilane as hydrophobic agents for silica and silicates. *J. Nanomater.* **2013,** *2013*, 18.

162. Bowden, F. P.; Tabor, D. *The friction and lubrication of solids-{part I}*. 1950.

163. Fuller, K.; Tabor, D. In *The effect of surface roughness on the adhesion of elastic solids*, Proc. Math. Phys. Eng. Sci.,, The Royal Society: 1975; pp 327-342.

164. Laskowski, J.; Kitchener, J. The hydrophilic—hydrophobic transition on silica. *J. Colloid Interface Sci.* **1969,** *29*, 670-679.

165. Lützenkirchen, J.; Richter, C. Zeta-potential measurements of OTS-covered silica samples. *Adsorption* **2013,** *19*, 217-224.

166. Wu, L.; Baghdachi, J. *Functional Polymer Coatings: Principles, Methods, and Applications*. John Wiley & Sons: 2015; Vol. 12.

167. Zdyrko, B.; Luzinov, I. Polymer brushes by the "grafting to" method. *Macromol. Rapid Commun.* **2011,** *32*, 859-869.

168. Kato, K.; Uchida, E.; Kang, E.-T.; Uyama, Y.; Ikada, Y. Polymer surface with graft chains. *Prog. Polym. Sci.* **2003,** *28*, 209-259.

169. Barbey, R.; Lavanant, L.; Paripovic, D.; Schüwer, N.; Sugnaux, C.; Tugulu, S.; Klok, H.-A. Polymer brushes via surface-initiated controlled radical polymerization: synthesis, characterization, properties, and applications. *Chem. Rev.* **2009,** *109*, 5437-5527.

170. Arnold, R. M.; McNitt, C. D.; Popik, V. V.; Locklin, J. Direct grafting of poly(pentafluorophenyl acrylate) onto oxides: versatile substrates for reactive microcapillary printing and self-sorting modification. *Chem. Commun.* **2014,** *50*, 5307-5309.

171. Eberhardt, M.; Mruk, R.; Zentel, R.; Théato, P. Synthesis of pentafluorophenyl (meth) acrylate polymers: New precursor polymers for the synthesis of multifunctional materials. *Eur. Polym. J.* **2005,** *41*, 1569-1575.

172. Chandler, D. Interfaces and the driving force of hydrophobic assembly. *Nature* **2005,** *437*, 640-647.

173. Attard, P. Nanobubbles and the hydrophobic attraction. *Adv. Colloid Interface Sci.* **2003,** *104*, 75-91.

174. Faghihnejad, A.; Zeng, H. B. Interaction mechanism between hydrophobic and hydrophilic surfaces: using polystyrene and mica as a model system. *Langmuir* **2013,** *29*, 12443-12451.

175. Cui, X.; Shi, C.; Xie, L.; Liu, J.; Zeng, H. Probing interactions between air

bubble and hydrophobic polymer surface: impact of solution salinity and interfacial nanobubbles. *Langmuir* **2016,** *32*, 11236-11244.

176. Doncom, K. E.; Hansell, C. F.; Theato, P.; O'Reilly, R. K. pH-switchable polymer nanostructures for controlled release. *Polym. Chem.* **2012,** *3*, 3007-3015.

177. Liu, Z.; Li, Z.; Zhou, H.; Wei, G.; Song, Y.; Wang, L. Immobilization and condensation of DNA with 3‐aminopropyltriethoxysilane studied by atomic force microscopy. *J. Microsc.* **2005,** *218*, 233-239.

178. Lu, Q.; Wang, J.; Faghihnejad, A.; Zeng, H.; Liu, Y. Understanding the molecular interactions of lipopolysaccharides during E. coli initial adhesion with a surface forces apparatus. *Soft Matter* **2011,** *7*, 9366-9379.

179. Ellison, A.; Zisman, W. Wettability studies on nylon, polyethylene terephthalate and polystyrene. *J. Phys. Chem.* **1954,** *58*, 503-506.

180. Chen, N.; Maeda, N.; Tirrell, M.; Israelachvili, J. Adhesion and friction of polymer surfaces: the effect of chain ends. *Macromolecules* **2005,** *38*, 3491-3503.

181. Zhang, X. H.; Quinn, A.; Ducker, W. A. Nanobubbles at the interface between water and a hydrophobic solid. *Langmuir* **2008,** *24*, 4756-4764.

182. Ishida, N.; Inoue, T.; Miyahara, M.; Higashitani, K. Nano bubbles on a hydrophobic surface in water observed by tapping-mode atomic force microscopy. *Langmuir* **2000,** *16*, 6377-6380.

183. Zhang, X. H.; Khan, A.; Ducker, W. A. A nanoscale gas state. *Phys. Rev. Lett.* **2007,** *98*, 136101.

184. Tyrrell, J. W.; Attard, P. Images of nanobubbles on hydrophobic surfaces and their interactions. *Phys. Rev. Lett.* **2001,** *87*, 176104.

185. Ariga, K.; Hill, J. P.; Ji, Q. Layer-by-layer assembly as a versatile bottom-up nanofabrication technique for exploratory research and realistic application. *Phys. Chem. Chem. Phys.* **2007,** *9*, 2319-2340.

186. Lvov, Y.; Yamada, S.; Kunitake, T. Non-linear optical effects in layer-by-layer alternate films of polycations and an azobenzene-containing polyanion. *Thin Solid Films* **1997,** *300*, 107-112.

187. Bhushan, B.; Israelachvili, J. N.; Landman, U. Nanotribology: friction, wear and lubrication at the atomic scale. *Nature* **1995,** *374*, 607-616.

188. Lvov, Y.; Ariga, K.; Ichinose, I.; Kunitake, T. Assembly of multicomponent protein films by means of electrostatic layer-by-layer adsorption. *J. Am. Chem. Soc.* **1995,** *117*, 6117-6123.

189. Baker, R. W. *Membrane Technology*. Wiley Online Library: 2000.

190. Decher, G.; Hong, J.; Schmitt, J. Buildup of ultrathin multilayer films by a self-assembly process: III. Consecutively alternating adsorption of anionic and cationic polyelectrolytes on charged surfaces. *Thin Solid Films* **1992,** *210*, 831-835.

191. Cho, J.; Char, K.; Hong, J. D.; Lee, K. B. Fabrication of highly ordered multilayer films using a spin self‐assembly method. *Adv. Mater.* **2001,** *13*, 1076-1078.

192. Middleman, S. The effect of induced air‐flow on the spin coating of viscous liquids. *J. Appl. Phys.* **1987,** *62*, 2530-2532.

193. Rehg, T. J.; Higgins, B. G. The effects of inertia and interfacial shear on film flow on a rotating disk. *Phys. Fluids* **1988,** *31*, 1360.

194. Ma, F.; Hwang, J. The effect of air shear on the flow of a thin liquid film over a rough rotating disk. *J. Appl. Phys.* **1990,** *68*, 1265-1271.

195. Stockton, W.; Rubner, M. Molecular-level processing of conjugated polymers. 4. Layer-by-layer manipulation of polyaniline via hydrogen-bonding interactions. *Macromolecules* **1997,** *30*, 2717-2725.

196. Rydzek, G.; Schaaf, P.; Voegel, J.-C.; Jierry, L.; Boulmedais, F. Strategies for covalently reticulated polymer multilayers. *Soft Matter* **2012,** *8*, 9738-9755.

197. Such, G. K.; Quinn, J. F.; Quinn, A.; Tjipto, E.; Caruso, F. Assembly of ultrathin polymer multilayer films by click chemistry. *J. Am. Chem. Soc.* **2006,** *128*, 9318-9319.

198. Shimazaki, Y.; Mitsuishi, M.; Ito, S.; Yamamoto, M. Preparation of the layer-by-layer deposited ultrathin film based on the charge-transfer interaction. *Langmuir* **1997,** *13*, 1385-1387.

199. Seo, J.; Schattling, P.; Lang, T.; Jochum, F.; Nilles, K.; Theato, P.; Char, K. Covalently bonded layer-by-layer assembly of multifunctional thin films based on activated esters. *Langmuir* **2009,** *26*, 1830-1836.

200. Batz, H. G.; Franzmann, G.; Ringsdorf, H. Model reactions for synthesis of pharmacologically active polymers by way of monomeric and polymeric reactive esters. *Angew. Chem., Int. Ed.* **1972,** *11*, 1103-1104.

201. Ferruti, P.; Bettelli, A.; Feré, A. High polymers of acrylic and methacrylic esters of N-hydroxysuccinimide as polyacrylamide and polymethacrylamide precursors. *Polymer* **1972,** *13*, 462-464.

202. Arnold, R. M.; McNitt, C. D.; Popik, V. V.; Locklin, J. Direct grafting of poly (pentafluorophenyl acrylate) onto oxides: versatile substrates for reactive microcapillary printing and self-sorting modification. *Chem. Commun.* **2014,** *50*, 5307-5309.

203. Han, S.-Y.; Kim, Y.-A. Recent development of peptide coupling reagents in organic synthesis. *Tetrahedron* **2004,** *60*, 2447-2467.

204. Zeng, X. Y.; Zhang, Q. K.; Yu, R. M.; Lu, C. Z. A new transparent conductor: silver nanowire film buried at the surface of a transparent polymer. *Adv. Mater.* **2010,** *22*, 4484-4488.

205. Claesson, P.; Paulson, O.; Blomberg, E.; Burns, N. Surface properties of poly (ethylene imine)-coated mica surfaces—salt and pH effects. *Colloids Surf., A* **1997,** *123*, 341-353.

206. Flammang, P.; Aldred, N.; Santos, R.; Gorb, S. *Biological and Biomimetic Adhesives: Challenges and Opportunities*. Royal Society of Chemistry: 2013.

207. Silverman, H. G.; Roberto, F. F. Understanding marine mussel adhesion. *Mar. Biotechnol.* **2007,** *9*, 661-681.

208. Ku, S. H.; Park, C. B. Human endothelial cell growth on mussel-inspired nanofiber scaffold for vascular tissue engineering. *Biomaterials* **2010,** *31*, 9431-9437.

209. Ku, S. H.; Ryu, J.; Hong, S. K.; Lee, H.; Park, C. B. General functionalization route for cell adhesion on non-wetting surfaces. *Biomaterials* **2010,**

31, 2535-2541.

210. Cui, J.; Yan, Y.; Such, G. K.; Liang, K.; Ochs, C. J.; Postma, A.; Caruso, F. Immobilization and intracellular delivery of an anticancer drug using mussel-inspired polydopamine capsules. *Biomacromolecules* **2012,** *13*, 2225-2228.

211. Qiang, W.; Li, W.; Li, X.; Chen, X.; Xu, D. Bioinspired polydopamine nanospheres: a superquencher for fluorescence sensing of biomolecules. *Chem. Sci.* **2014,** *5*, 3018-3024.

212. You, I.; Kang, S. M.; Lee, S.; Cho, Y. O.; Kim, J. B.; Lee, S. B.; Nam, Y. S.; Lee, H. Polydopamine microfluidicsSystem toward a two‐dimensional, gravity‐driven mixing device. *Angew. Chem., Int. Ed.* **2012,** *51*, 6126-6130.

213. Liu, C. B.; Meng, W.; Li, F.; Wang, S.; Nie, J.; Ma, J. A. A facile parallel synthesis of trifluoroethyl‐substituted alkynes. *Angew. Chem., Int. Ed.* **2012,** *51*, 6227-6230.

214. Ryou, M. H.; Kim, J.; Lee, I.; Kim, S.; Jeong, Y. K.; Hong, S.; Ryu, J. H.; Kim, T. S.; Park, J. K.; Lee, H. Mussel‐inspired adhesive binders for high‐performance silicon nanoparticle anodes in Lithium‐Ion batteries. *Adv. Mater.* **2013,** *25*, 1571-1576.

215. Tanaka, M.; Yoshida, M.; Emoto, H.; Ishii, H. Noradrenaline systems in the hypothalamus, amygdala and locus coeruleus are involved in the provocation of anxiety: basic studies. *Eur. J. Pharmacol.* **2000,** *405*, 397-406.

216. Yu, J.; Wei, W.; Danner, E.; Ashley, R. K.; Israelachvili, J. N.; Waite, J. H. Mussel protein adhesion depends on interprotein thiol-mediated redox modulation. *Nat. Chem. Biol.* **2011,** *7*, 588-590.

217. Yu, J.; Wei, W.; Danner, E.; Israelachvili, J. N.; Waite, J. H. Effects of interfacial redox in mussel adhesive protein films on mica. *Adv. Mater.* **2011,** *23*, 2362-2366.

218. Hong, S.; Na, Y. S.; Choi, S.; Song, I. T.; Kim, W. Y.; Lee, H. Non‐covalent self‐assembly and covalent polymerization co‐contribute to polydopamine formation. *Adv. Funct. Mater.* **2012,** *22*, 4711-4717.

219. d'Ischia, M.; Napolitano, A.; Pezzella, A.; Meredith, P.; Sarna, T. Chemical and structural diversity in eumelanins: unexplored bio‐optoelectronic materials. *Angew. Chem., Int. Ed.* **2009,** *48*, 3914-3921.

220. Meredith, P.; Powell, B. J.; Riesz, J.; Nighswander-Rempel, S. P.; Pederson, M. R.; Moore, E. G. Towards structure–property–function relationships for eumelanin. *Soft Matter* **2006,** *2*, 37-44.

221. Wang, W.; Li, R.; Tian, M.; Liu, L.; Zou, H.; Zhao, X.; Zhang, L. Surface silverized meta-aramid fibers prepared by bio-inspired poly (dopamine) functionalization. *ACS Appl. Mater. Interfaces* **2013,** *5*, 2062-2069.

222. d'Ischia, M.; Napolitano, A.; Ball, V.; Chen, C.-T.; Buehler, M. J. Polydopamine and eumelanin: from structure–property relationships to a unified tailoring strategy. *Acc. Chem. Res.* **2014,** *47*, 3541-3550.

223. Ball, V.; Del Frari, D.; Toniazzo, V.; Ruch, D. Kinetics of polydopamine film deposition as a function of pH and dopamine concentration: Insights in the polydopamine deposition mechanism. *J. Colloid Interface Sci.* **2012,** *386*, 366-372.

224. Ma, J. C.; Dougherty, D. A. The cation-π interaction. *Chem. Rev.* **1997,** *97*, 1303-1324.

225. Herrmann, A. Dynamic combinatorial/covalent chemistry: A tool to read, generate and modulate the bioactivity of compounds and compound mixtures. *Chem. Soc. Rev.* **2014,** *43*, 1899-1933.

226. Ju, K.-Y.; Lee, Y.; Lee, S.; Park, S. B.; Lee, J.-K. Bioinspired polymerization of dopamine to generate melanin-like nanoparticles having an excellent free-radical-scavenging property. *Biomacromolecules* **2011,** *12*, 625-632.

227. Sanchez-Cortes, S.; Francioso, O.; Garcıa-Ramos, J.; Ciavatta, C.; Gessa, C. Catechol polymerization in the presence of silver surface. *Colloids Surf., A* **2001,** *176*, 177-184.

228. Pashley, R. Hydration forces between mica surfaces in aqueous electrolyte solutions. *J. Colloid Interface Sci.* **1981,** *80*, 153-162.

229. Gallivan, J. P.; Dougherty, D. A. A computational study of cation−π

interactions vs salt bridges in aqueous media: implications for protein engineering. *J. Am. Chem. Soc.* **2000,** *122*, 870-874.

230. Kim, S.; Faghihnejad, A.; Lee, Y.; Jho, Y.; Zeng, H.; Hwang, D. S. Cation–π interaction in DOPA-deficient mussel adhesive protein mfp-1. *J. Mater. Chem. B* **2015,** *3*, 738-743.